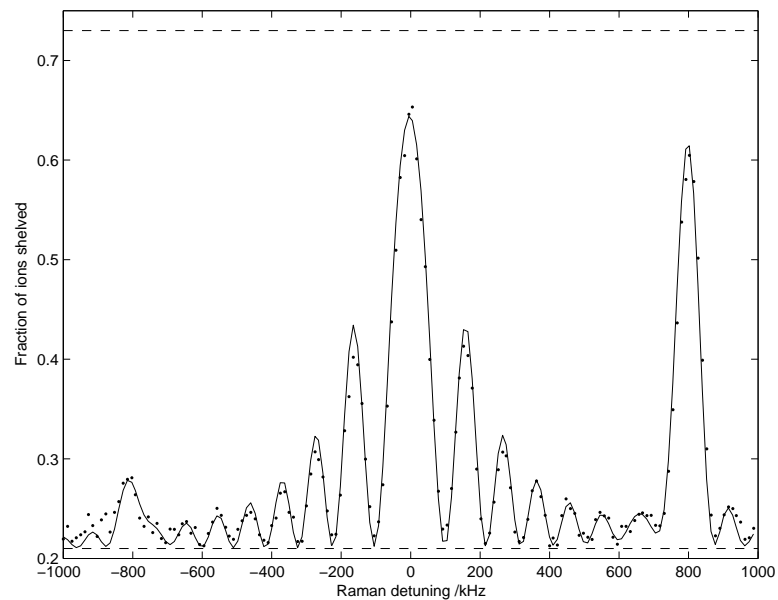

Raman Sideband Cooling and Coherent Manipulation of Trapped Ions

A thesis submitted for the degree of
Doctor of Philosophy



Simon Webster

Hilary Term
2005

St. John's College
Oxford

Abstract

This thesis describes experiments primarily concerned with the manipulation of the spin and quantum motional state of single trapped ions and pairs of ions.

A two stage photoionization system is described. This allows the loading of ions of a specific isotope of calcium into our trap. We measure the absolute cross section for photoionization from the $4s4p\ ^1P_1$ state of neutral Ca. We demonstrate the loading and cooling of all the naturally occurring isotopes of calcium, including of pure crystals of $^{43}\text{Ca}^+$.

A magnetic resonance is used to determine accurately the Zeeman splitting of the ground state of a $^{40}\text{Ca}^+$ ion. The coherent manipulation of the spin state of a $^{40}\text{Ca}^+$ ion using this magnetic resonance is shown. We observe high quality Rabi oscillations between the two spin states with π times of order $100\ \mu\text{s}$ and with decay times of order milliseconds. By using multiple pulses of this magnetic resonance in a Ramsey type experiment we are able to measure the net light shift induced on the two spin states by a circularly polarised far-off-resonant beam, and thus deduce its intensity precisely, and also ensure that such a beam is linearly polarised to high accuracy.

We demonstrate a laser-driven rotation of the qubit with a π time of order a few microseconds. We also implement Rabi flopping by Raman carrier transitions, with a similar π time.

We investigate three Raman sideband cooling methods applied to a single $^{40}\text{Ca}^+$ ion. Two of these provide continuous cooling, with the lasers which drive the Raman transitions also providing the repumping. A simple theoretical model for this continuous cooling process is presented. The third method is pulsed sideband cooling, using pulses of far-off-resonant Raman beams to drive the first red motional sideband of the ion, and then use a near-resonant beam to act as a repumper. The mean vibrational excitation of the ion is measured by comparing sideband heights, for these three cooling schemes. We achieve maximum ground state occupation probabilities of over 85%.

We also demonstrate sub-Doppler cooling of a pair of trapped ions. Using a continuous cooling method followed by pulsed sideband cooling of the two axial motional modes we demonstrate cooling of both modes into the Lamb-Dicke regime.

We present a rate equations program developed to study $^{43}\text{Ca}^+$, which we intend to use to embody our qubit in future experiments. We use our program to fit data taken from a trapped $^{43}\text{Ca}^+$ ion during photoionization experiments and to study the effect of the hyperfine structure of the ion on producing a high scattering rate during Doppler cooling of the ion.

Acknowledgements

My first thanks go to my supervisor Prof. Andrew Steane for all his help and guidance which has made this work possible, and whose enthusiasm to try new things in the lab is unmatched. My thanks also go to Prof. Derek Stacey whose enthusiasm to get things working correctly in the lab is unmatched. Dr. David Lucas has been a great help in getting the work presented here done. His knowledge and mastery of the experiment is awe inspiring at times and my thanks go to him.

I must thank all the other ion trappers for their friendship, hard work on the experiment and time spent drinking tea in the Clarendon common room: Dr. Matthew McDonnell, Dr. J.-P. Stacey, Dr. Angel Ramas, Dr. Marek Šašura, Jonathan Home, Ben Keitch, Nick Thomas and Greg Imreh. Out of all these I would particularly like to thank Matt and J.-P. for their friendship when I first joined the group. Thanks also to Graham Quelch, George Matthews and Rob Harris for their practical help and advice in the workshop.

Outside of the lab thanks to all the friends I've made in Oxford, both as an undergraduate and a graduate, and who have made my time here so enjoyable.

My parents have made all of this possible. While they may not understand why I want to be a physicist, their love and support have helped me to become one.

Finally I thank Katrina, for her love and for being there for me over the past five years.

Contents

Abstract	i
Acknowledgements	ii
1 Introduction	1
1.1 Quantum computing in an ion trap	1
1.1.1 Quantum gates	3
1.2 Summary of the thesis	7
2 Apparatus	9
2.1 Building blocks	9
2.1.1 Calcium	9
2.1.2 Paul trap	10
2.1.3 Laser systems	14
2.1.4 Magnetic resonance coil	18
2.1.5 Imaging system	18
2.2 Optical layout	19
2.2.1 Cooling beams	20
2.2.2 Raman beams	21
2.3 Control of the experiment	23
3 Photoionization	26
3.1 Geometric factor	26
3.2 Photoionization cross section	27
4 Single qubit Rabi flopping experiments	29
4.1 Fluorescence, Doppler cooling and qubit initialization	30
4.2 Qubit Readout	30
4.3 Basic concepts in magnetic resonance	33
4.3.1 Rabi flopping	33
4.3.2 Ramsey and Spin echo	34
4.4 Magnetic resonance experiments	35
4.4.1 Determining the qubit splitting	35
4.4.2 Rabi flopping and coherence time	38
4.5 Raman transitions and coupling to the motion	39
4.5.1 Characterisation of the Raman beams	41
4.5.2 Sideband spectrum of a single ion	44

5	Cooling	47
5.1	Notes on Cooling and Diagnostics	47
5.1.1	Cooling Processes	47
5.1.2	Temperature Diagnostics	49
5.2	Continuous Raman Sideband Cooling	51
5.3	Red Detuned Continuous Cooling	55
5.3.1	Fluorescence spectrum	56
5.3.2	Temperature measurements	64
5.4	‘EIT’ cooling	68
5.5	Pulsed sideband cooling	70
5.5.1	Conclusions	72
6	Cooling two ions	74
6.1	Dynamics of two trapped ions	74
6.1.1	Normal modes	74
6.1.2	Quantisation of the motion	75
6.1.3	Determining the qubit state	76
6.1.4	Temperature diagnostics	77
6.2	Experiments	80
6.2.1	Continuous Sideband Cooling	80
6.2.2	Pulsed sideband cooling	83
6.3	Conclusions	84
7	$^{43}\text{Ca}^+$	85
7.1	Why change isotope?	85
7.2	Modelling $^{43}\text{Ca}^+$	86
7.2.1	Rate equations	89
7.3	Program results	90
7.3.1	Cooling with the 393 laser	90
7.3.2	Cooling with multiple 397 frequencies	91
7.3.3	Cooling using circularly polarised 397 light	93
8	Conclusion	96
A	Photoionization publication	100
B	Rate equations code	101

Chapter 1

Introduction

The implementation of quantum information processing (QIP) is a subject of great interest in many areas of physics. Techniques developed in atomic physics for high resolution spectroscopy and metrology applications are almost uniquely suited for the task of implementing quantum information processing. The world of metrology and atomic clocks has advanced by developing extremely precise control over quantum systems, and indeed the Ramsey split pulse method can be recast as the manipulation of single qubit systems.

The use of laser cooled trapped ions for metrology has advanced rapidly over the last 25 years. Frequency standards based on optical transitions in trapped ions (rather than microwave transitions in neutral atoms) are becoming increasingly accurate, and are poised to overtake the cesium standard[1]. Meanwhile, ion trap quantum computing is arguably the most successful of the raft of physical systems under investigation for QIP potential, with on demand production of entangled states[2] and teleportation of quantum information[3, 4] achieved as well as a demonstration of basic error-correction[5, 6].

This introductory chapter briefly outlines the properties of trapped ions which make them suitable for QIP and describes quantum gates, including the one we are working towards implementing, before giving a summary of the work presented in this thesis.

1.1 Quantum computing in an ion trap

The network model of a quantum computer, based on a register of qubits and a fixed finite set of gate operations, was proposed by Deutsch[7]. To implement a quantum algorithm, such as Shor's factoring algorithm[8], we start with an initialized quantum register. This is then fed through a network of quantum gates, which act on both individual and collections of two or more qubits. In addition to these gates there are also measurements of individual qubits, both within the network for the purposes of error correction, where the results influence subsequent gate operations, and at the end of the network, where the result of performing the algorithm is obtained.

DiVincenzo criteria

The requirements on a physical system and our control over it which must be met for it to be used as described above were first outlined by Deutsch. A more extensive discussion is summarised by the DiVincenzo criteria[9] which are listed below (in italics). We explain how they are met by our system.

1. *A scaleable physical system with well-characterised qubits*

The first of these criteria calls for well-characterised qubits. These qubits are provided by the trapped ions, each ion embodying a qubit in its internal state. The majority of experiments in this thesis are concerned with $^{40}\text{Ca}^+$, and the qubit basis states are the two Zeeman sublevels of the ground state. The ion trap group at the University of Innsbruck use one of these sublevels as a qubit basis state, the other being a sublevel in the metastable $3D_{5/2}$ level. The ion trap can be scaled up in two ways. For a small number of qubits, holding all the ions in a single harmonic potential is possible. For larger number of ions the ‘quantum CCD’ has been proposed[10], in which a segmented electrode structure is used to transport individual ions from storage areas to interaction regions where gates, measurement *etc.* can be performed. Segmented linear traps are already in operation[4], and theoretical work has been performed within our group in preparation for making such a move[11].

2. *The ability to initialise the state of the qubits to a simple fiducial state, such as $|000\dots\rangle$*

This is easily performed with a set of ions, by use of optical pumping to transfer the ion into (in the case of our $^{40}\text{Ca}^+$ qubit) one of the Zeeman sublevels. The original Cirac and Zoller[12] scheme also uses as an auxiliary qubit a motional mode of the ion string. In this scheme, the motional mode must be cooled to the ground state to prepare this qubit.

3. *Long relevant decoherence times, much longer than the gate operation time*

The intrinsic decoherence rate of a qubit based on two sublevels in the ionic ground state is very low, due to the extremely small probability of decay from the upper state to the lower. Decoherence is caused by uncontrolled interaction of the qubit with its environment.

The largest decoherence effect for Zeeman sublevel qubits in $^{40}\text{Ca}^+$ is phase decoherence caused by fluctuating magnetic fields, producing decoherence times $\sim 1\text{ms}$ [13]. By use of isotopes with hyperfine structure it is possible to use two sublevels for the qubit which are magnetic field insensitive. Coherence has been observed on such a transition in a single trapped ion on a timescale of many minutes. The maximum speed of gate operations depends on the specific gate used but for a broad range of gates $\tau^{-1} \sim \eta\Omega$, the Rabi frequency on the first sideband. To avoid exciting carrier transitions, $\Omega^2 \ll \omega_z^2$, ω_z being the trap frequency. Gate times of order 10–100 μs have been observed with good fidelity. Techniques exist to reach 2-qubit gates at and above ω_z [14].

4. *A “universal” set of quantum gates*

In practice we only need to be able to implement a single two qubit gate (such as a two qubit phase gate) because it is possible to create a universal two qubit gate by combining this gate with single qubit gates. The 2-qubit gate is the most difficult aspect of ion trap computing at present, and discussion of quantum gates will be postponed until later in this section.

5. *A qubit-specific measurement capability*

Most readout methods in ion traps make use of the electron shelving technique[15, 16, 17], where the two qubit basis states are mapped onto two states of the ion which have radically different behaviour under application of radiation. One of these states is strongly fluorescing when the radiation is applied, and the other produces no fluorescence. In this way the internal state can be amplified into a macroscopic signal. Details of how we perform this mapping for our qubit are given in chapter 4.

1.1.1 Quantum gates

We will now return to the fourth criterion and discuss the ability to cause two qubits to interact so as to generate a two qubit gate.

‘Bus qubit’ gates

The first experimental scheme for quantum computing with ions was proposed by Cirac and Zoller in 1995[12]. In this scheme two (or more) ions are held in the same potential and cooled to the ground state of at least one of the axial modes. This motional mode is then used as an auxiliary ‘bus’ qubit, mediating interactions between ions.

There are two main difficulties associated with this scheme. The first is the stringent temperature requirements. Because a motional state is used as a qubit, it has to be initialised by cooling to the ground state. In addition, the other axial mode (or modes if more than two ions are present) have to be cooled, at least into the Lamb-Dicke limit, as the Rabi frequency of the driven mode depends on the degree of vibrational excitation on the other modes (the Debye-Waller effect[18]).

The other difficulty is that of the need for individual addressing of the ions. For two ions in a trap with axial frequency 500 kHz the ion separation is $9 \mu\text{m}$. Taking into account the geometry of the pair of beams we use to drive motion changing transitions, if the beams were Gaussian, and focussed on one of the ions with a waist of $5 \mu\text{m}$, then the other ion would be driven with an (effective) Rabi frequency of $\sim 1\%$ that of the correct ion.

The original scheme requires, in addition to the two levels which form the qubit, a third ‘auxiliary’ level to be present to complete the gate operation. However, this can be avoided. The Rabi frequency for driving the transition $|\downarrow n\rangle \leftrightarrow |\uparrow n\rangle$ is a function of the motional state n and of η , the Lamb-Dicke parameter. By picking a so-called ‘magic’ value of η it is possible to drive the carrier such that the spin state is swapped if $n = 0$ and is not if $n = 1$, thus achieving a CNOT operation between the bus and the ion[19].

This original Cirac-Zoller scheme has been implemented for two ions to demonstrate the fundamental CNOT gate[20] and for three ions to demonstrate quantum teleportation[3] and the generation of GHZ and W tripartite entangled states[21].

‘Warm ion’ gates

The ability to drive gate operations which do not require ground state cooling would remove one of these stringent requirements. What this means is that we want a gate that, while it can make use of the vibrational modes to perform its operation, works in a way that is independent of the vibrational state the ions started in. One such gate was proposed by Sørensen and Mølmer in 1999[22].

Each ion is addressed by a separate laser beam, each of the same power. The beam incident on the first ion has a detuning of $\omega_z - \delta$, close to the first blue sideband transition whereas the detuning of the beam on the second ion is set to the negative of the first beam’s detuning, $-\omega_z + \delta$. An energy level diagram of the four internal states and one of the vibrational ladders is shown in figure 1.1, and as can be seen, these two beams connect, via Raman transitions, the $|\downarrow\downarrow\rangle|n\rangle$ state to $|\uparrow\uparrow\rangle|n\rangle$. There are two possible paths for the transition and the Rabi frequency of the process is the sum of the frequencies for the two paths. Assuming both beams have equal intensity and Lamb-Dicke parameter

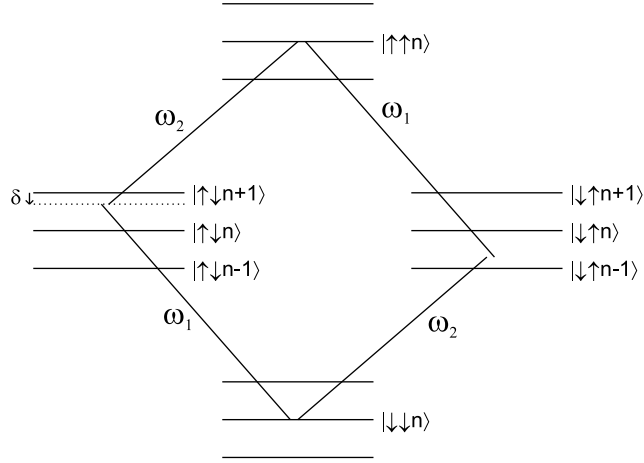


Figure 1.1: Energy level diagram for describing the Sørensen-Mølmer gate[22]. The internal state of the two ions and one of the axial modes are shown. In the original gate each of the ions is addressed by a single laser beam, ion 1 (2) by a beam of frequency ω_1 (ω_2). The beams have equal but opposite detunings from the ionic resonance such that they are detuned a small amount from a first sideband transition. The Raman transition $|\downarrow\downarrow\rangle \leftrightarrow |\uparrow\uparrow\rangle$ is driven by two routes. These destructively interfere in such a way as to make the transition Rabi frequency independent of the motional mode $|n\rangle$ the ion is in, provided it is in the Lamb-Dicke regime.

then the overall Rabi frequency for the process is, in the Lamb-Dicke limit,

$$\bar{\Omega} = \frac{(\eta\Omega\sqrt{n})^2}{2\delta} + \frac{(\eta\Omega\sqrt{n+1})^2}{-2\delta} = -\frac{(\eta\Omega)^2}{2\delta} \quad (1.1)$$

where $\eta\Omega\sqrt{n}$ ($\eta\Omega\sqrt{n+1}$) is the single photon Rabi frequency for transitions which change the motional state from $n \rightarrow n+1$ ($n \rightarrow n-1$) and δ is the detuning of the two lasers from the motional sideband. As can be seen, the two different paths interfere destructively in such a way that the Rabi frequency for the $|\uparrow\uparrow\rangle \leftrightarrow |\downarrow\downarrow\rangle$ transition is independent of the motional state and thus ground state cooling is not required. As presented the gate requires individual addressing. However if instead both beams interact with both ions then the gate will still drive the $|\uparrow\uparrow\rangle \leftrightarrow |\downarrow\downarrow\rangle$ transition in a motion independent way, but will also drive $|\uparrow\downarrow\rangle \leftrightarrow |\downarrow\uparrow\rangle$.

This gate can also be used to entangle more than two ions, as long as they are all illuminated by the two beams[23]. This technique has been used by the NIST Ion Storage group to entangle four ions[2].

In the gate operation a time $\tau = 2\pi\delta/(\eta\Omega)^2$ is required to obtain a complete flip of the ions' internal states. To avoid excitation of the ions into the intermediate states requires $\eta\Omega \ll \delta$, and to avoid exciting the carrier transition $\delta \ll \omega_z$, where ω_z is the trap frequency. This leads to the requirement that the gate time τ has to be several orders of magnitude greater than $1/\omega_z$. This means the gate as described is very 'slow' compared with the cold gate described above.

The slowness is a consequence of the fact that we did not wish to excite the ion into the intermediate levels, which have different motional states, during the Raman transition. Excitation to these intermediate levels during the gate does not however have to cause decoherence providing that the ion returns to its original motional state at the end of the

gate operation.

A phase gate which works by exciting the motion into coherent states during the gate was proposed[24] and shortly after it was shown that a Sørensen-Mølmer gate that was driven faster than originally thought possible could also work in the same way, accessing coherent motional states during the gate but ending in the original motional state[25]. This makes the speed similar to the original cold Cirac-Zoller gate.

‘Wobble’ gate

The gate we intend to perform in our trap is a variant of the phase gate presented in [24] which has been realised by the NIST group to entangle two ions with high fidelity[26]. It has also been used to realise a three ion phase gate in the generation of a GHZ state[27]. It is known informally in our group as the ‘wobble’ gate due to its effect on the ions’ motion, as will be seen.

A coherent state $|\alpha\rangle$ is a superposition of simple harmonic oscillator states which is an eigenstate of the annihilation operator[28], and has the properties that it is a minimum uncertainty wavepacket which evolves as a classical harmonically bound particle (*i.e.* $\langle x \rangle$ and $\langle p \rangle$ obey the classical equations of motion). A classical motion or a coherent state can be identified by a complex number α whose magnitude is proportional to the amplitude of oscillation and phase is the phase of the oscillation. By acting on a coherent state with a force oscillating (near) resonantly with the vibrational frequency α is changed, and by studying a classical oscillator we can see what happens to a coherent state acted on by the same force. The motional state is most easily visualised by looking at the change in α on an Argand diagram.

If the force is resonant with the natural frequency of the harmonic oscillator then the state α is translated linearly (consider a classical oscillator starting at rest - a resonant force will cause the particle to oscillate with larger and larger amplitude, in phase with the force). If the force is not resonant then the motion of the coherent state in phase space is in a circular path. Again consider a classical oscillator at rest. If acted on by an off resonant force then it will start moving and the magnitude of its motion will grow. As the driving oscillation is not at the same frequency as the particle’s natural frequency, while the initial motion was in phase with the driving force, a phase difference will grow between the two, until the drive is π out of phase with the motion. At this point the magnitude of the motion is at its greatest because now the out of phase drive reduces the particle’s motional amplitude, returning it to rest just as the two oscillations return to being in phase with each other.

To perform the wobble gate, two laser beams with a frequency difference close to the stretch motional mode are applied to the ion (alternatively, the centre of mass mode could be used). The two beams will interfere and produce a travelling standing wave which, because of the polarisations picked for the two beams, causes the polarisation of light at a fixed point in space to oscillate between σ^+ and σ^- at the difference frequency. The two internal states used in our ion for the qubit ($|\uparrow\rangle/|\downarrow\rangle$) experience a time varying light shift gradient, and thus force, which is of opposite sign for the two different internal states. As the ions are separated in space, they experience these forces with different phases. We consider the case that the ions are separated by an integral number of wavelengths of the standing wave, and thus the forces acting on them are in phase.

Consider the case where the ions are in the internal state $|\uparrow\uparrow\rangle$. They each experience a force with the same phase and, since to excite the stretch mode of the ion pair the ions

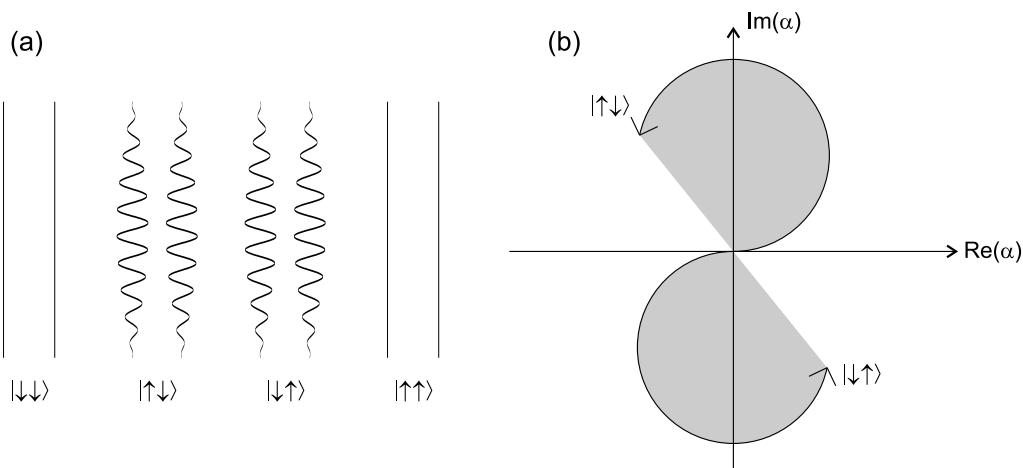


Figure 1.2: The ‘wobble’ gate. State selective forces are used to drive the ions at a frequency close to the stretch mode. If the ions are in the same internal state then the ions are driven in phase and the stretch mode is not driven. If the ions are in different internal states the ions are driven out of phase, and the stretch mode is excited. Since the drive is not resonant with the motional mode the amplitude of motion oscillates at the difference frequency. (a) Motion of the ions for the four possible internal states. The horizontal axis represents displacement, the vertical time. Ions oscillate if their internal states differ, returning to rest after a time $\tau = 2\pi/\delta$. (b) Phase space for ion motion, in a frame rotating at the oscillation frequency. α uniquely defines the dynamics of the normal mode motion, both classically and for a coherent state. The motion of the ion in phase space is described by a circle, a complete revolution completed in time τ . The motion produces a phase, proportional to the area enclosed by the circle.

must move in anti-phase, this mode is not excited. The centre of mass mode could be excited, however it is far from resonance so is only excited weakly. The same situation occurs if the ions are in $|\downarrow\downarrow\rangle$. If however the ions are in $|\uparrow\downarrow\rangle$ or $|\downarrow\uparrow\rangle$, then the forces will be in opposite direction, and thus able to excite the stretch mode, at a frequency close to resonance (see figure 1.2a). The evolution of the coherent state (*i.e.* the value of α) can be plotted on an Argand diagram. The state starts at rest ($\alpha = 0$) and then the amplitude of the motion rises then falls, with the motion describing a circle on the Argand diagram, returning to the origin after a time $\tau = 2\pi/\delta$, where δ is the detuning of the difference frequency from the stretch mode frequency, see figure 1.2b. Thus after a time τ the ions have returned to their original motional state, however due to their motion they acquire a phase equal in magnitude to the area of the circle they inscribed in the α Argand diagram. Although the value of phase is determined by an area (and can be described as a geometric phase) it could also be evaluated by integrating the motional energy of the system over the course of the gate (and thus described as a dynamic phase). The spin-dependent phase which results from this operation is precisely that required for a 2-qubit phase gate when the enclosed area represents a phase $\pi/2$.

The motional state at the start of the gate operation does not in general have to be a coherent state (the motional ground state $|n = 0\rangle$ is the coherent state with $\alpha = 0$), the above treatment being correct to good approximation if the ions are in the Lamb-Dicke regime.

1.2 Summary of the thesis

This thesis is concerned with the loading, cooling, manipulation and measurement of single ions, or pairs of ions, in experiments designed to achieve the level of single-qubit resolution and coherence required for studying quantum information. It forms part of a larger work developed over the course of 8 years in the ion trapping group at Oxford University. At the outset of the work discussed here, the group had observed single trapped ions and few-ion crystals of $^{40}\text{Ca}^+$ and performed a careful study of dark resonances in order to characterise laser intensities and polarizations and the magnetic field at the ion. The spin-state of a single $^{40}\text{Ca}^+$ ion had been measured at high magnetic field ($\sim 100\text{ G}$)[29] but not at low field. The ions were laser cooled to around but not below the Doppler limit associated with the strong 397 nm transition in the ion ($\sim 540\ \mu\text{K}$).

A method to measure the spin state at arbitrary (i.e. including low or zero) field was developed and implemented successfully in 2002/2003 and formed a major theme of the D. Phil. thesis of M. McDonnell [30, 31], the method is outlined here in chapter 4. In the same period we first implemented photoionization and thus selectively loaded each of the long-lived isotopes of calcium into our ion trap. Details of the experimental setup, a discussion of the expected selectivity and some of our early data may be found in the D. Phil. thesis of J.-P. Stacey[32]. I constructed the laser source at 389 nm and carried out experimental studies of the selectivity and efficiency, the main results of which are presented here (see below).

The work presented in this thesis has three major themes: photoionization, coherent manipulation by Rabi flopping and related techniques, and cooling to the ground state of motion. The techniques are applied primarily to single trapped ions, and preliminary work with a pair of trapped ions is reported.

Chapter 2 describes the experimental apparatus, covering amongst other things the trap itself and the various laser systems, particularly those used in the cooling experiments. Several of these were installed in the course of the current work, including for example the master-slave system producing the Raman beam pair which we use to drive coherent evolution.

Our studies of photoionization of neutral calcium as a means to load calcium ions into a Paul trap are described in an article published in Physical Review A and included here in appendix A. Some further information is presented in chapter 3. Photoionization allows the ionization and loading of specific isotopes of calcium into the ion trap[33, 34]. In a non-isotopically enhanced sample of calcium, such as we use, almost 97% of the sample is ^{40}Ca . This isotope was chosen for all the manipulation and cooling experiments described in this thesis. However it is an important consideration that the rare isotope ^{43}Ca (0.135% natural abundance) has hyperfine structure and magnetic field-insensitive transitions, and will be the natural candidate for the next round of experiments where higher precision manipulation and measurement of the qubits is desired.

Chapter 4 concerns preparation, manipulation and readout of a qubit. We use magnetic resonance to manipulate a qubit stored in the spin (i.e. Zeeman sublevels) of the ground state of $^{40}\text{Ca}^+$. The magnetic resonance allows us to measure the qubit splitting accurately and once this is found we use the magnetic resonance to coherently manipulate the qubit, driving Rabi oscillations between the two spin states. We describe the implementation of Ramsey pulse sequences for measurement of phase changes and the use of spin-echo pulses to reduce errors in phase measurement due to slow drifts in the magnetic field and thus the qubit splitting. We also discuss using Raman transitions to drive spin transitions

which also involve changing the motional state of the ion. Finally we use magnetically driven Ramsey spin-echo sequences to measure the phase change induced in an ion when circularly polarised far from resonant light causes a light shift on the qubit states. This allows us to make a precise measurement of the intensity of the two beams we use to drive Raman transitions.

Chapters 5 and 6 are concerned with the cooling and temperature diagnostics of one and two ions, by sideband cooling techniques. We implemented three different forms of sideband cooling. All involved Raman transitions; two were continuous, the other pulsed. The continuous methods have been little explored up till now. In principle all three methods could allow a similar cooling rate and final temperature to be attained, but in practice technical issues make some more convenient than others. We present evidence of cooling to near the ground state of motion by all three methods, as well as related information on cooling and heating rates.

Chapter 7 concerns the planned move to working with the isotope ^{43}Ca . A computer program to set out and solve numerically the rate equations for laser excitation of the low-lying energy levels is described. This enables us to plan the laser system for cooling and detection and study issues such as preparation of the qubit state by optical pumping.

Chapter 8 concludes.

Chapter 2

Apparatus

This chapter describes the experimental apparatus used to manipulate our calcium ions.

The first section describes the main building blocks of the experiment, such as the calcium ion, the ion trap, laser systems, a magnetic resonance coil and the imaging system.

The second section covers in more detail the optical layout of the experiment, particularly the optics which bring light from the 397 cooling and 397 master-slave lasers to the ion trap.

The final short section covers some details of the control of the experiment by computer, in particular details of the control of pulse sequencies and the setting of the Raman detunings of the two sets of Raman beams.

2.1 Building blocks

2.1.1 Calcium

We use calcium in all the experiments described in this thesis. Neutral calcium is ionised in a two-stage photoionisation processes, which is discussed in chapter 3 and appendix A. The transitions for this process are shown in figure 2.1a. The lower lying energy levels of Ca^+ are shown in figure 2.1b. Wavelengths of relevant transitions in $^{40}\text{Ca(I)}$ and $^{40}\text{Ca(II)}$ are given in table 2.1.

We use $^{40}\text{Ca}^+$ in all the cooling and qubit manipulation experiments in this thesis. This isotope has no nuclear spin and so has no hyperfine structure. The degeneracy of the Zeeman levels is lifted by an applied magnetic field. We use the two sublevels of the $4\text{S}_{1/2}$ ground state as our two qubit states. The Zeeman splitting of these two states is

	Transition	Wavelength / nm
Ca(I)	$4^1\text{S}_0 \leftrightarrow 4^1\text{P}_1$	422.792
	$4^1\text{P}_1 \leftrightarrow \text{Ca(II)}$	389.808
Ca(II)	$4\text{S}_{1/2} \leftrightarrow 4\text{P}_{1/2}$	396.95865
	$4\text{S}_{1/2} \leftrightarrow 4\text{P}_{3/2}$	393.477304
	$3\text{D}_{3/2} \leftrightarrow 4\text{P}_{1/2}$	866.45134
	$3\text{D}_{3/2} \leftrightarrow 4\text{P}_{3/2}$	850.03547
	$3\text{D}_{5/2} \leftrightarrow 4\text{P}_{3/2}$	854.44335

Table 2.1: List of wavelengths for selected transitions in neutral and singly ionised ^{40}Ca

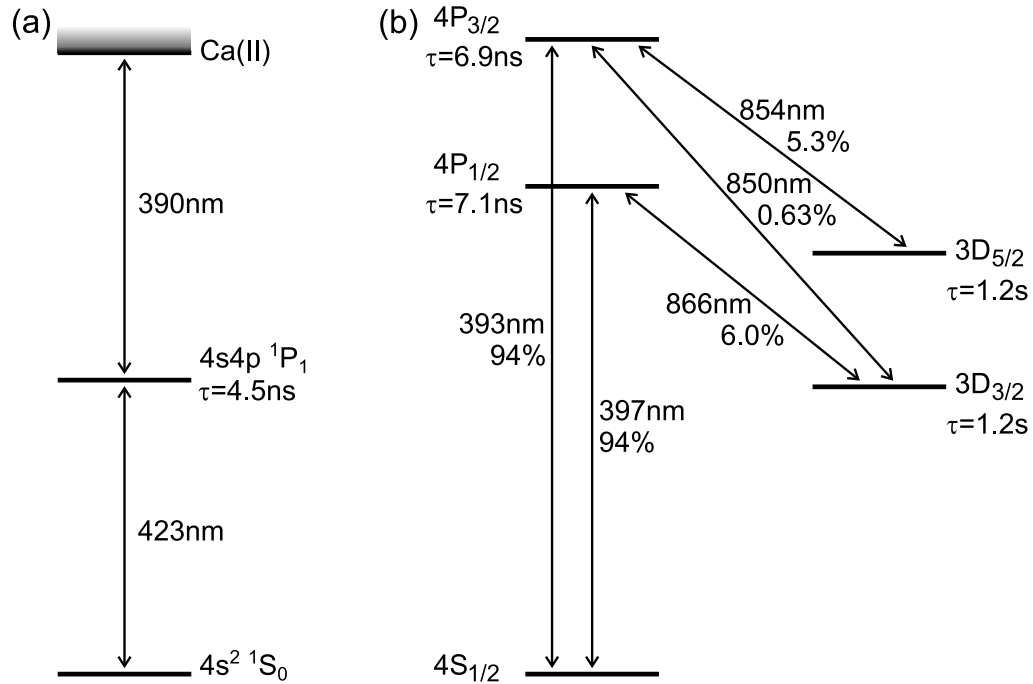


Figure 2.1: Energy level diagrams for selected levels in (a) neutral and (b) singly ionised calcium.

2.8 MHz/G.

2.1.2 Paul trap

Electric fields are useful for confining ions. Unlike in traps for neutral atoms, the ions can be trapped in very deep and tightly-confining potential wells and the trapping potential does not depend on the internal state. However it is not possible to trap charged particles in all three dimensions using only static electric fields.

There are two common types of ion trap: Penning and Paul traps.

A Penning trap combines two static fields, one electric and one magnetic. The electric field confines the ions along the z direction, while in the x - y plane it is anti-trapping. The magnetic field is in the z direction causing the ions' motion in the x - y plane to be a combination of two circular motions which prevent their expulsion from the trap. No quantum information experiments involving more than one qubit have been performed in a Penning trap as yet, although work towards this goal is progressing[35].

The Paul trap uses time-varying electric fields to confine ions. We use a linear Paul trap, in which an oscillating electric field provides radial confinement and a static electric field provides confinement along the z -axis. Figure 2.2 shows the six electrodes which form our trap. The two electrodes which lie on the z -axis are the endcap electrodes, and a positive voltage is applied to them, to produce confinement of our positively charged ion in the z direction. As with the Penning trap, this field also provides an expelling force on the ion in the x and y (radial) directions.

The four electrodes which lie equally spaced from the z -axis produce a quadrupole potential in the x - y plane. The electrodes are cylindrical in shape, which means that the field produced has small components of higher order multipole potentials, however close

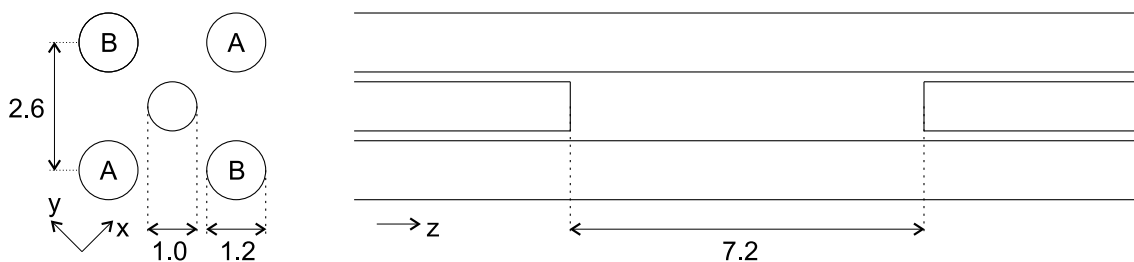


Figure 2.2: The linear Paul trap. The trapping electrodes are seen end on and from the side. Dimensions are indicated in mm.

to the axis these have negligible effect on the ion. The figure shows the orientation of the trap as it is found on the optical table. In the coordinates indicated in the figure, the potential energy of a (singly charged) ion is $U = eQ(x^2 - y^2)$ where Q is a quantity with dimension of voltage divided by distance squared.

If $Q > 0$ then the potential confines along x and expels along y , and vice versa if $Q < 0$. In the Paul trap Q oscillates as $Q = Q_0 \cos(\Omega t)$. When the r.f. frequency Ω is high enough, the motion of a charged particle in the potential consists of fast small oscillations at the r.f. frequency (this is called micro-motion) superimposed on a relatively slower simple harmonic motion about the trap centre, called secular motion. The classical dynamics are described in detail elsewhere[36, 37, 38]. We give several basic results, using similar notation to [39].

The voltage applied to the endcap electrodes is V_z , while that applied to the pair of electrodes labelled A is $V_A = V_{ac} \cos(\Omega t)$, and $V_B = -V_A$. The electric potential can be written

$$V(x, y, z, t) = Q_{ac}(x^2 - y^2) \cos \Omega t + Q_z \left(z^2 - \frac{x^2 + y^2}{2} \right), \quad (2.1)$$

where

$$Q_{ac} = \alpha_{ac} V_{ac} / \rho_0^2, \quad (2.2)$$

ρ_0 is the distance from the centre of the trap to the nearest part of the quadrupole electrodes, equal to 1.22 mm, and α_{ac} is a dimensionless factor depending on the geometry of the electrodes. Similarly

$$Q_z = \alpha_z V_z / z_0^2, \quad (2.3)$$

z_0 being the distance from the trap centre to the endcaps, equal to 3.6 mm, and α_z is another geometrical factor. These geometric factors have been measured as $\alpha_z = 0.10$ and $\alpha_{ac} = 1.1$ [39].

Motion along the z direction is harmonic, and depends only on the endcap voltage. The frequency of oscillation is

$$\omega_z = \sqrt{\frac{2eQ_z}{M}} \quad (2.4)$$

The equation of motion for one of the radial directions can be written

$$\frac{d^2 x}{d\tau^2} + [a_x - 2q_x \cos 2\tau] = 0 \quad (2.5)$$

where

$$\tau = \frac{\Omega t}{2}, \quad a_x = -\frac{4eQ_z}{\Omega^2 M}, \quad q_x = \frac{4eQ_{ac}}{\Omega^2 M}. \quad (2.6)$$

Equation 2.5 is known as the Mathieu differential equation. The analytic solution to this equation is an infinite sum of exponentials. The lowest order terms of the sum give

$$x \simeq x_0 \cos(\omega_r t + \phi) \left(1 + \frac{1}{2} q_x \cos \Omega t\right) \quad (2.7)$$

where

$$\omega_r = \frac{\Omega}{2} \sqrt{\frac{q_x^2}{2} + a_x} = \sqrt{\omega_{r0}^2 - \omega_z^2/2}, \quad \omega_{r0}^2 = \Omega^2 q_x^2/8. \quad (2.8)$$

This solution is valid when $|a_x|, q_x^2 \ll 1$

A useful insight into the time-averaged effect of the r.f. potential is to regard it as providing a ponderomotive pseudopotential[36, 37].

$$U_p = \frac{|\nabla U|^2}{4m\Omega^2} \quad (2.9)$$

The secular motion can then be regarded as motion in this pseudopotential. Simple harmonic motion is therefore obtained when $|\nabla U|^2$ is quadratic in position, as for example for a quadrupole.

The slow harmonic motion of the ion in the pseudopotential with frequency ω_r has the high frequency micromotion at the RF drive frequency Ω superimposed upon it. For this approximation to be valid $q_x^2 \ll 1$ and so the amplitude of the micromotion is smaller than that of the secular motion. The motion in the y direction can be treated in the same way.

When the classical motion is quantised, in the z direction the motion is simple harmonic, the quantisation of which is standard. When the motion in the radial directions is quantised, the wavefunction is periodic in $2\pi/\Omega$, and when $\Omega t = 2n\pi$, the wavefunction is approximately that of an SHO of frequency ω_r [40]. This non-stationary, periodic nature of the wavefunction is a consequence of the time dependence of the trapping potential.

The endcap voltages are provided by two channels of an EMCO Octo-channel high voltage system. The output voltage of each channel is in the range 0–1000 V, and is programmed by an applied voltage in the range 0–5 V. Each voltage is set separately, so that the centre of the trap can be moved along the z axis. The maximum voltage we apply to the endcap electrodes is 700 V, because higher voltages cause electrical breakdowns inside the vacuum system. 700 V produce an axial secular frequency $\omega_z = 2\pi \cdot 812$ kHz.

The quadrupole electrodes are driven by a non-linear oscillator circuit called a Colpitts oscillator which produces two output voltages of equal magnitude but in anti-phase, as well as a ‘monitor’ voltage with amplitude 1/200th of the output voltage[39]. When the oscillator is connected to the trap electrodes, the frequency of the output is 6.29 MHz, and the output voltage amplitude can be varied up to a maximum of 120 V. This means that the maximum value of ω_{r0} is $2\pi \cdot 1.2$ MHz.

RF compensation

In addition to the six main trapping electrodes described above, and shown in the figure, a further four electrodes which lie further out from, and parallel to, the trapping electrodes are present. These are called the compensation electrodes.

Consider the effect of a static electric field in the vertical direction. The force from this field pushes the ion away from the centre of the quadrupole. Whereas an ion at the centre of the quadrupole field will not experience any forces from the oscillating field, if the ion is forced away so that the centre of the trap does not correspond to the centre of

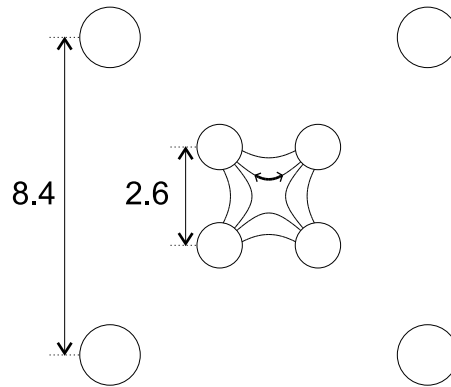


Figure 2.3: Compensation and RF electrodes. If the ion is displaced from the centre of the quadrupole then it will experience non-zero oscillating fields, and be driven along the electric field lines at the drive frequency. A vertical displacement as shown in the figure produces horizontal motion, and thus a horizontal laser beam is sensitive to a vertical displacement. The lower two compensation electrodes are earthed, and voltages are applied to the upper two electrodes. Dimensions in mm, displacement of the ion from the centre of the trap is exaggerated.

the quadrupole, the ion will oscillate with the quadrupole, at the drive frequency Ω . The compensation electrodes have dc voltages applied to them to cancel out any fields that move the ion from the quadrupole centre. Two of these electrodes are earthed, the other two controlled by the Octo-channel system in the same way as the endcaps.

We use two different methods for setting the voltages on the compensation electrodes. Both make use of the effect that ionic motion has on the scattering of the incident cooling radiation. As can be seen in figure 2.3, vertical displacement of the ion results in horizontal oscillation of the ion, and so laser beams lying in the horizontal plane are sensitive to vertical displacement, and similarly, a vertical beam is needed to detect horizontal displacement. As the 397 nm laser detuning is scanned over the ionic resonance, the scattering rate should take a half Lorentzian lineshape. Motion of the ion at the drive frequency causes the lineshape to be broadened and take a non Lorentzian shape. By minimising the width of this resonance, the compensation voltage can be crudely set.

A more precise setting is obtained by RF correlation. The 397 laser is detuned so that the scattering rate is approximately half the rate at the peak of the resonance. This is the point at which the scattering rate is most sensitive to detuning (and thus Doppler shift) for a Lorentzian lineshape. Micromotion at the drive frequency results in correlation between the arrival time of photons at the detector and the RF phase. By minimising this correlation for two different beams, one with a component in the horizontal direction, the other with a component in the vertical direction, the compensation voltages can be accurately set[32].

Determining the secular frequencies

To determine the secular frequencies, a signal generator is capacitatively coupled to one of the endcap electrodes. This is used to provide an oscillating ‘tickle’ voltage which drives the ion motion. When the frequency comes close to one of the secular frequencies then the amplitude of oscillation of the ion is resonantly enhanced. This motion causes

the fluorescence rate of the ion to be altered which we detect. This method permits the resonant frequencies to be measured to an accuracy of ~ 1 kHz. Because the ‘tickle’ voltage is applied to an endcap, axial motion is much easier to excite than radial motion.

2.1.3 Laser systems

We have 8 laser systems which are used to produce radiation at the 7 different wavelengths listed in table 2.1. When referring to a laser system, it will be identified by the wavelength of the transition it addresses. As there are two laser systems which drive the $4S_{1/2} \leftrightarrow 4P_{1/2}$ transition, one is known as the 397 cooling laser, the other the 397 master-slave.

Lasers

We use exclusively diode lasers in our experiments. The availability of diodes which operate at the transition wavelengths of calcium is one of the advantages of the element, as their ease of use and set-up compared with other common laser technologies used in atomic physics such as dye or titanium:sapphire lasers simplifies the experiment.

The internal cavity of the laser diode is small and very lossy, giving the emitted radiation a wide frequency linewidth. All but one of our laser systems are external cavity diode lasers (ECDLs). The external cavity uses a grating in the Littrow configuration, where the first order diffracted beam is sent back into the diode. The output beam is the zero order reflection from the grating. This feedback forces the diode to lase on one of the external cavity modes, which have a narrower width than the internal cavity modes of the diode. Because of the feedback, the optical power inside the diode head is approximately twice that of the output of the external cavity, limiting the available laser power to half of that at which the laser diode is rated.

The emission wavelength can be coarsely tuned by changing the temperature of the diode and the angle of the grating. For more precise control of the wavelength, the current can be changed, and finally, the grating is on a piezo which can change the length of the external cavity, allowing the wavelength to be tuned continuously.

The laser systems are a mixture of commercial and lab built systems. All the laser systems in use have been described more fully in previous group theses and reports. The 397 cooling[39, 30], 393[30] and 423[32] lasers are commercial ECDL systems manufactured by Toptica Photonics. All three use GaN laser diodes produced by Nichea. The 393 laser uses a 5 mW rated diode, the 397 cooling and 423 lasers 30 mW diodes. The 397 master-slave[30] is also a Toptica system. A 5 mW diode ECDL injects, via the third port of an optical isolator, a ‘bare’ (no grating) 30 mW diode. This allows a full 30 mW output power. Changing the alignment of the grating in an ECDL introduces an angular deviation in the output beam. This can be changed to a displacement of the beam by using a compensation mirror, which rotates with the grating. This compensation mirror is found in all the Toptica systems. In the master-slave system although change in the alignment of the master laser may require realignment into the slave to maintain injection, the beam emitted by the slave diode is not displaced, preserving the alignment down the beam path.

The 866, 854 and 850 lasers are all lab built ECDLs. The 866 and 854 lasers use 50 mW diodes produced by SDL. The 850[32] laser originally used a 50 mW SDL diode, which has recently been replaced with a 150 mW diode.

The 389[41] laser is different from the others, as it does not have to be tuned to a specific wavelength, merely have a wavelength less than the 389.8 nm required for excitation of an excited atom to the continuum. This means that an external cavity was not needed,

simplifying construction. Only temperature stabilisation is required. The diode was again manufactured by Nichia, and was rated at 5 mW. By use of a grating spectrometer, it could be seen that the emission spectrum had the form of a comb of emitted frequencies separated by 59 GHz. This comb is due to the internal diode cavity and is similar to a previous measurement of a UV Nichia diode which found a mode spacing of 65 GHz[39]. The emission wavelength of the strongest mode was measured to be 388.86 nm.

Diagnostics

With the exception of the 389 laser, which has fixed wavelength, we need to be able to match the emission wavelength of our lasers to the atomic transitions to which they correspond. There are two main frequency diagnostics: the wavemeter and the spectrum analyser. A block diagram summarising laser systems and their relations to diagnostics is shown in figure 2.4.

A wavemeter provides absolute measurement of the wavelength of laser light. We use a Burleigh WA-1500 wavemeter. This uses a Michelson interferometer as a Fourier transform spectrometer. By counting interference fringes as the path length of one of the arms is varied, and comparing this number with the number of fringes counted for a stabilised HeNe laser, the wavelength can be deduced. The WA-1500 reports wavenumbers to a precision of 0.001 cm^{-1} . We also sometimes use a Burleigh WA-200 wavemeter, an earlier version of our main wavemeter. This reports wavenumbers to a precision of 0.01 cm^{-1} . Due to misalignment into the wavemeters causing inaccuracy in reading, the final step in setting a laser frequency correctly is to use the response of a trapped ion (or the atomic beam in the case of the 423).

Scanning Fabry-Perot etalons are used as optical spectrum analysers. We define the free spectral range (fsr) to be the frequency separation of longitudinal TEM_{00} modes, $\nu_{\text{FSR}} = c/2L$ where L is the cavity length. The cavities are confocal[42]. This means that all the radially symmetric transverse modes occur at the same frequency, and the antisymmetric modes all occur at a frequency displaced by $c/4L$. We generally excite both symmetric and antisymmetric modes, since very accurate alignment is required to avoid this, and therefore the gap between observed peaks in the signal corresponds to $c/4L$. This permits the observed spectrum to be calibrated (since L is known), but we mostly use the analyzers merely to check that the lasers are single-mode and have not drifted or jumped in frequency with respect to one another.

All the ‘blue’ (393,397 and 423) beams are combined onto one beam path using pbs cubes (or a movable mirror in the case of the 397 master-slave) and sent to one spectrum analyser, which has a free spectral range of 300 MHz, and also to the WA-1500 wavemeter. Similarly, all the ‘red’ (850,854 and 866) beams are combined and sent to a different spectrum analyser, this with an fsr of 2 GHz. The red beams are also sent to a wavemeter, sometimes the same WA-1500 as the blue beams, or when it is available to the WA-200, enabling two laser frequencies to be measured concurrently.

Frequency control

To provide frequency stability, several of our laser systems are locked to Fabry-Perot cavities. These give a signal which is used to provide feedback both to the diode current and the grating position via the piezo.

There are two important physical properties of the reference cavity, its length (and thus fsr) and the reflectivity R . A more convenient measure of reflectivity is given by the

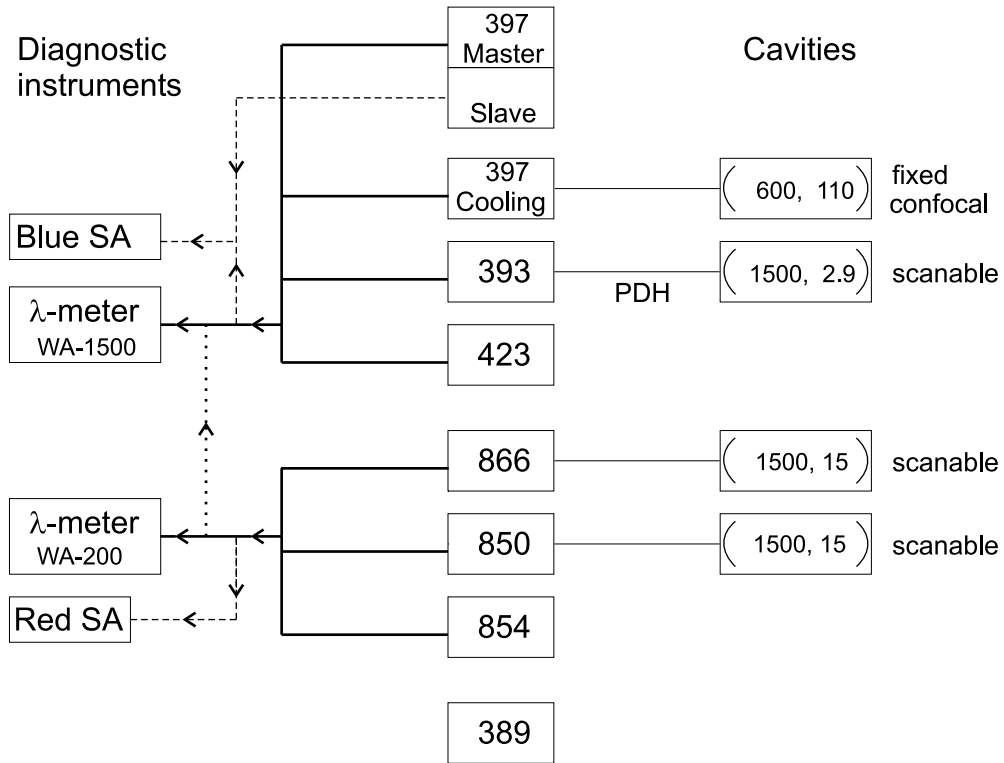


Figure 2.4: Summary of laser systems. Shown are all the lasers we use, and their diagnostics and locking arrangements. All of the diagnostic beams are multiplexed into two beam paths, one for the red beams, one for the blue. White cards are used to block beams to ensure only one is incident on each wavemeter. The WA-1500 wavemeter is used to measure the blue wavelengths. It can also be used to measure the red beams, however that requires the wavemeter to be reset. For this reason a WA-200 wavemeter is used, when it is available, to monitor the red beams. The 397 master-slave system consists of a pair of lasers. Only the master laser is used with the wavemeter. If the slave is injecting correctly (which can be determined from the spectrum analyser) then it will have the wavelength of the master. Also shown are the four reference cavities used for frequency stabilisation. Shown on each cavity is the free spectral range ($c/2L$) and the linewidth of the cavity in MHz.

finesse

$$\mathcal{F} = \frac{\pi\sqrt{R}}{1-R}. \quad (2.10)$$

The free spectral range and the finesse combine to give the linewidth of the cavity, equal to $\nu_{\text{FSR}}/\mathcal{F}$. If we consider the simple ‘side-of-fringe’ lock, where the laser frequency is set so that it is detuned from a cavity mode such that the intensity of transmitted light is half the maximum, the linewidth determines both the sensitivity of the error signal to frequency fluctuations (lower linewidth giving greater sensitivity) and the stability of the lock in response to large fluctuations (lower linewidth giving lower stability).

The parameters of the various cavities are summarised in figure 2.4.

The cavity the 397 cooling laser is locked to has a fixed length of 250 mm, and is confocal. The beam is not aligned so as to match only into the symmetric modes of the cavity, so the fringe separation is given by $c/4L$ and equals 300 MHz. The cavity is low finesse, with a fringe width of ~ 110 MHz, implying a finesse of 5.4. The laser can be scanned over ± 50 MHz by moving the lock-point. The cavity is in a vacuum and temperature stabilised to minimise drift. In the event of the cavity fringes not being at a useful frequency, relative to the atomic transition, the cavity length can be changed by changing the cavity temperature.

The 397 master-slave laser is not locked to a cavity. This is because it is used to drive Raman transitions between the two qubit states with each beam individually at a large detuning (*e.g.* 30 GHz) from the atomic resonance. This detuning is much larger than fluctuations and drifts in the frequency. The effective laser linewidth of the Raman transition is close to zero as both laser fields are derived from this one laser. (See chapter 4 for further information).

The 866 laser, which is used as a repumper during the Doppler cooling process, is side-of-fringe locked to a commercial high finesse cavity supplied by the NPL. The linewidth of the cavity is 15 MHz. The NPL cavities are not confocal, and so care is needed to match the beam into the TEM₀₀ mode of the cavity. The NPL cavities are designed to be highly stable, contained in a vacuum of $< 10^{-6}$ mBar and temperature stabilised. These cavities have one of the mirrors attached to a piezo, enabling the length, and thus the frequency of the fringes to be controlled, enabling the frequency of the locked laser to be varied.

The 393 and 850 lasers are also locked to scannable NPL cavities. These lasers are used to perform the crucial ‘shelving’ step of our qubit readout method, to be described in section 4.2. The effectiveness of the method depends partly on the linewidths of the two lasers. The 850 cavity has linewidth of 15 MHz, and the laser is side-of-fringe locked to it. The 393 laser is locked to its cavity (linewidth 2.9 MHz) using a different lock method, the Pound-Drever-Hall (PDH) method[43, 44]. The linewidth of each laser is estimated to be 1.5 MHz from the error signal obtained. A simple description of the PDH method, and details of our implementation are found in the thesis of McDonnell[30]. The PDH method is capable of creating a narrower laser linewidth for a given cavity linewidth than a side of fringe lock. In addition, it can have a much greater capture range, making it more stable.

The 854 laser, which is used to deshelve the ion from the 3D_{5/2} state, is not locked to a cavity. The intensity of the beam is such that the passive stability of the laser keeps the frequency close enough to the transition frequency for periods of up to several hours at a time.

The 423 laser, used for the first stage of the photoionisation of neutral calcium, is under normal circumstances unlocked. This beam is typically only needed for a period of at most a few minutes when we are loading $^{40}\text{Ca}^+$ ions, during which time passive stability again

keeps the laser at the correct frequency. During some of the photoionisation experiments where higher frequency stability was required, the laser was temporarily locked to the 850 cavity with a side-of-fringe lock.

2.1.4 Magnetic resonance coil

We can manipulate the ions by magnetic resonance as well as by optical methods. An oscillating magnetic field whose frequency is close to the Zeeman splitting frequency of the qubit states will coherently drive population between the two qubit states. The magnetic field coil is part of a tuned circuit, with a resonant behaviour. We want the resonant frequency to match the Larmor frequency of around 4 MHz.

Our tuned circuit consists of a coil, and a variable capacitor in series with it. The coil has 40 turns (in two layers of 20) and a conical geometry, due to the confined space it has to occupy. The variable capacitor is used to change the resonant frequency of the coil. The width of the resonance is ~ 250 kHz. A smaller coil is mounted close to the main coil. This ‘pick-up’ coil is used to monitor the size of the magnetic field generated by the main coil.

The source for the coil is a Stanford DS345. This can produce a sine wave of frequency from 0–30 MHz and amplitude of up to $3.5 V_{\text{rms}}$ (+24 dBm). The output of the Stanford passes through a Minicircuits ZYSWA-2-50DR TTL switch. The input is switched between one of two outputs by a TTL signal, one of which connects to an amplifier and the other is terminated. The switch causes a typical loss of 1.1 dB in the signal, and the isolation is 42 dB. The signal is then amplified by a Frankonia FLL 25 amplifier. The small signal gain of the amplifier is 47 dBm, however the maximum input to the amplifier should be 1 mW (0 dBm, $0.224 V_{\text{rms}}$) which gives 25 W (44 dBm) output. The impedance of the coil/capacitor is not equal to 50Ω , however the Frankonia is very robust and able to perform even under conditions of complete mismatch between its output and the load.

2.1.5 Imaging system

Light emitted by the ion(s) in the trap is collected by a lens system and sent to a PMT or camera. Full details of the imaging optics are given in [39], they are summarised in this paragraph. The first stage images the centre of the trap onto an aperture (the ‘imaging slit’) of size $700 \mu\text{m} \times 870 \mu\text{m}$. The magnification of this stage is 4.1. This aperture, which corresponds to an area of $170 \mu\text{m} \times 210 \mu\text{m}$ inside the trap, serves to reduce the amount of scattered light reaching the PMT and CCD. The aperture is then re-imaged, with magnification 1, onto a PMT. A blue filter is used to reduce counts due to scattered 866 nm light. This two lens imaging optic can have a beamsplitter inserted between the lenses which diverts some of the light to a camera. The aperture is imaged onto the camera with magnification 2, giving a total magnification of 8.2 from the centre of the trap to the camera.

In [39] an image intensifier camera was used. This has been replaced with a CCD device supplied by Andor Technology. The pixel size of the camera is $13 \mu\text{m}$, which corresponds to $1.6 \mu\text{m}$ at the centre of the trap.

In the course of the cooling experiments, we need to detect weak fluorescence where the counts due to the ion were less than the background counts. To improve the signal to noise ratio, a further aperture was inserted into the imaging system. A pinhole of diameter $200 \mu\text{m}$ was placed in the image plane of the second magnification stage, immediately before the PMT. The pinhole reduced the number of background counts by approximately

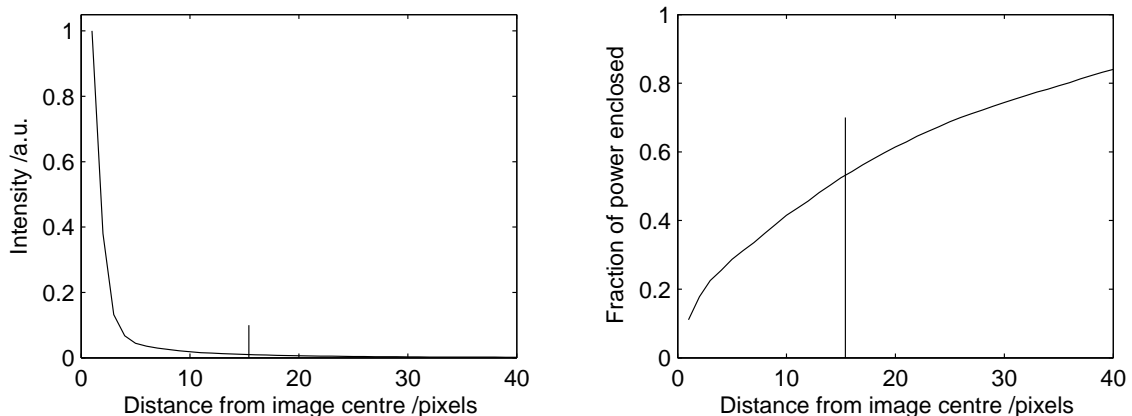


Figure 2.5: (a) Intensity profile of a single ion imaged through the imaging system onto CCD, calculated by integrating over whole image. One pixel corresponds to a distance of $13\ \mu\text{m}$, which corresponds to $1.6\ \mu\text{m}$ at the ion. The pinhole has a radius of $100\ \mu\text{m}$, which due to the $2\times$ magnification corresponds to 15.4 pixels. (b) Fraction of power enclosed by a circle of the given radius, centred on the ion image. 53% of the power for this image lies within a radius of 15.4 pixels.

a factor of 10, (whereas we would expect from the ratio of the area of this hole to the area of the imaging slit a factor of 19). The signal from the ion is also reduced, to $\sim 75\%$ of its previous size. Although a Doppler cooled ion traces out a very small area in space, the imaging system has only a finite resolution so that the CCD image of the ion has a width of approximately 2 pixels. This is still much less than the size of the pinhole, which has a radius corresponding to 15.4 pixels at the CCD, however the camera image of the ion also shows a small intensity of light detected by the CCD at large (>15 pixels) distances from the ion position. Figure 2.5a shows the intensity (in arbitrary units) of light as a function of the distance in pixels from the centre of the image of the ion. Figure 2.5b shows the fraction of the total power enclosed within a circle of given radius. This indicates that the PMT count rate we observe should be $\sim 50\%$ of that before the pinhole was inserted. Presumably when we focus the imaging system to maximise the counts from the PMT, the central part of the ion image blurs out but in such a way that the total power going through the PMT pinhole actually increases.

2.2 Optical layout

The principle optical components delivering light to the trap are described here. A few general notes on the layout will be followed by more detailed explanation of the various 397 nm beams used for cooling and driving Raman transitions.

Immediately following the 397 cooling, 397 master-slave, 393, 866 and 850 lasers is an optical isolator. This serves to prevent light retroreflected by elements further down the beam path from reaching the laser diode, where it would cause instability.

All the laser beams except those for photoionisation are controlled by one or more AOMs which serve as switches as well as frequency shifters. This all-AOM setup, as compared to previous iterations of the experimental layout which included shutters on some of the lasers, allows much faster experimental sequences to be performed. The

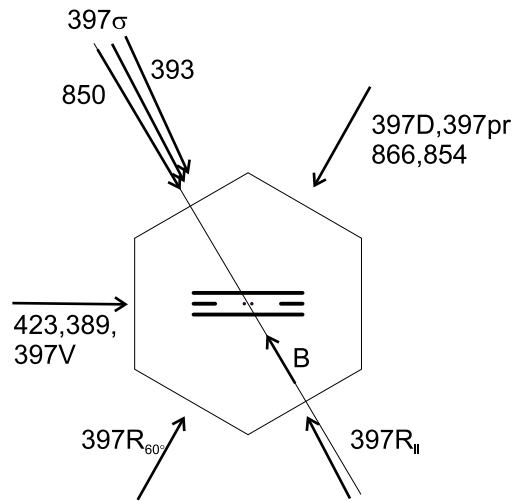


Figure 2.6: Diagram showing the directions the various beams used in the experiment enter the vacuum system. The 423,389 and 397V beams do not lie in the horizontal plane, instead entering the vacuum system through the top window, at an angle of 27° to the vertical.

switching time of AOMs is $< 1 \mu\text{s}$ whereas mechanical shutters can have switching times of milliseconds. Also, mechanical vibrations from shutters may introduce frequency jitter in the lasers. All the ‘blue’ AOMs are manufactured by IntraAction, and are made of UV grade fused silica crystals. The diffraction efficiency of these AOMs is polarisation dependent, being much higher for vertically polarised light (when the AOMs are mounted so that the acoustic wave is horizontal) than horizontally polarised.

A laser passing through an AOM which is nominally off will typically still have a small fraction ($\sim 10^{-3}$) diffracted into the correct order and thus still reach the ion. The total number of AOM passes required to reduce the intensity to an acceptable level depends on the beam.

The 423/389 lasers are controlled by a single shutter. These two lasers and the 850 and 854 lasers are on a different optical table than the vacuum system. To bring the light onto the main table, the 423 and 389 are combined and travel through one fibre, while the 850 and 854 lasers each have their own fibres.

Figure 2.6 shows the directions of the various laser beams as they enter the vacuum chamber. Also shown on this diagram is the magnetic field direction, and the axial trap direction. The photoionization and 397 vertical beams shown do not lie in the horizontal plane in which the other beams propagate. These enter the trap by passing through the window on the top of the trap, which is also used by the imaging system to collect fluorescence.

2.2.1 Cooling beams

To Doppler cool ions we need 397 nm light detuned of order 20 MHz to the blue of the atomic resonance. We want to approximately saturate this transition for two reasons: firstly, so that the cooling rate is high, and secondly because during our readout process we discriminate between qubit states by detection of fluorescence induced by the Doppler cooling lasers (see section 4.2). The higher the scattering rate, the shorter this detection

period can be.

We also use light from this laser for sub-Doppler cooling. This is a continuous Raman cooling process, described in chapter 5. It relies on a two photon transition between the qubit states. Two beams are required (labeled 397 σ and 397pr on figure 2.6), separated in frequency by a few megahertz and detuned from the atomic resonance by 100+ MHz, to either the red or the blue. The pump beam (397 σ) has a higher intensity than the probe (397pr) beam.

Any light from the 397 cooling laser which reaches the ion(s) during the information processing part of an experiment, when this laser is nominally turned off, will cause decoherence of the qubit(s). The intensity and detuning of the 397 beams means that three passes through AOMs are required to reduce decoherence due to 397 scattering to a negligible level.

The following arrangement is used to produce the three beams we require from the 397 cooling laser. After the optical isolator, the laser beam passes through a mirror blank, the front and rear reflections from which are used for the locking and diagnostic beams. A double pass AOM is then used to provide the bulk of the beam extinction. The beam is next reflected off a diffraction grating. This disperses it according to its wavelength, and an iris further down the beam path ensures that any component of the nominally 397 nm beam with a wavelength of 393 nm is prevented from reaching the ion, where it could shelve the ion in the 3D_{5/2} level. This light at 393 nm is produced by amplified spontaneous emission within the laser diode.

A $\lambda/2$ waveplate and polarising beamsplitter cube is then used to split the beam up into the intense pump and weaker probe beams. These two beams each make a single pass through separate 200 MHz AOMs, see figure 2.7. To get the Doppler beam, the zeroth order beam leaving the pump AOM passes through an 85 MHz AOM. As the Doppler and pump beams are never needed to illuminate the ion simultaneously, both are able to use the same, high, proportion of the total beam power. The relative power of the pump and Doppler beams is controlled by changing the amplitude of the RF driving the pump AOM. The AOMs are able to be used to either add or subtract their frequency onto that of the laser light. For the experiments we have performed the Doppler AOM is used in -1st order, *i.e.* it subtracts 85 MHz from the beam. For experiments in continuous cooling on the red side (section 5.3), the pump and probe AOMs were also used in -1st order, resulting in these beams being 115 MHz to the red of the Doppler beam. For blue side continuous cooling ('EIT' cooling) (section 5.4), the pump and probe AOMs are used in +1st order after being turned around (thus not changing the path of the diffracted beam), so that the beams have frequencies 285 MHz to the blue of the Doppler beam.

The 397 probe and Doppler beams are combined on a PBS cube. Thereafter they have perpendicular polarisations. We set the probe beam to have horizontal polarisation and so the Doppler has vertical polarisation. A $\lambda/2$ waveplate in the Doppler beam before this cube can be used to temporarily divert some light from the Doppler beam through the cube. This beam is then sent through a telescope onto a raised platform before being superimposed onto the 423/389 beam path and sent into the vacuum system through the top window. This vertical beam is used for compensation of the ions' vertical micromotion.

2.2.2 Raman beams

The 397 master-slave laser is used to drive Raman transitions between the two qubit states and to couple the ions' internal state to their motion in the trap.

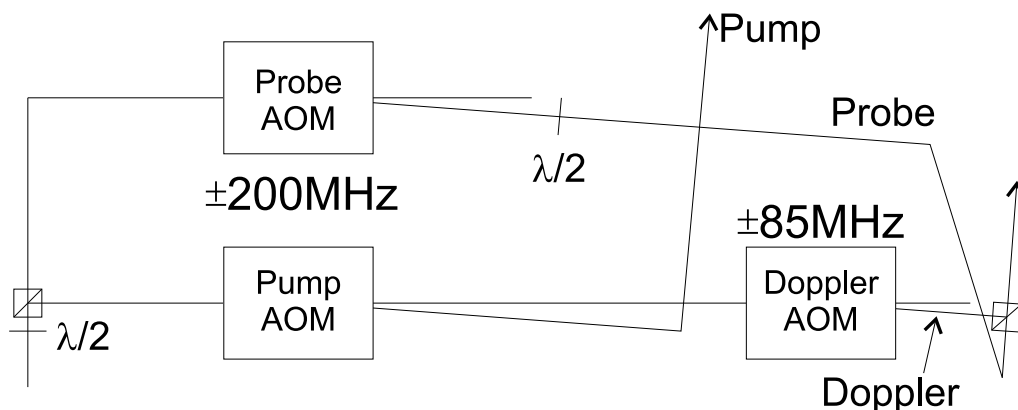


Figure 2.7: Arrangement of single pass AOMs used to produce the three cooling beams. The $\lambda/2$ and pbs are used to split the beam into two parts, the probe beam, and the more intense beam that will produce the pump and Doppler beams. The pump and Doppler beams are never used at the same time. The relative frequencies of the beams can be altered by changing the orientation of the AOMs

The important parameter when driving motional state changing transitions is the Lamb-Dicke parameter. This is equal to $|\Delta\mathbf{k}|z_0 \cos \alpha$, where $\Delta\mathbf{k} = \mathbf{k}_1 - \mathbf{k}_2$ is the difference between the k -vectors of the two lasers driving the transition, α is the angle this vector makes with the normal mode being driven and z_0 is the spatial extent of the ground state wavefunction of the normal mode in question. $z_0 = \sqrt{\hbar/(2m\omega)}$ where m is the mass of the ion crystal in question, and ω the frequency of the normal mode.

The orientation of the two Raman beams is shown in figure 2.6. One beam is approximately parallel to the magnetic field (labelled $397R_{\parallel}$) and the other at 60° to the magnetic field (labelled $397R_{60^\circ}$). The difference k -vector is then (close to) parallel to the trap axis, with the result that the radial motion of the ion(s) does not couple to the Raman beams, only the axial motion.

The light from the 397 master-slave laser is controllably split into the two beams using a waveplate and PBS. These each pass through an AOM. The AOMs serve to impose a frequency difference and to allow fast switching of the beams. This single pass is sufficient, due to the large detuning of the beams.

The 60° beam, after passing through its AOM, is focused by a $f=250$ mm lens, which is positioned 265 mm from trap centre so that the focus of the beam falls on the centre of the trap, where the spot size is $47 \mu\text{m} \times 51 \mu\text{m}$ (as indicated by a CCD camera placed at a position optically equivalent to the trap centre but outside the vacuum chamber). The arrangement for the parallel beam is slightly more complex. The frequency of the switching AOM can be changed, so as to change the detuning of the Raman transition. As this frequency is changed, the deflection angle of the beam as it passes through the AOM also changes. So as to minimise the change in Rabi frequency experienced by the ions as the frequency is changed, the focusing lens of the beam is arranged so that the centre of the AOM is imaged to the centre of the trap. This means that the beam should remain centred on the ion, and the only change in intensity is that caused by change in diffraction efficiency.

The AOM efficiency drops if the focal spot size of the beam is too small - this is because

for a small spot size, if the beam is decomposed into a set of plane waves, a large range of k -vectors is present, only a small proportion of which can meet the Bragg criterion for diffraction in the AOM. Empirically the minimum spot size which gives good diffraction efficiency is approximately $400\ \mu\text{m}$. Since we want a spot size at the ion which is much smaller than this, the lens imaging the AOM onto the trap centre needs to have a high magnification. Because the vacuum system limits how close the final lens can be to the centre of trap, the distance between AOM and lens has to be large. An $f=150\ \text{mm}$ lens is used, located a distance $158\ \text{mm}$ from the ion position and the distance from the AOM to the lens is $3.140\ \text{m}$. This gives a magnification of 0.05 .

The beam leaving the 397 master-slave system is highly elliptical ($\sim 550\ \mu\text{m} \times 2000\ \mu\text{m}$ at $\sim 0.3\ \text{m}$ from the slave laser) with a very non-Gaussian profile in the horizontal direction. A tilted lens telescope is used to reduce the eccentricity of the beam, so that it is $\sim 600\ \mu\text{m} \times 600\ \mu\text{m}$ at the centre of the AOM. The measured spot size at the centre of the trap is $38\ \mu\text{m} \times 19\ \mu\text{m}$. This size is not consistent with the magnification of the focusing lens. This is explained by the action of the AOM on the beam. Looking at the undiffracted and diffracted beams after the AOM, it is seen that the AOM is not removing light from the incident beam in the same proportion across the beam profile, but instead primarily removing intensity from the centre of the incident beam, resulting in the diffracted beam looking more Gaussian than the incident beam.

2.3 Control of the experiment

The experiment is under the control of an IBM compatible PC running MS-DOS, with the control software written in Turbo Pascal by Dr David Lucas. The computer is able to control and measure many aspects of the experiment. These include which lasers are illuminating the ion(s) (by turning on and off the AOMs), the frequencies of the 397 cooling laser (by changing the point on the cavity fringe at which the laser is locked) and of the 393, 866 and 850 lasers (by altering the lengths of the cavities to which they are locked) and the relative frequencies of the 397 probe and pump beams and also of the two 397 Raman beams (by changing the frequency at which the AOMs are driven). The most important measurement that the computer makes is the number of photons detected by the PMT. This is performed using hardware counters that are read by the computer. Details can be found in [32]. Various aspects of this computer control will now be described in more detail.

Pulse sequences

A quantum information experiment requires complex sequences of laser or magnetic resonance pulses. To perform this task a ‘laser control unit’ (LCU) was designed and constructed by Ben Keitch[45]. The hardware of the LCU consists of 16 digital outputs (emitting TTL voltage levels) which are able to drive loads of input impedance of $\geq 50\ \Omega$. These outputs are controlled by 16 digital inputs to the LCU and a gating input. The gating input is under the control of a hardware timing IC which has a timing resolution of $0.2\ \mu\text{s}$, with minimum pulse length $0.2\ \mu\text{s}$ and maximum of $13.1\ \text{ms}$. Between these timed pulses there is a ‘dead time’ of $12\ \mu\text{s}$, where all the digital outs are off. The digital inputs to the LCU work on the convention that 1 is on, 0 is off. Each of the channels is also invertible so that if the device under control is turned on by a low voltage, the input convention is maintained. In addition, each of the output channels can be overridden by

a mechanical switch and turned permanently on or off. The control software allows long pulse sequences to be easily composed and run.

Frequency control

We have two pairs of laser beams used to drive Raman transitions between the qubit states. The 397 probe and 397 pump beams are one pair, used for cooling experiments. The parallel and 60° 397 Raman beams are the other pair. This pair can be used for many different purposes, such as temperature diagnostics, cooling and driving quantum gates.

To drive Raman transitions the frequency difference between the beams in the pair needs to be controlled. This is done using AOMs to add or subtract known frequencies from each beam, see above. For the 397 probe and pump beams, the AOMs are driven by driver boxes supplied by IntraAction. Each box can produce up to ~ 2 W at frequencies around 200 MHz. The pump beam AOM is operated at 200 MHz, while the frequency of the probe is under computer control via a frequency modulation input. The input has an input impedance of 50Ω . This modulation input is driven by one of the digital to analogue converters (DACs) in the experimental computer. These are only able to source a low current and so a unity gain amplifier¹, which is able to drive 50Ω loads, is used as a buffer. With nothing connected to the FM modulation the output frequency of the driver jittered with a range of ~ 5 kHz. With a modulation voltage applied by the computer the output frequency of the driver had a jitter ~ 100 kHz, caused by noise on the DAC output. A low pass filter connected between the buffer and FM input reduced the jitter to ~ 10 kHz.

The AOMs for the Raman beams use as their frequency source Agilent synthesizers (models E4422B and E4426B). To ensure maximum frequency stability the synths are daisy-chained, the 10 MHz reference out of one synth being used to supply the external 10 MHz input of the next. Each synth's output is turned off and on by applying 0 or 1 V to one of the modulation inputs of the synthesiser, which is set to pulse modulation. The minimum output pulse length the synth can produce when in pulse modulation mode is $0.4 \mu\text{s}$.

The synth for the 60° beam's AOM is set to produce 200 MHz and its output goes to an amplifier and then the AOM. There are up to four synths which can be set to drive the parallel beam AOM, allowing up to four different Raman detunings to be used within an experimental sequence. All four synths are turned on and off from a single computer digital output (via the LCU), and the RF outputs of the synths pass through a switching network controlled by a further two digital outputs which select which RF source drives the parallel beam amplifier, see figure 2.8. The switches are Minicircuits ZASWA-2-50DR. The insertion loss of each switch is 1.7 dB, and the isolation 90 dB. The frequency of one of the parallel beam synthesizers is controlled by one of the DAC outputs of the computer, which is connected to a modulation input of the synth via the buffer amplifier. This allows the frequency of this synthesizer to be changed from sequence to sequence, *e.g.* so that the computer can perform a scan over the Raman spectrum of the ion(s).

Each amplifier is a Motorola 2810C mounted on a heatsink and fan cooled. They have a gain of 34.7 dB, and the 1 dB compression point occurs for an output of 31 dBm. The maximum diffraction efficiency of the AOMs should occur for an RF power of ~ 2.5 W which is greater than the amplifier can supply. The spot size of the beams and the power supplied by the 397 master-slave however mean that the intensity of light at the ion is sufficient

¹Maxim Integrated Products MAX496 quad video buffer

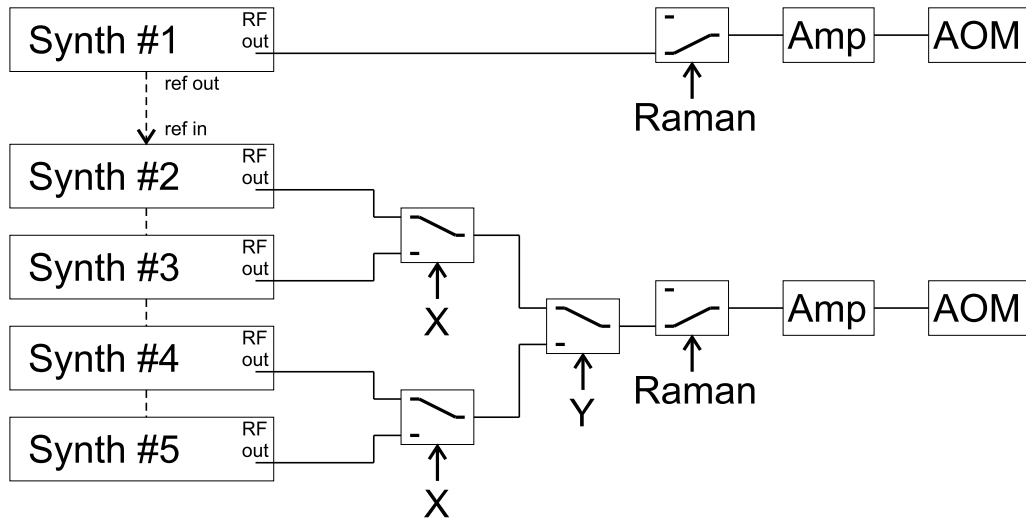


Figure 2.8: Synth network for driving Raman beam AOMs. Five synths can be used to provide up to four different Raman detunings during a single experimental sequence. Synth 1 drives the 60° Raman beam and two digital outputs X and Y allow the computer to switch between synths 2–5 to drive the parallel beam. A third digital out is used to turn the Raman beams on or off. The synths used are Agilent E4422B and E4426B, the switches Minicircuits ZASWA-2-50DR and the amplifiers Motorola 2810C, details of which are given in the text.

for our purposes with the amplifiers we currently have supplying less than their maximum power.

Chapter 3

Photoionization

The standard method to load ions into an ion trap is to pass a beam of neutral atoms through the trapping region, and ionize the atoms in situ by means of electron bombardment. Electron bombardment has various shortcomings however. Owing to their acceleration by the large a.c. fields of the trap, the incident electron energies are uncontrolled. This method ionizes all isotopes present in the atomic beam equally, and also ionizes any other species in the background gas in the vacuum chamber. This makes it impractical for the loading of any but the most abundant isotope ($^{40}\text{Ca}^+$) and also time-consuming, in that usually several ions are loaded, not always of the desired species/isotope, and a slow process to eject unwanted ions has to be performed.

In addition, the electron beam charges insulating regions of the ion trap electrode structure. This requires the compensation voltages (see 2.1.2) to be changed after each load, and also results in a slow drift of the electric field at the ion as the charge leaks away ([39, 32], also appendix A sec.VI). Typically, the electric field is not stable until about 24 hours after loading the trap (appendix A figure 11(a)). Furthermore, the stray field changes by up to 200V/m on longer time scales (appendix A figure 11(b)).

Photoionization allows the loading of $^{40}\text{Ca}^+$ in a much more controlled fashion and without charging the electrodes. Additionally, the isotope shifts in the neutral atoms mean that the ionization process can be isotope-specific, making it possible to load selectively any desired isotope. We have implemented a photoionisation system and used it to load all the stable isotopes of calcium selectively into our trap. A paper covering in some detail the observations and the experiments to characterise the system is included as appendix A. This chapter provides some supplementary information.

3.1 Geometric factor

Neutral calcium atoms are excited by incident radiation at 423 nm. We use an absolute measurement of the fluorescence rate to deduce the number density of atoms in the beam. This information is useful both in order to deduce the loading efficiency and to allow the photoionisation cross-section to be extracted.

When the atomic calcium beam is driven by the linearly polarised 423 nm laser, the radiation is emitted with a dipole distribution and thus the detected fluorescence depends on the angle this dipole makes with the imaging optics, as well as the collection angle of the imaging optics. To calculate the number density in the beam requires us to take into account this directionality of radiation emission. The number density is calculated

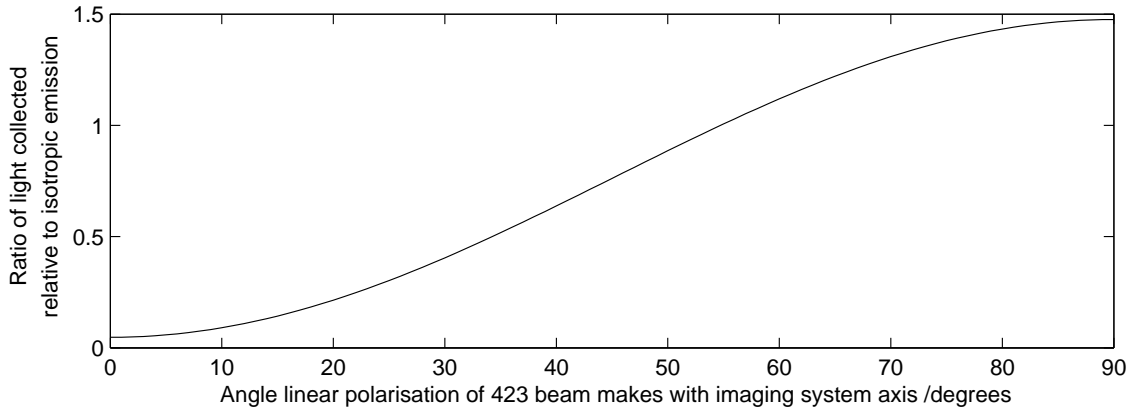


Figure 3.1: Geometric factor for light collection from the fluorescing atomic beam for the geometry of exciting 423 beam and imaging system as a function of the angle the linear polarisation of the 423 beam makes with the vertical. This is expressed as the ratio of fluorescence expected relative to that emitted by an isotropic emitter.

in section III.C of the paper and this directionality is accounted for by a geometric factor $r = 1.43$. This geometric factor is the ratio of the expected fluorescence for our imaging system position to that we would obtain for isotropic emission. Its calculation is as follows.

The dipole emission pattern goes as the square of the sine of the angle the emission direction makes with the dipole. The fraction of radiation collected is therefore equal to

$$\frac{3}{8\pi} \iint_{\text{IS}} \sin^3(\theta) d\theta d\phi \quad (3.1)$$

where the integration is taken over the solid angle collected by the imaging system and the dipole lies at angle $\theta = 0$.

The geometry of the 423 beam and imaging system are described here. The 423 beam makes an angle of 26.9° to the vertical, which is the direction of the collection optics for the imaging system. The imaging system acceptance half angle is 14.5° . To calculate the geometric factor the integral in equation 3.1 was numerically integrated over the part of the dipole seen by the imaging system for the full range of possible polarisations the 423 beam could have. The result of these integrations is shown in figure 3.1. The angle that the 423 polarisation made with the vertical was $80(2)^\circ$ for the number density experiment giving the quoted geometric factor of $1.43(2)$.

3.2 Photoionization cross section

One item of information we were able to extract from our observations was a lower limit for the absolute cross section for photoionization of calcium I from the $4s4p$ excited state. The observed value was 170 ± 60 Mbarns ($1 \text{ Mbarn} = 10^{-22} \text{ m}^2$), which is high in comparison to the value one would expect from a crude estimate of ionizing a hydrogen-like system. The hydrogenic case is analysed by Cowan [46, §18-6] and gives the absolute cross-section

$$Q(\epsilon) = \frac{64\pi\alpha a_0^2 n}{3\sqrt{3}} \left(\frac{\epsilon_n}{\epsilon}\right)^3 \quad (3.2)$$

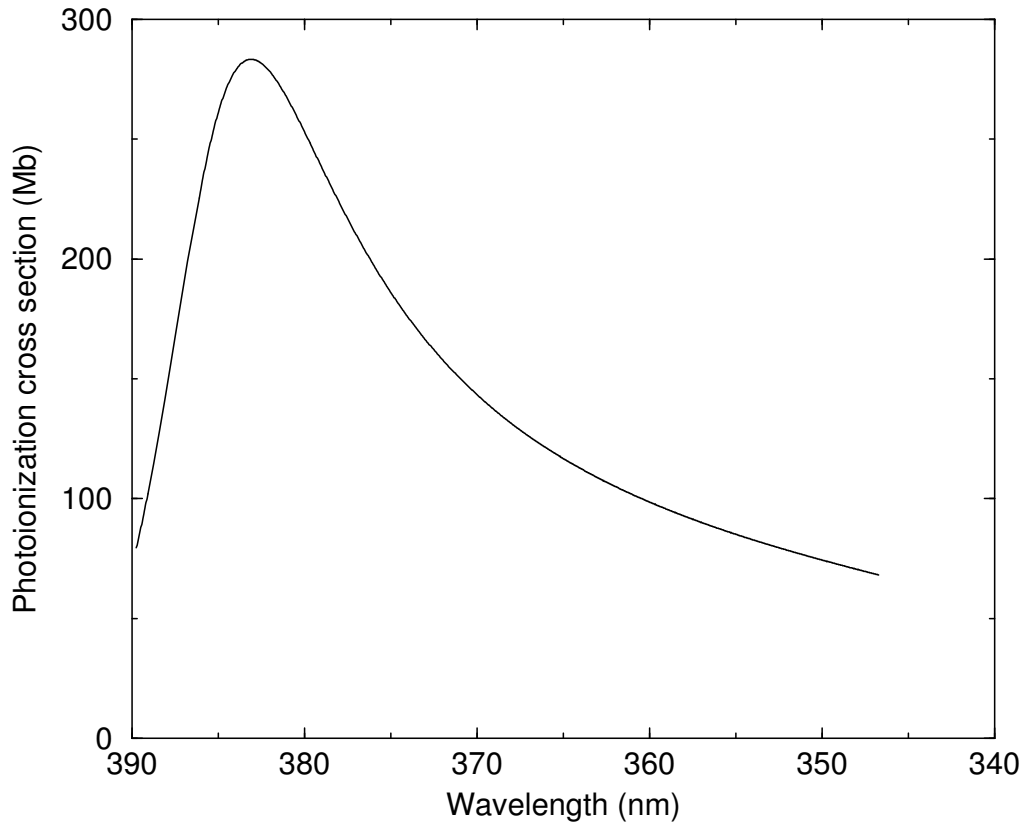


Figure 3.2: Cross section for excitation from the 1P_1 level in calcium, calculated by McKenna and van der Hart [47]. The cross-section is enhanced due to the presence of an auto-ionizing resonance near the ionization threshold, the position of which is uncertain to ± 5 nm.

where ϵ is the energy of the incident photon, ϵ_n is the ionization energy for ionization from the shell of principal quantum number n , α is the fine-structure constant and a_0 the first Bohr radius. For the $4s4p \ ^1P_1$ level in calcium, $\epsilon_4 = 3.18 \text{ eV} = 0.234$ rydbergs. Equation 3.2 assumes that $\epsilon_n = 1/n^2$ rydbergs which is clearly not appropriate here; if instead we use an effective quantum number $n^* = 2.07$ then we find, at the continuum limit, $Q(\epsilon) = 16 \times 10^{-22} \text{ m}^2 = 16$ Mbarn.

The reason that the hydrogenic case is such a poor approximation to the calcium system is the existence of doubly-excited auto-ionizing resonances in the continuum. Such doubly-excited states are extremely short-lived, giving features several nm wide, but considerably enhance the cross-section. A calculation of the cross-section taking into account an auto-ionizing resonance in the vicinity of the ionization threshold was performed by McKenna and van der Hart [47]; the result is shown in figure 3.2. The position of the resonance is uncertain to ± 5 nm, but the calculation shows that the cross-section may be as large as 280 Mb, and the lower limit we deduce from ion trap loading rates is entirely plausible. The calculation also shows that it would be interesting to study the variation of the cross-section with wavelength, to choose the optimum wavelength for the 389 nm laser.

Chapter 4

Single qubit Rabi flopping experiments

We use the $^{40}\text{Ca}^+$ ion in all the cooling and quantum information experiments described in this thesis. The low-lying energy levels of the ion are shown in figure 4.1. The two magnetic sublevels of the $4\text{S}_{1/2}$ ground state are split with a magnetic field, such that the splitting between them is $\sim 4\text{MHz}$. These two states are used for our two logical qubit states. We use the notation $|\uparrow\rangle, |\downarrow\rangle$ to refer to the $4\text{S}_{1/2} m_j = 1/2$ and $m_j = -1/2$ states respectively.

A typical experimental sequence consists of 5 steps: cooling, spin-state initialization, coherent evolution, selective shelving and finally fluorescence detection. Section 4.1 discusses fluorescence detection, Doppler cooling and spin-state preparation. In section 4.2 we discuss a method to selectively transfer population from one (and only one) of our qubit states $|\uparrow\rangle, |\downarrow\rangle$ to the metastable ‘shelf’ level $3\text{D}_{5/2}$. This is the heart of our method to measure the qubit: if the ion has been shelved it does not fluoresce in the final part of the sequence, allowing us to infer the spin state from the presence or absence of radiation.

The remaining sections are devoted to coherent evolution of the ion. We have two methods to drive coherent evolution of our qubit: magnetic resonance, and Raman transitions. Section 4.3 discusses the theory of magnetic resonance and the coherent population transfer that occurs when a two level system is driven by a periodic interaction. This section also describes basic concepts such as a phase gate, the Ramsey separated oscillatory fields method, and the spin-echo.

We then consider the use of the magnetic resonance in our experiments. We start by describing how we locate the qubit resonance frequency, first using a Raman process to locate it roughly, then using the magnetic resonance. We present Rabi flopping signals and discuss the problems of fluctuations and drifts of the magnetic field experienced by the ion.

In section 4.5 we discuss the use of Raman transitions for coherent driving of the ion. We give some basic theoretical results and discuss treating the ion as an effective two level system, induced light shifts and coupling to the ion’s harmonic motion.

We describe experiments in which we use the Raman beams individually to produce a phase gate on the qubit, which we detect using magnetic resonance. This allows us to infer the strength of the coupling of the laser to the ion accurately. Finally, we give an example of a Raman spectrum obtained with an ion cooled to $\sim \text{mK}$ temperature near the Doppler limit, showing the quantised ionic motion. Further cooling and manipulation of

the motional state is the subject of chapter 5.

4.1 Fluorescence, Doppler cooling and qubit initialization

The ion is Doppler cooled on the $4S_{1/2} \leftrightarrow 4P_{1/2}$ 397 nm transition. For the most efficient cooling for a given laser power, the 397 Doppler laser is detuned to the half fluorescence point of the atomic resonance. To prevent the ion becoming trapped in the metastable $3D_{3/2}$ level, the 866 laser is also turned on during any Doppler cooling, to act as a repumper. The 866 laser is normally detuned slightly to the blue of its transition, so as to avoid the possibility of the two lasers being in Raman resonance, causing dark resonances. The $4S_{1/2}$, $4P_{1/2}$ and $3D_{3/2}$ levels form a closed system under the application of the two Doppler cooling lasers, scattering millions of photons per second. By contrast, if the ion is in the metastable $3D_{5/2}$ ‘shelf’ level, then no photons are scattered from the cooling lasers by the ion. This allows us to determine if the ion is in the shelf with high accuracy by counting photons for ~ 1 ms. State discrimination performed with this method is called electron shelving[15, 16, 17], and is used to determine the state of the ionic qubit, in the method described in section 4.2.

The ion can be easily prepared in either one of its qubit states by applying the 397 pump and 866 lasers. Since the 397 pump beam is σ polarised the ion will be optically pumped into one of $|\uparrow\rangle$ or $|\downarrow\rangle$.

4.2 Qubit Readout

The procedure for performing a measurement of the quantum state will now be summarised; full details can be found in the thesis of Matthew McDonnell[30]. Figure 4.2 shows the energy levels and transitions relevant to the readout method. The method takes advantage of the electron shelving technique mentioned above. First the population of one of the qubit states is transferred to the $3D_{5/2}$ shelf while the population in the other qubit state is left in the ground state. By then applying the Doppler cooling beams to the ion and counting photons to determine if the ion is in the shelf, the original qubit state can be determined. Which of the qubit states is shelved depends on the polarisations of the two lasers we use in the shelving process. The description of the method below has the polarisations set to produce shelving of the $|\uparrow\rangle$ state.

Applying weak, on resonance σ^+ polarized 393 nm light to an ion will cause an ion in the $|\uparrow\rangle$ state to be excited to $4P_{3/2}$, $m_j = 3/2$. From there, 94% of the time it will decay to $4S_{1/2}$, and due to angular momentum conservation, these decays always return it to the initial $|\uparrow\rangle$ state. The other 6% of the time, it will decay to one of the metastable 3D levels. Of these decays 89% take the ion to the shelf, as required, the other 11% going to the $3D_{3/2}$ level. The longer the transition is driven for, the greater the probability the ion ends up in the shelf, up to a maximum probability of 89%. The 393 laser, however, also affects the $|\downarrow\rangle$ state, exciting it to $4P_{3/2}$, $m_j = 1/2$ from where it can decay to the shelf, or, much more likely, be optically pumping into the $|\uparrow\rangle$ state. This means that the 393 laser by itself does not produce the required selective shelving.

To introduce selectivity we apply intense σ^- polarised 850 nm light to the ion. Due to the angular momentum selection rules this has no effect on excitation from $|\uparrow\rangle$ because the $4P_{3/2}$, $m_j = 3/2$ upper state does not couple to this 850 nm light. It does however couple the $4P_{3/2}$, $m_j = 1/2$ sublevel to one of the $3D_{3/2}$ sublevels, and so $|\downarrow\rangle$, $4P_{3/2}$, $m_j = 1/2$

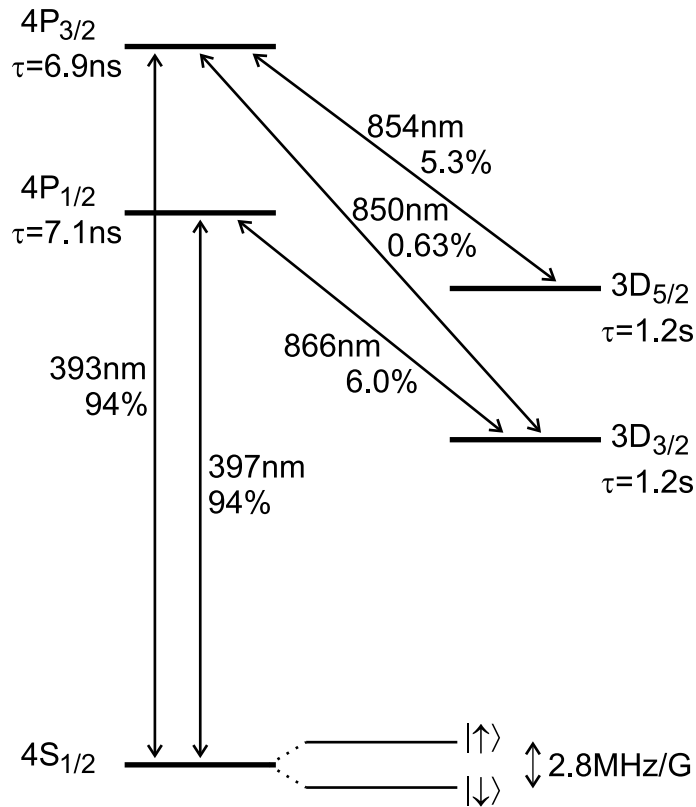


Figure 4.1: Energy level diagram showing the low lying levels of the $^{40}\text{Ca}^+$ ion. Indicated are the wavelengths of the dipole allowed transitions, the lifetime of the excited and metastable states, and the branching ratios for decay from the unstable P states. Also shown is the magnetic field-induced splitting of the $S_{1/2}$ ground state which is used for our qubit.

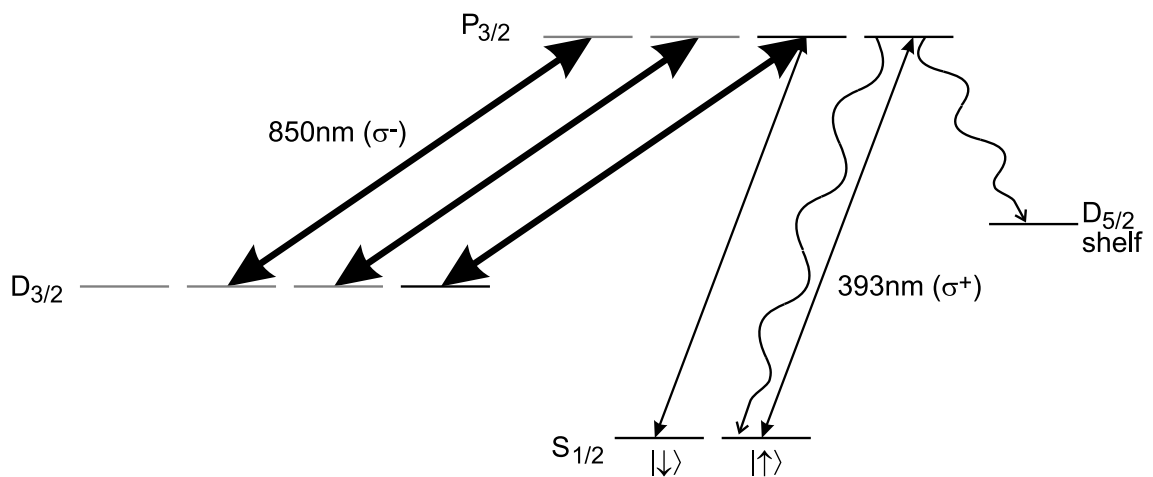


Figure 4.2: Electron shelving using EIT. The 850 nm laser creates a null in the absorption spectrum of 393 nm light from the $|\downarrow\rangle$ state, suppressing absorption. The $|\uparrow\rangle$ state is excited as normal as its destination upper state is uncoupled to the 850 nm laser.

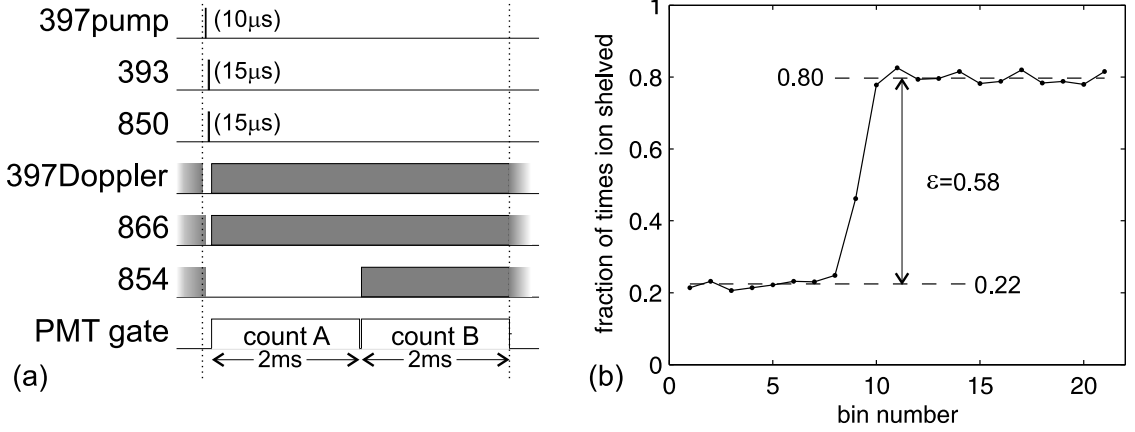


Figure 4.3: (a): Sequence used for measuring shelving efficiency. The length of the 393/850 pulse varies, because the ‘best’ length depends on the power in the 393 beam, which can change from day to day. The PMT is gated twice, once to determine if the ion has been shelved, and a second time to check that the ion is still present and cold. This second period also Doppler cools the ion. (b): Example data. Each of the bins shows the result of 500 successful repeats of the experimental sequence. During the 9th bin, the polarisation of the 397 pump beam was changed from σ^+ to σ^- . The probability of shelving the $|\downarrow\rangle$ state is 0.22, the $|\uparrow\rangle$ state 0.80, giving an efficiency of 0.58. Dashed lines indicate these “shelving levels” on this, and subsequent plots.

and $3D_{3/2}$, $m_j = 3/2$ form a three level system, see figure 4.2. If the 850 laser is resonant with its transition then it effectively splits the upper level into two dressed states, spaced in energy about the position of the unperturbed upper level. 393 nm light resonant with the unperturbed transition will have its excitation probability greatly reduced as the two excitation paths (to the two dressed states) destructively interfere. This process is known as electromagnetically induced transparency, as the intense beam causes the ionic system to become transparent to the weak 393 laser. The degree of transparency increases with increased 850 laser power and decreased linewidth of the two lasers[31, 48].

After the shelving has been performed, the final part of the readout process is to detect whether the ion is in the shelf level or not. This, as has already been stated, is done by turning on the Doppler cooling lasers and counting the number of photons detected by the PMT. By comparing this number with a previously determined threshold, the ion can be said to have been shelved or not. This threshold is determined from the mean number of photons counted during a detection period under two different conditions. The first of these is with both the 397 Doppler and 866 lasers on; this determines the number of photons scattered by a non-shelved ion. The second is with only the 397 Doppler beam on: this determines the number of counts from stray light. The number of photons detected during a single measurement period follows a Poissonian probability distribution and the most efficient threshold to distinguish a shelved ion from a non-shelved one can be calculated from the two measured mean counts.

Figure 4.3a shows the experimental sequence used to measure the probability the ion is detected as being shelved for the two different initial states. This sequence forms the basis of most of the experiments presented in this thesis. Each sequence starts with the ion already in a Doppler cooled state, after the previous sequence. Firstly, the ion is optically

pumped into one of the qubit states by using light from the σ polarised 397 pump beam. After this, the two shelving lasers, 393 and 850, are pulsed on. The length of these pulses depends on the 393 laser power and a typical value is $15 \mu\text{s}$. Finally, there are two detection periods. The first, with the 397 Doppler and 866 on, is used to determine if the ion was shelved or not by comparison of the number of PMT counts with the threshold as just described. The second detection phase is then performed with the deshelling 854 laser on in addition to the cooling beams. This serves two purposes. Firstly, it serves to check that the reason for the absence of fluorescence (if that was the case) in the first phase was due to shelving rather than some other cause. For instance, the ion may have been excited by a collision into a high orbit which gives low fluorescence, or one of the cooling lasers might have an incorrect frequency. Secondly, it serves to provide Doppler cooling of the ion, before the next repeat of the experimental sequence.

Figure 4.3b shows the result of performing many shelving experiments on a single ion, for two different initially prepared states. Each bin is the result of 500 successful sequences (*i.e.* those sequences where the second detection phase detected the ion's presence). Let $p_{s|\uparrow}$ be the probability that the ion is detected as being shelved after it has been prepared in the $|\uparrow\rangle$ state and let $p_{s|\downarrow}$ be the probability the ion is detected as being shelved after being prepared in the $|\downarrow\rangle$ state. We define the efficiency ϵ of the shelving process by $\epsilon = p_{s|\uparrow} - p_{s|\downarrow}$. For the example shown in the figure, $p_{s|\uparrow} = 0.80$ and $p_{s|\downarrow} = 0.22$, resulting in a shelving efficiency of $\epsilon = 0.58$. The fact that the efficiency is not close to 1 limits what sort of quantum information experiments are possible. For instance, to perform teleportation experiments, single qubit gate operations must be made, with the gate to be performed dependent on the result of measurement. Fidelity of the teleportation then depends on the fidelity of the measurement. However for determining a quantum state, where multiple copies of the state to be determined can be produced, any non-zero ϵ allows tomography to take place. The probability the ion is shelved $p_s = p_{s|\uparrow}p_\uparrow + p_{s|\downarrow}p_\downarrow$ and similarly for p_{ns} . These relationships are easily inverted to give $p_\uparrow = (p_s - p_{s|\downarrow})/\epsilon$.

The state which is shelved can be changed by reversing the polarisation of the two σ polarised shelving beams. Unless otherwise stated, all experiments using the readout method will have the shelving laser polarisations set so that the state we initialise into is the state which is not shelved, and for convenience, we call this initialised state $|0\rangle$ and the other state $|1\rangle$.

4.3 Basic concepts in magnetic resonance

We have two methods which we use to manipulate the qubit state in a coherent manner: magnetic resonance, and Raman transitions. This section describes the case of using an oscillating magnetic field to manipulate the spin state. It also discusses using such a coherent evolution to measure phase shifts induced in the qubit through the use of the Ramsey split pulse method and the use of 'spin echo' pulses to improve the robustness of the experiment to errors in the frequency of the driving radiation.

4.3.1 Rabi flopping

The Hamiltonian describing the ground state of $^{40}\text{Ca}^+$ in a magnetic field is $\hat{H} = -\hat{\boldsymbol{\mu}} \cdot \mathbf{B}$ where $\hat{\boldsymbol{\mu}}$ is the magnetic moment of the state, equal to $-g_s\mu_B\mathbf{s}/\hbar$. A constant magnetic field defines the z -axis of our system, and lifts the degeneracy of the two qubit states, giving us a Hamiltonian $H_0 = (1/2)\hbar\omega_s\sigma_z$, where $\hbar\omega_s = g_s\mu_B B$ is the energy splitting of the two

qubit states. If an oscillating magnetic field is applied to the ion, $\mathbf{B}' = B_0 \hat{\mathbf{i}} \cos(\omega t - \phi)$ where B_0, ω are the magnitude and frequency of the field, and ϕ the phase, the interaction Hamiltonian is $H_I = \mu_B B_0 (\sigma^+ + \sigma^-) \cos(\omega t - \phi)$. The complete Hamiltonian is $H = H_0 + H_I$.

Moving into an interaction picture $H \rightarrow H'_I = U_0^\dagger H_I U_0$ where $U_0 = e^{-iH_0 t/\hbar}$ and making the rotating wave approximation, we get the interaction Hamiltonian:

$$H'_I = \frac{\mu_B B_0}{2} (e^{-i\delta t} e^{i\phi} \sigma^+ + e^{i\delta t} e^{-i\phi} \sigma^-) = \frac{\hbar \Omega}{2} (e^{-i\delta t} e^{i\phi} \sigma^+ + e^{i\delta t} e^{-i\phi} \sigma^-) \quad (4.1)$$

where the detuning $\delta = \omega - \omega_s$ and Rabi frequency $\Omega = \mu_B B_0/\hbar$. When $\delta = 0$ this Hamiltonian results in the qubit oscillating between the two basis states with frequency Ω . If the laser is off resonant, a smaller amplitude (equal to $\Omega^2/(\Omega^2 + \delta^2)$) oscillation takes place at a higher frequency (equal to $\sqrt{\Omega^2 + \delta^2}$).

Evolution of the general state $|\Psi\rangle = a|\uparrow\rangle + b|\downarrow\rangle$ under this Hamiltonian can be written in matrix form as

$$\begin{pmatrix} a(t) \\ b(t) \end{pmatrix} = U(t, \alpha, \delta, \phi) \begin{pmatrix} a(0) \\ b(0) \end{pmatrix} \quad (4.2)$$

where t is the length of time the Hamiltonian is applied for, $\alpha = \sqrt{\Omega^2 + \delta^2}$ and

$$U(t, \alpha, \delta, \phi) = \begin{pmatrix} e^{-i\delta t/2} (\cos(\alpha t/2) + i \frac{\delta}{\alpha} \sin(\alpha t/2)) & -i \frac{\Omega}{\alpha} e^{i(\phi - \delta t/2)} \sin(\alpha t/2) \\ -i \frac{\Omega}{\alpha} e^{-i(\phi - \delta t/2)} \sin(\alpha t/2) & e^{i\delta t/2} (\cos(\alpha t/2) - i \frac{\delta}{\alpha} \sin(\alpha t/2)) \end{pmatrix}. \quad (4.3)$$

For a detuning equal to zero this simplifies to

$$U(t, \Omega, \phi) = \begin{pmatrix} \cos(\Omega t/2) & -i e^{i\phi} \sin(\Omega t/2) \\ -i e^{-i\phi} \sin(\Omega t/2) & \cos(\Omega t/2) \end{pmatrix}. \quad (4.4)$$

If we look at the Bloch sphere picture of the two level system, this corresponds to a rotation of angle Ωt about an axis lying in the x - y plane, at an angle ϕ to the x -axis. Any single qubit gate can be expressed as a sequence of these pulses.

4.3.2 Ramsey and Spin echo

The effect of gates or other physical processes that affect only the phase of the qubit(s) involved cannot be directly measured by preparing an ion by optical pumping, performing the gate, and then performing a readout. To create a state which is sensitive to phase changes, we start with the ion initialised in the $|0\rangle$ state, and apply a $\pi/2$ pulse to create the superposition state $\frac{1}{\sqrt{2}}(|0\rangle + |1\rangle)$. We can then apply the phase changing operation. To then map the phase change onto the qubit population we perform another $\pi/2$ rotation. If the $|0\rangle$ state acquires a phase of ϕ_0 and the $|1\rangle$ state a phase of ϕ_1 then the probability of measuring the qubit as being in $|0\rangle$ is $\frac{1}{2}(1 - \cos(\phi_g))$ where $\phi_g = \phi_1 - \phi_0$. Note that this does not allow us to determine the sign of ϕ_g . If the phase of the second $\pi/2$ pulse were different from the first, then this could be determined, however for many experiments the sign of the phase change is either known, or unimportant, so changing the phase of the second pulse is unnecessary.

This use of two time-separated $\pi/2$ excitation pulses is often referred to as a Ramsey sequence. This sequence of two $\pi/2$ pulses is used in atomic clocks because it produces the narrowest linewidth signal for a given total interaction time, giving a fringe pattern of alternate high and low probability of being in the $|1\rangle$ state as the frequency of the driving

radiation is scanned, with fringe width $\sim \pi/\tau$ where τ is the time separation between the pulses. This means that a Ramsey pulse sequence is very sensitive to the detuning of the driving radiation, the sensitivity increasing as the time between pulses increases.

To reduce this sensitivity ‘spin echo’ pulses are widely used[3, 4]. As before, the sequence starts with a $\pi/2$ pulse, then the phase changing process we wish to measure is turned on. Next, a π pulse is applied to the system. After waiting for a time equal to the gap between the first two pulses, a further $\pi/2$ pulse is applied. The use of a spin echo pulse doubles the time length of the coherent evolution section of the pulse sequence. The effect of the driving potential being detuned from resonance is to cause the driving radiation phase to advance relative to that of the qubit at a rate equal to the detuning. During the gap between the first two pulses, a phase of $-\delta \cdot \tau$ plus a phase ϕ_g , from any other phase changing process such as a phase gate, will be added to the qubit, so it has a phase, relative to that defined by the radiation, of $-\delta\tau + \phi_g$. The π pulse swaps the two qubit basis states, so now the qubit has a phase equal to $\delta\tau - \phi_g$ relative to the radiation. The free evolution between the pulses again adds a phase $-\delta\tau$, leaving the qubit with a phase $-\phi_g$ ready to be acted upon by the final $\pi/2$ pulse. After a Ramsey-spin echo sequence, the probability of observing the qubit in $|0\rangle$ is $\frac{1}{2}(1 + \cos \phi_g)$.

Figure 4.4 shows the pulse sequences for Ramsey and Ramsey-spin echo experiments, as well as plots illustrating the robustness of spin echo compared with Ramsey pulses. These theoretical plots do not take into account any qubit decoherence, and also assume a constant detuning over the duration of the pulse sequence. This is only true if the duration of this part of the sequence is small compared to the 20 ms period of the 50 Hz mains (see the next section). The spin echo is valuable in our case mainly because it makes the experiment less sensitive to slow drifts of the magnetic field on the ion.

4.4 Magnetic resonance experiments

The coil for driving the magnetic resonance was described in section 2.1.4.

4.4.1 Determining the qubit splitting

Our first task was to use the coil to measure the Larmor frequency ω_s . Since the width of the magnetic resonance is small compared to the resonance frequency, to find ω_s by exhaustive search would take a large time, and so an approximate measurement of the Zeeman splitting is useful to narrow the search area. The magnetic field experienced by the ion had previously been measured as a function of the currents passing through the coils used to generate the static field[32]. However a large amount of hysteresis exists in the system, thought to be caused by magnetisable material used in the construction of the vacuum can, so that the field at the ion could not be predicted accurately merely by reference to the currents flowing through the three pairs of coils which produce the field. The field was originally calibrated through the use of 397/866 nm dark resonances, but at the low field we currently use, the individual components of the dark resonances are separated by less than their width, making them unresolvable.

A narrower resonance is available to determine the qubit splitting - the Raman resonance used for cooling, and described in the next chapter. The width of this resonance is a function of laser parameters, and is in the range of 0.1 to 1 MHz (see figure 5.4 of chapter 5). It is caused by a Raman transition between $|\uparrow\rangle$ and $|\downarrow\rangle$, driven by the 397 pump and probe beams detuned by ~ 150 MHz from the single photon transition. The pump beam is

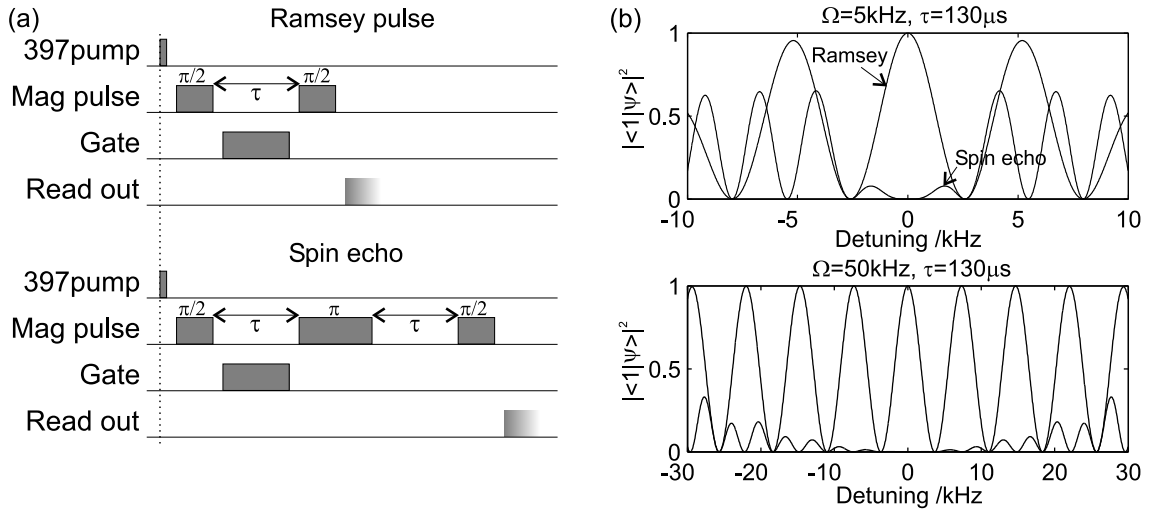


Figure 4.4: Ramsey and Ramsey-spin echo methods. (a) Pulse sequences for a Ramsey, and a Ramsey-spin echo experiment. By using two $\pi/2$ pulses, changes in qubit phase can be measured. In this Ramsey type pulse sequence however the phase measured also contains contributions due to driving the qubit off-resonantly. By adding a π pulse, the contribution due to detuning error is removed in the second half of the sequence. (b) Plots of population as a function of detuning for Ramsey and Ramsey-spin echo, for two different Rabi frequencies. Adding the spin echo pulse is most effective in countering detuning errors when $\Omega \gg 1/\tau$.

σ polarised, the weak probe beam π . As the π beam is scanned in frequency a resonance in the fluorescence emitted by the ion is seen.

If the resonance were occurring precisely at the Larmor frequency ω_s , then we could deduce ω_s from the frequency difference between the pump and probe beams, which is set by two AOM's and is known to within ± 1 kHz. However, the resonance is displaced by a light shift Δ' caused by the pump beam (the other beam is π polarised and much weaker; for both reasons it does not shift the resonance). If the pump beam polarisation is set to σ^+ , the shift acts on $|\downarrow\rangle$, so the resonance frequency is $\omega_s + \Delta'$. If the polarisation is σ^- , the shift acts on $|\uparrow\rangle$ so the resonance frequency is $\omega_s - \Delta'$. By observing the resonance under each condition, we can deduce both ω_s and Δ' .

This method to find ω_s was used several times whilst changing the magnetic field. The field was adjusted both in order to get it parallel to the 850 beam (we test this using optical pumping) and in order to set its magnitude to produce a Larmor frequency around 4 MHz to match our magnetic resonance coil. Once the splitting was thus roughly determined, a much more precise value could be obtained from magnetic resonance.

Figure 4.5a shows the result of using the magnetic resonance to find the Zeeman splitting more accurately. Each point on the graph is the result of 1000 repeats of a sequence similar to that in figure 4.3a, except that between the preparation and readout pulses the oscillating magnetic field was turned on for a period of $100\mu\text{s}$. The figure shows the fraction of times the ion is shelved as a function of the frequency of the oscillating field. A resonance can be seen where the oscillating field is causing population transfer between the two levels, centred at a frequency of around 4374 kHz. The dashed lines on the graph indicate the measured values of p_\uparrow and p_\downarrow .

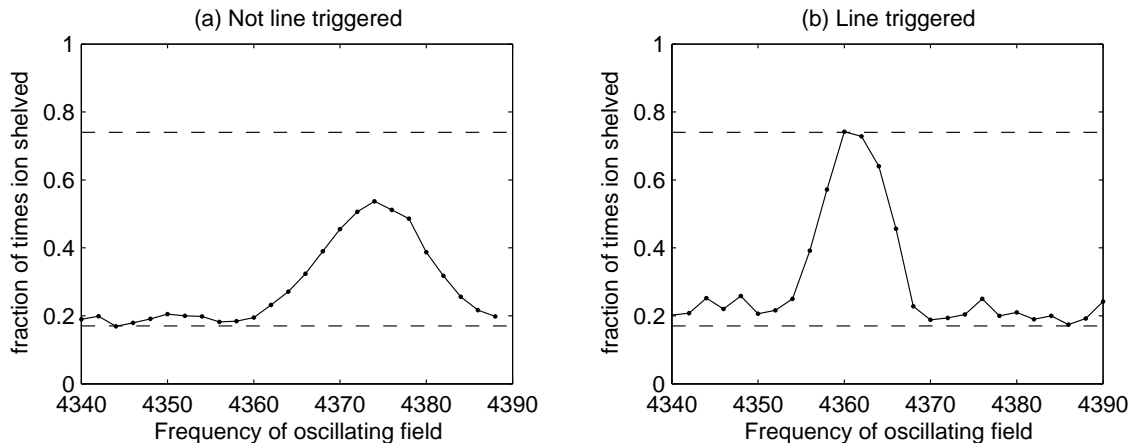


Figure 4.5: Two examples of magnetic resonance frequency scans. A magnetic pulse time of $100 \mu\text{s}$ was used in both scans (approximately the time required for population inversion). (a) Each point 1000 experimental sequences of prepare-magnetic pulse-readout. Centre of the resonance is 4374 kHz, and $\sim 60\%$ population transfer from $|0\rangle$ to $|1\rangle$ is achieved. (b) Each point 500 experimental sequences. The start of each sequence was triggered at the same phase of the 50 Hz mains frequency each time the sequence was performed. The resonance is at a frequency of 4360 kHz and $\sim 100\%$ population transfer occurs at the centre of the resonance.

By setting the frequency to the centre of the resonance and measuring the population in the $|1\rangle$ state as a function of the duration of the magnetic pulse, oscillation between the two qubit states can be seen. It was not possible to obtain complete population inversion because the amplitude of the oscillation in the population died away in a $1/e$ time of $\sim 250 \mu\text{s}$. The reason for this decay of contrast is that the resonance frequency ω_s is not the same from sequence to sequence. Another consequence of this is that the 15 MHz width of the resonance shown in figure 4.5a is greater than one would expect. For a frequency scan where the pulse time is picked to be equivalent to a π pulse when the detuning is zero, the resonance should have a $\text{FWHM} \simeq 1.6\Omega$, which is much less than the width observed. The variation of resonance frequency is due to magnetic field fluctuations caused by the 50 Hz mains. These can be avoided by triggering each sequence to start at the same point in the mains cycle. This ensures the same field is present during each repetition of the experiment (ignoring any drift over longer timescales), as long as the complete pulse sequence is short compared with the 20 ms mains period. By inserting a variable delay between the mains-locked trigger and the driving pulse¹ the peak to peak variation in the resonance frequency has been measured to be approximately 15 kHz, corresponding to $\sim 5 \text{ mG}$.

Figure 4.5b shows a frequency scan where the experimental sequence is triggered in phase with the mains. The scan was taken shortly before the non line triggered scan, and the only other experimental difference, other than line triggering, is that 500 sequences rather than 1000 were taken per frequency point. On resonance, there is complete population inversion and the resonance width is 10 kHz, less than for the non line triggered scan, and only slightly more than the 8 kHz expected. A disadvantage of having to line

¹This experiment was actually performed using the Raman lasers to drive the carrier transition of a sideband cooled ion, rather than the magnetic resonance

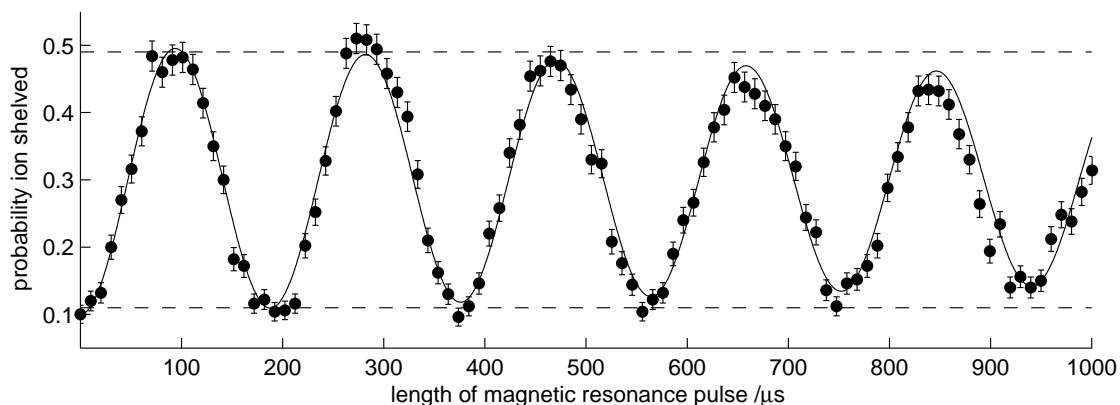


Figure 4.6: Rabi flopping using magnetic resonance. Each point consists of 500 sequences, triggered in phase with the mains. The dashed lines indicate the shelving levels measured in a separate experiment. The fitted curve is a decaying sine function, with floated offset, amplitude, frequency Ω and decay time constant τ . The fitted values are Rabi frequency $\Omega = 2\pi \times 5.3$ kHz, and time constant $\tau = 4$ ms.

trigger is that it decreases the sequence repetition rate to a maximum of 50 Hz, whereas without the line trigger, the sequence repeat rate was limited only by the photon counting periods. To distinguish shelved from non-shelved accurately 2 ms of fluorescence counting was required, giving a total sequence time of < 5 ms (*i.e.* > 200 Hz repetition rate).

As well as the 50 Hz variations in the magnetic field, there is also a slower drift of the magnitude of the magnetic field. For example, approximately 45 minutes after the resonance was located at 4360 kHz, a scan was taken under nominally identical conditions and the resonance occurred at 4367 kHz. The effect of this slow drift is reduced by use of spin echo pulses, as described in section 4.3.2.

4.4.2 Rabi flopping and coherence time

Once the frequency difference between the two qubit states has been measured using the magnetic resonance, Rabi oscillations between the two qubit states can be studied. Figure 4.6 shows the oscillation of population between the two qubit states when the driving frequency matches the qubit splitting ω_s , in a line triggered experiment. The ion undergoes five complete Rabi ‘flops’ where the population oscillates from $|0\rangle \rightarrow |1\rangle \rightarrow |0\rangle$ when the length of the pulse is $950 \mu\text{s}$. In order to deduce the Rabi frequency accurately and to place a rough figure on the coherence time, we fit the data using a decaying sine function. The fitted curve gives a Rabi frequency $\Omega = 2\pi \cdot 5.3$ kHz and a decay time constant $\tau = 4$ ms. The dominant source of decoherence is believed to be magnetic field noise, and indeed in view of the fact that there is no magnetic shielding around the vacuum chamber, we were fortunate to find the field noise was low enough (sub mG) to allow coherence times longer than 1 ms.

The fitted parameters imply that after the ion was driven for a π time ($t = \pi/\Omega$), 99% of the population had transferred from $|0\rangle$ to $|1\rangle$.

Rabi frequencies of order $2\pi \cdot 5$ kHz are the most we are able to achieve with the magnetic resonance coil, for technical reasons. Magnetic Rabi flopping scans taken at the same time as the data in figure 4.5 had a Rabi frequency of $\sim 2\pi \cdot 4.5$ kHz with the Stanford

signal generator producing $0.05 V_{\text{rms}}$ at 4367 kHz and producing a voltage in the pickup coil of $3.3 V_{\text{pk-pk}}$. When the Stanford was driving the coil resonantly, at a frequency of 4400 kHz, a driving voltage of $0.05 V_{\text{rms}}$ produced a pickup of $3.9 V_{\text{rms}}$. When the coil was driven harder, at a drive of $0.07 V_{\text{rms}}$ (pickup $5.5 V_{\text{pk-pk}}$) the variable capacitor intermittently broke down, producing an audible clicking noise and blue sparks. A drive of $0.08 V_{\text{rms}}$ produced constant breakdown, and a blue ‘glow’ on the capacitor. Even if the capacitor were replaced with one able to take higher voltages we would not want to drive the coil this hard. This is because, even before breakdown, at a drive of $0.06 V_{\text{rms}}$ various other independent parts of the experiment were picking up the 4.4 MHz pulse. These include a visible high-frequency modulation on the lock signal of the 393 laser and a change in the point on its reference cavity fringe at which the 397 cooling laser was locked, resulting in a change in the level of ion fluorescence.

4.5 Raman transitions and coupling to the motion

Our second method to drive the qubit coherently is by using a Raman transition. In addition, unlike in the magnetic resonance method where there is no coupling between the internal and motional states of the ion, there can be a large coupling when driving Raman transitions because the optical photons can exchange momentum with the ion.

We will start with a brief review of Raman transitions, followed by a discussion of the interaction of a laser with a harmonically trapped two level atom. Full theoretical descriptions can be found *e.g.* in [18].

Raman transitions

Consider a three level system of states $\{|1\rangle, |2\rangle, |3\rangle\}$ with energies $\{0, \hbar\omega_{21}, \hbar\omega_{31}\}$ driven by two laser fields of frequencies ω_1, ω_2 . The first laser field (ω_1) drives the $|1\rangle \leftrightarrow |3\rangle$ transition with Rabi frequency Ω_1 , the second (ω_2) drives $|2\rangle \leftrightarrow |3\rangle$ with Rabi frequency Ω_2 . Defining the single photon detuning of the first laser from resonance as $\Delta = \omega_1 - \omega_{31}$ and the detuning of the two lasers from Raman resonance as $\delta = \omega_1 - \omega_2 - \omega_{21}$, if $\Delta \gg \Omega_1, \Omega_2, \Gamma, \delta$ then the amplitude $\langle 3|\Psi\rangle$, where $|\Psi\rangle$ is the wavefunction of the system, will be small, and varying on timescales $\sim 1/\Delta$. This means that it can be adiabatically eliminated and the behaviour of population in the lower two levels can be described in terms of a two level system. The detuning and Rabi frequency of this effective two level system are

$$\delta_{\text{eff}} = \delta - \left(\frac{|\Omega_1|^2 - |\Omega_2|^2}{4\Delta} \right) \quad (4.5)$$

$$\Omega_{\text{eff}} = \frac{\Omega_1\Omega_2}{2\Delta}. \quad (4.6)$$

Note that the effective detuning is just the detuning of the two lasers from Raman resonance when the single photon light shifts are taken into account. The other important quantity, affecting the strength of coupling to the motion, is the difference k -vector, $\Delta\mathbf{k} = \mathbf{k}_1 - \mathbf{k}_2$.

Although we discuss Raman transitions using this effective 2 level system, there will still be a small amount of population in the third level, which results in decoherence through photon scattering, the photon scattering rate R being equal to $\rho_{33}\Gamma$ where Γ is the natural decay rate of $|3\rangle$ and ρ is the density matrix. Let N be the mean number of photons scattered when the Raman lasers are used to perform a π pulse on the qubit.

This is given approximately by $N = R\tau = \pi R/\Omega_{\text{eff}}$. This quantity is minimised if the individual Rabi frequencies Ω_1, Ω_2 are equal, in which case

$$N = \frac{\pi\Gamma}{2\Delta}. \quad (4.7)$$

Therefore the number of photons scattered during a π pulse is independent of the effective Rabi frequency.

This supposes that only one frequency of light is present in each of the two laser fields used to drive the Raman transition. In addition to the stimulated emission at the lasing frequency spontaneous emission will also occur which can be amplified by the laser gain medium. This amplified spontaneous emission (ASE), if it produces light resonant with the 397 transition, can cause additional photon scattering. It has been found[39] that laser diodes of the type used in our Raman laser system produce ASE light primarily at frequencies an integral multiple of 60 GHz away from the main emission frequency of the laser, corresponding to the internal cavity modes of the diode. For this reason we set our Raman laser detuning to around 30 GHz from the atomic resonance, so that the ASE modes are far from resonance. At 30 GHz the number of photons scattered according to equation 4.7 during a π transition (on the carrier, see below) is 4×10^{-4} , which is negligible for our purposes. This is for a three level system, where each laser field interacts only with one transition. The actual experimental situation is more complex, with four levels present, and additional laser couplings (see later in the chapter, and figure 4.8). This will result in increased scattering.

Coupling to the motion

In a one-dimensional treatment, the Hamiltonian for a trapped two level ion illuminated by a laser is $H_0 + H_I$ where

$$H_0 = \frac{1}{2}\hbar\omega_s\sigma_z + \hbar\omega_z a^\dagger a, \quad (4.8)$$

$$H_I = \hbar\Omega_0(\sigma^+ + \sigma^-) \cos(kz - \omega t + \phi). \quad (4.9)$$

$a^\dagger(a)$ is the creation(annihilation) operator for the harmonic oscillation of frequency ω_z and Ω_0 is the Rabi frequency of the laser excitation. In the case of a Raman transition treated as an effective 2-level system, $\Omega_0 \equiv \Omega_{\text{eff}}$, $k \equiv \Delta k$, $\omega \equiv \omega_1 - \omega_2$ and ω_s has to be modified to take into account the single photon light shifts. The position operator z found in the interaction Hamiltonian H_I can be written in terms of the creation/annihilation operators as $kz = \eta(a^\dagger + a)$ where we define the Lamb-Dicke parameter

$$\eta = \sqrt{\frac{\hbar k^2}{2m\omega_z}}. \quad (4.10)$$

As with magnetic resonance, we adopt an interaction picture defined by $U_0 = e^{-iH_0 t/\hbar}$ and make the rotating wave approximation to get the interaction Hamiltonian

$$H'_I = \frac{1}{2}\hbar\Omega_0(e^{i\eta(a^\dagger e^{i\phi} e^{-i\omega_z t} + a e^{i\omega_z t})}\sigma^+ e^{-i\delta t} + \text{h.c.}) \quad (4.11)$$

$\delta = \omega - \omega_s$ ($\equiv \delta_{\text{eff}}$ for a Raman transition) being the detuning from the atomic resonance. This Hamiltonian couples each spin/motional state to all the spin/motional states of the opposite spin. If we are only weakly driving the system ($\Omega \ll \omega_z$) and $\delta' = \delta + m\omega_z$ where

m is an integer then terms in the Hamiltonian connecting $|n\rangle$ to $|n+m\rangle$ having small detuning δ' will vary much slower than others, which are being driven far from resonance (detunings $\sim \omega_z$ or greater). We can then think of the system as decoupling into many independent two level systems, the two levels $|\downarrow, n\rangle$ and $|\uparrow, n+m\rangle$ being acted on by an effective Hamiltonian

$$H_{\text{eff}} = \frac{1}{2}\hbar\Omega_0\langle n+m|e^{i\eta(a^\dagger+a)}|n\rangle \left(|\uparrow, n+m\rangle\langle\downarrow, n|e^{i\phi}e^{-i\delta't} + \text{h.c.} \right) \quad (4.12)$$

$$= \frac{1}{2}\hbar\Omega_{n+m,n} \left(\sigma'^+ e^{i\phi_m} e^{-i\delta't} + \sigma'^- e^{-i\phi_m} e^{i\delta't} \right) \quad (4.13)$$

where $\sigma'^+ = \sigma^+|n+m\rangle\langle n|$, $\sigma'^- = \sigma^-|n\rangle\langle n+m|$ are the raising and lowering operators for the effective two level system,

$$\Omega_{n+m,n} = \Omega_0 \left| \langle n+m|e^{i\eta(a^\dagger+a)}|n\rangle \right| \quad (4.14)$$

is the Rabi frequency on the m th sideband, and the phase $\phi_m = \phi + |m|\frac{\pi}{2}$ is also dependent on the sideband driven[49]. Equation 4.13 is now in the same form as the interaction Hamiltonian for magnetic resonance (equation 4.1).

An important parameter regime in trapping ions is the Lamb-Dicke regime, where the spread in the ion's wavefunction is smaller than the wavelength of the radiation driving the motion. This corresponds to $k\sqrt{\langle x^2 \rangle} \ll 1$, which can be written $\eta\sqrt{\langle (a^\dagger + a)^2 \rangle} = \eta\sqrt{2\bar{n} + 1} \ll 1$. Equation 4.14 can then be expanded in powers of η .

In the Lamb-Dicke regime, expanding to second order in η , the Rabi frequency for carrier transitions $\Omega_{n,n} = \Omega_0(1 - \eta^2(2n+1)/2)$. The Rabi frequency for first sideband transitions is $\Omega_{n+1,n} = \Omega_{n,n+1} = \Omega_0\eta\sqrt{n+1}$.

4.5.1 Characterisation of the Raman beams

To drive Raman transitions between $|\uparrow\rangle$ and $|\downarrow\rangle$ we use as our third level one of the two $4P_{1/2}$ states. The two laser fields, which are described in more detail in chapter 2, are derived from a single beam, and each is switched by a single AOM. This allows the frequency difference between the beams to be controlled precisely. One of the beams enters the vacuum system (almost) parallel to the magnetic field, the other beam enters at 60° to the field.

The polarisation vector of any (polarised) laser field can be expressed in terms of three polarisation basis vectors. A natural set of basis states to use when discussing the interaction of light with an ion is that where the three polarisations correspond to the three possible changes in angular momentum projection eigenvalue that can occur in a dipole transition. Thus, if the z axis is defined by the magnetic field, then the three basis states are $\epsilon^0 = \mathbf{z}$, $\epsilon^+ = \mathbf{x} + i\mathbf{y}$, $\epsilon^- = \mathbf{x} - i\mathbf{y}$, which drive $\Delta m_j=0, +1, -1$ (π, σ^+, σ^-) transitions respectively.

Any polarisation vector can be resolved in terms of these basis states. If we have a laser beam propagating at angle θ to the magnetic field, then if it is circularly polarised it is resolved:

$$\epsilon_{\text{circ}+} = \frac{1 + \cos\theta}{2}\epsilon^+ + \frac{1 - \cos\theta}{2}\epsilon^- + \frac{\sin\theta}{\sqrt{2}}\epsilon^- \quad (4.15)$$

If the beam is linearly polarised, with polarisation vector in the plane formed by the beam and the magnetic field then:

$$\epsilon_{\text{lin}} = \frac{\cos\theta}{\sqrt{2}}\epsilon^+ + \frac{\cos\theta}{\sqrt{2}}\epsilon^- + \sin\theta\epsilon^- \quad (4.16)$$

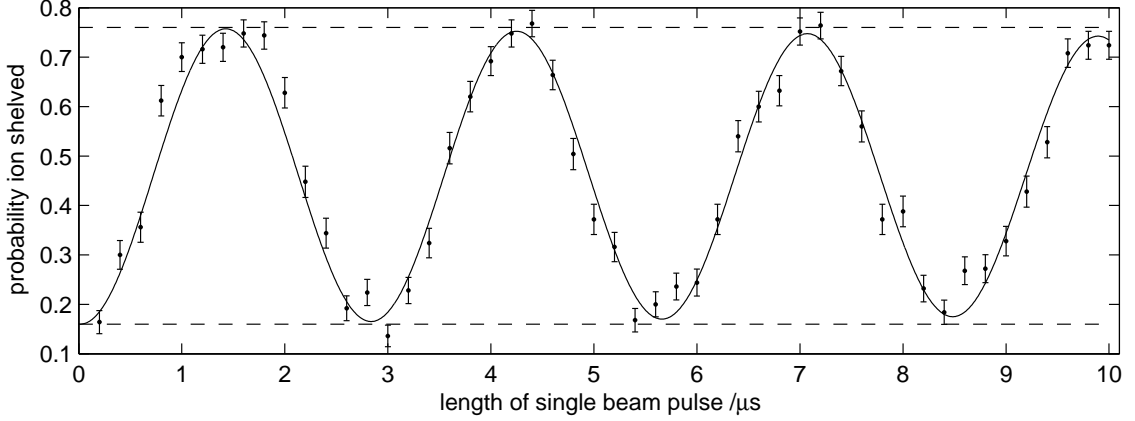


Figure 4.7: Lightshift phase gate. A variable length pulse of light from the parallel Raman beam is turned on during the 1st gap of a magnetic pulse Ramsey-spin echo sequence. The fitted curve has a value of $d\phi/dt = 2\pi \cdot 354$ kHz.

So for instance, when the 60° Raman beam is circularly polarised, then the intensities in the three components able to drive $\sigma^+:\sigma^-:\pi$ transitions are in the ratios 9:1:6, and when this beam is horizontally polarised, the components are in the ratios 1:1:6. The beam we call the parallel Raman beam is actually at about 3° to the field. The reason for this is that for alignment purposes this beam and the 397 pump beam counterpropagate, whereas the magnetic field is aligned with the 850 beam. The effect of this misalignment is small; less than 1% of the beam intensity is of the ‘wrong’ polarisation.

To measure the intensities of the two Raman beams, we make use of the light shifts they induce on the ion. A difference between the light shift of $|\uparrow\rangle$ and $|\downarrow\rangle$ will produce a single-qubit ‘phase gate’, *i.e.* a rotation about the z axis of the Bloch sphere, which we measure by a Ramsey pulse sequence. The two qubit states will have light shifts as follows:

$$\Delta'_{|\uparrow\rangle} = \frac{\Omega_{\sigma^-}^2 + \Omega_{\pi}^2}{4\Delta}, \quad \Delta'_{|\downarrow\rangle} = \frac{\Omega_{\sigma^+}^2 + \Omega_{\pi}^2}{4\Delta} \quad (4.17)$$

assuming $\Delta \gg \Gamma, \Omega_{pol}$ and where Ω_{pol} is the Rabi frequency for the transition driven by light of the relevant polarisation. The qubit will only acquire a phase overall if $\Delta'_{|\uparrow\rangle} \neq \Delta'_{|\downarrow\rangle}$. If the light is applied for a time τ then the resultant phase is

$$\phi_{LS} = (\Delta'_{|\uparrow\rangle} - \Delta'_{|\downarrow\rangle})\tau = \frac{(\Omega_{\sigma^-}^2 - \Omega_{\sigma^+}^2)\tau}{4\Delta} \quad (4.18)$$

To measure this phase we used a Ramsey-spin echo sequence like that shown in figure 4.4. The Raman laser detunings used were around 30 GHz (see equation 4.7 and discussion above).

Figure 4.7 shows the result of using the parallel Raman beam to produce a phase gate. The laser beam was circularly polarised. In the pulse sequence used, the magnetic resonance $t_{\pi} = 40 \mu\text{s}$ and the gap between the pulses $\tau = 104 \mu\text{s}$. During the first gap, the parallel Raman beam was pulsed on for a variable time $t_g = 0.2 \rightarrow 10 \mu\text{s}$. The detuning of the Raman laser from resonance was measured to be $\Delta = -2\pi \cdot 26.7$ GHz using the WA-1500 wavemeter. A $\lambda/4$ waveplate was placed in the parallel Raman beam between

Beam	Beam spot size μm	Beam power mW	Implied I mW/mm^2	Measured $d\phi/dt$ kHz	Implied I mW/mm^2
Parallel	38×19	0.125	99	$2\pi \cdot 354$	113
60°	47×51	1	240	$2\pi \cdot 142$	106

Table 4.1: Summary of the intensity of light from the parallel and 60° Raman beams at the ion as calculated from measured spot sizes and beam powers, and as calculated from the change of phase resulting from light shifts induced on an ion by the beams. In calculating the intensity from the beam power, a 90% transmission through the vacuum window is assumed.

the final mirror and the final lens before the beam enters the trap to make the beam circularly polarised. The power was measured as $125 \mu\text{W}$.

By fitting to the fringes in figure 4.7 the net lightshift $\Delta' = d\phi/dt$ is inferred to be $2\pi \cdot 354 \text{ kHz}$. This implies a Rabi frequency $\Omega_\sigma = 2\pi \cdot 194 \text{ MHz}$ for the circularly polarised beam and so that the beam intensity is $112 \text{ mW}/\text{mm}^2$. Based on the measured beam power and spot size at the ion's position, we would expect the intensity of the beam to be $99 \text{ mW}/\text{mm}^2$.

This procedure of measuring the light shift was repeated using the 60° Raman beam. The beam power was 1 mW , and detuning measured to be $2\pi \cdot 31.2 \text{ GHz}$. The beam was again set to be circularly polarised. By fitting to the fringes observed as a function of beam pulse duration, a net light shift of $2\pi \cdot 142 \text{ kHz}$ is deduced. Taking into account the mix of polarisations expected due to the angle the beam makes with the field (equation 4.15), a beam intensity of $107 \text{ mW}/\text{mm}^2$ is inferred. From the measured spot size and power we would expect an intensity of $240 \text{ mW}/\text{mm}^2$. A summary of the intensities inferred from beam and light shift measurements is shown in table 4.1.

As can be seen, the intensity as deduced from the beam spot size and power can differ by up to a factor two from that deduced from light shift phase measurement. The phase measurement method is precise and as long as the beam polarizations and detunings are known precisely, as they are here, permits a highly accurate value of the light intensity at the ion to be inferred. The method by measurement of the spot size, by contrast, is less accurate and it is not uncommon to have a factor 2 discrepancy between an intensity inferred from spot sizes and the true value. We use the Raman process to drive both carrier and sideband transitions. In order to understand the behaviour, the three level system may be reduced to an effective two level system (see equation 4.13), with the effective detuning dependent on the intensity and detuning of the two driving beams, due to the light shifts (equation 4.5). This has two important consequences. Firstly, if the intensity of the two beams is changed, the detuning of the Raman transitions is also changed. Secondly, the application of the Raman beams will act as a phase gate on the qubit, which would have to be taken into account in any quantum algorithm. However, the fact that our ion is not a true three level system (see figure 4.8) means that we can easily ensure that there is no differential light shift between the two qubit states. To drive the Raman transition one of the beams has to address a π transition, the other a σ^- transition. The π polarised beam will produce no differential light shift. In addition, by making the other beam a mixture of σ^+ and σ^- in equal proportions, rather than purely σ^- , it will also produce no net shift, at the price of reducing the intensity of light which drives the desired Raman transition by a factor two, and increasing photon scattering. With equal Rabi frequencies for the two single photon transitions forming the Raman transition, the total photon scattering

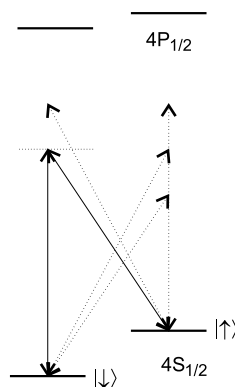


Figure 4.8: 4 level system used for driving Raman transitions. Shown are all the polarisation and frequency combinations experienced by the ion. When both the lasers have linear polarisation, the presence of the fourth level results in there being no net differential light shift on the two qubit states (the ~ 4 MHz Zeeman splitting is negligible compared to the ~ 30 GHz detuning,).

rate due to off resonant excitation, for this configuration of polarisations and intensities, is 2.5 times that given by equation 4.7. We use the same Ramsey-spin-echo sequence to set the polarisation such that the net light shift on the two spin states is small.

Using the results in table 4.1 we can estimate the Rabi frequencies of the two transitions which form the Raman transition, when the polarisations of the beams are set as required. For a linearly polarised parallel beam we obtain a Rabi frequency on the σ^- transition of $\Omega_{\sigma^-}/\sqrt{P} = 2\pi \cdot 389 \text{ MHz}/\text{mW}^{1/2}$. The 60° beam is set to horizontal polarisation. The 60° angle means that $3/4$ of the beam intensity drives π transitions, and should result in $\Omega_{\pi}/\sqrt{P} = 2\pi \cdot 109 \text{ MHz}/\text{mW}^{1/2}$.

4.5.2 Sideband spectrum of a single ion

Figure 4.9 shows a Raman excitation spectrum taken with the Raman beams. The detuning $\Delta = 2\pi \cdot 31.8 \text{ GHz}$ and with 0.10 mW in the parallel Raman beam and 1.2 mW in the 60° beam, this gives an expected effective Rabi frequency of $2\pi \cdot 230 \text{ kHz}$. After the preparation pulse, a $3 \mu\text{s}$ pulse of both the Raman beams was applied to the ion, causing population transfer between the two qubit states to occur if the Raman beams are in resonance with the carrier or a motional sideband. A change in spin state is detected using our readout method. The motional sideband structure is clearly visible in the spectrum. The ion in this experiment was confined with axial trap frequency $\omega_z = 2\pi \cdot 816 \text{ kHz}$ as measured by ‘tickling’, matching the peak separation seen in the spectrum. This results in a Lamb-Dicke parameter $\eta = 0.2$. As can be seen from the relative heights of the sidebands visible in the spectrum, the ion is not in the Lamb-Dicke regime after Doppler cooling (nor would we expect it to be). This data was the first such spectrum obtained in our laboratory. It introduces the motional degree of freedom and its control, which is the theme of the next chapter.

Looking ahead to that chapter, figure 4.10 shows Rabi flopping observed when driving the carrier transition of a sub-Doppler cooled ion with the Raman beams. Although the motional state is not changed by the flopping, the Rabi frequency has a weak dependence on n due to non-zero η . The fit curve also shown on the graph assumes a Rabi frequency

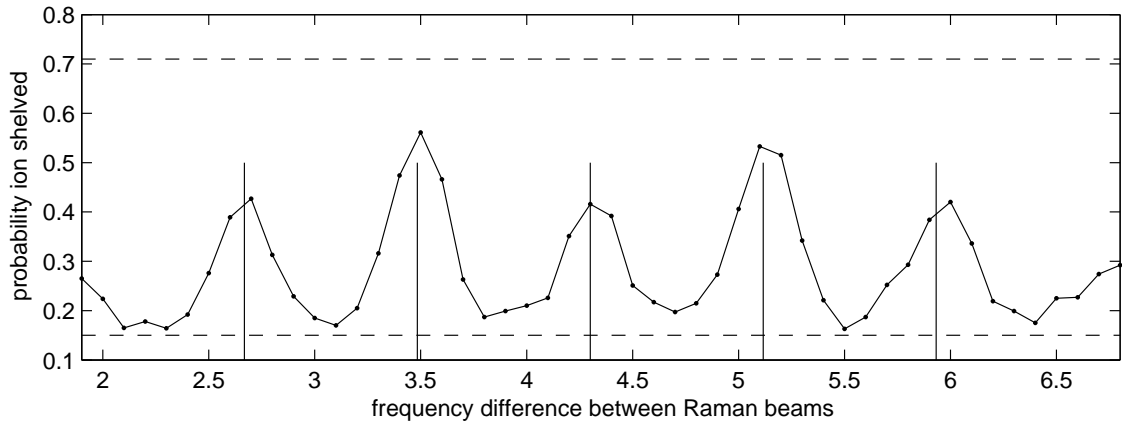


Figure 4.9: Raman spectrum of a single Doppler cooled ion. The lines show the expected positions of carrier and sidebands based on the known qubit splitting of 4.3 MHz and trap frequency 816 kHz.

of $2\pi \cdot 270$ kHz and an excitation of $\bar{n}_z=0.55$. For such an excitation the population in the shelved spin state should be over 99% in the absence of other decohering processes.

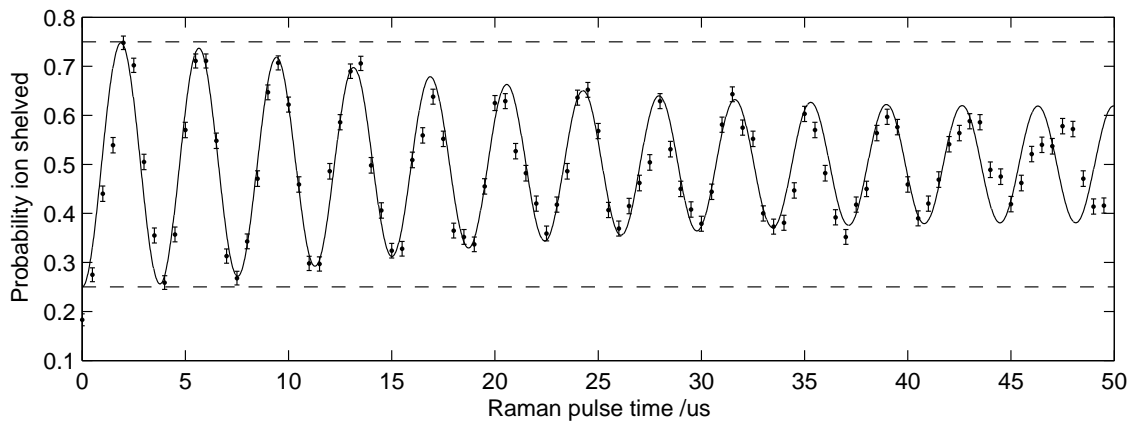


Figure 4.10: Rabi flopping on the carrier transition driven by the Raman beams. Shown are both data points and a theoretical fit. The theory curve assumes a Rabi frequency of $2\pi \cdot 270$ kHz and a thermal distribution of motional state populations with $\bar{n}_z = 0.55$, which agrees with the value measured using the comparison of sideband heights method (see section 5.1.2). The shelving levels marked are those which are used for the fitted curve. The lower shelving level as measured both before and after this data was taken however was 0.18, in agreement with the point taken at zero Raman pulse length but not the value for the fit. The upper shelving level as measured agrees with that for the fit, confirming $\sim 100\%$ population transfer after a π pulse.

Chapter 5

Cooling

This chapter describes laser cooling of a single ion. We start with a general discussion of the Doppler and sideband cooling regimes, and the temperatures expected for a transition of given width in these regimes. We also discuss how we can determine the temperature of a single trapped ion.

The rest of the chapter presents in more detail various Raman sideband cooling schemes and their experimental implementation. In particular we describe the use of a near detuned Raman transition to cool in a continuous way. We present a simple theoretical discussion and our experimental implementation. For blue-detuned laser beams this leads to the case known as EIT cooling[50]. We have also implemented pulsed sideband cooling using a far detuned Raman transition.

5.1 Notes on Cooling and Diagnostics

5.1.1 Cooling Processes

Doppler cooling

The first stage of cooling used in our experiments is Doppler cooling on the strong 397 nm transition. This provides a high cooling rate, down to the Doppler limit temperature, $T_D = \hbar\Gamma/2k_B$ which is 540 μ K for the 397 nm transition. For an $\omega_z/2\pi = 800$ kHz trap this gives a mean vibrational quantum number $\bar{n}_z=14$. In reality, the ion will be hotter than this, due to the fact that instead of a two level atom, we have multiple levels, spread out in frequency by the Zeeman effect, thus increasing the effective width. We also cool with the Doppler cooling laser set to approximately saturate the cooling transition, further widening the transition and pushing up \bar{n}_z . (We saturate the transition so as to increase the number of photons scattered during the detection phase). For experimental convenience, we typically do not try to obtain optimum temperatures close to T_D but accept cooling to temperatures of order $2T_D$. We require temperatures below the Doppler limit, so further cooling by a different technique must be used in any case.

Sideband cooling

As narrower resonances are used to cool the ion, colder temperatures are achievable. When the width of the resonance becomes smaller than the trap frequency, we enter the resolved sidebands regime where the absorption spectrum is greatly modified by the quantized nature of motion in the trap, and splits into sidebands spaced around the carrier. Adjacent

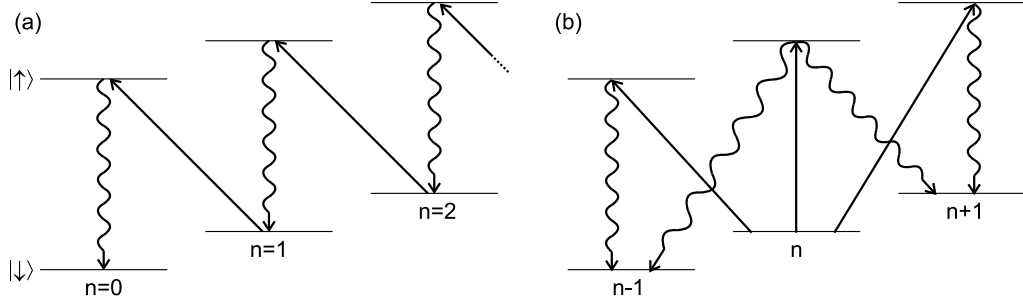


Figure 5.1: Sideband cooling. (a) With the ion starting in the $|\downarrow\rangle$ state, it is driven on its red sideband to the $|\uparrow\rangle$ state with the loss of one vibrational quantum of energy. From this state, it decays to $|\downarrow\rangle$ with only a small average increase in vibrational energy. In this way the ion is optically pumped to the $n = 0$ state. (b) Processes which contribute in determining the minimum temperature, when the ion is in the Lamb-Dicke regime. These processes are excitation on the carrier followed by decay on a sideband (leading to a gain in energy of αE_R on average) or excitation on the first red or blue sideband followed by decay on the carrier.

sidebands are separated from each other by the trap frequency. By tuning the laser(s) driving the transition to a red sideband, absorption to the excited state is accompanied by the reduction of the motional eigenvalue by the number of the sideband tuned to. This process, which is a form of Doppler cooling, is known as sideband cooling. The lowest temperatures are attainable by tuning to the 1st red sideband. This is illustrated in the generic picture of sideband cooling shown in figure 5.1a.

We will calculate the steady state mean vibrational number for sideband cooling of a two level atom. We consider sideband cooling as repeated cycles of absorption of radiation, which change the motional energy in steps of $\hbar\omega_z$, followed by spontaneous decay, which on average will increase the motional energy of the ion by a recoil energy E_R . This energy is spread amongst all three motional modes of the ion. We denote the fraction which heats the axial mode α . If the decay were isotropic, α would be equal to $1/3$. For a dipole transition, $\alpha = 2/5$.

Neglecting saturation effects, the rate of change of axial motional energy for a harmonically trapped two level ion can be written [49, 51]

$$\frac{d\langle E_z \rangle}{dt} = \frac{I\sigma_0}{\hbar\omega_s} \sum_n P(n) \sum_f (E_f - E_n + \alpha E_R) I_{fn} \tilde{g}(\delta - (E_f - E_n)/\hbar) \quad (5.1)$$

where σ_0 is the cross section for resonant absorption, equal to $\lambda^2/(2\pi)$, I is the intensity of radiation, $I_{fn} = |\langle f | e^{i\eta(a^\dagger + a)} | n \rangle|^2$ and $\tilde{g}(\delta)$ is the lineshape function for excitation of the ion, normalised so that $\tilde{g}(0) = 1$.

If the ion is in the Lamb-Dicke regime then we can expand I_{fn} in powers of η (see section 4.5) to get:

$$I_{fn} = \delta_{f,n}(1 - \eta^2(2n + 1)) + \delta_{f,n-1}\eta^2 n + \delta_{f,n+1}\eta^2(n + 1) \quad (5.2)$$

where we have expanded to the second power in η . Only transitions with $\Delta n = \pm 1, 0$ are

possible to this order of η . Substituting into equation 5.1 we obtain

$$\begin{aligned} \frac{d\langle E_z \rangle}{dt} &\simeq \frac{I\sigma_0}{\hbar\omega_s} \sum_n P(n) (\alpha E_R (1 - \eta^2 (2n + 1)) \tilde{g}(\delta) \\ &\quad + (\hbar\omega_z + \alpha E_R) \eta^2 (n + 1) \tilde{g}(\delta - \omega_z) + (-\hbar\omega_z + \alpha E_R) \eta^2 (n) \tilde{g}(\delta + \omega_z)) \\ &\simeq \frac{I\sigma_0}{\hbar\omega_s} \eta^2 \hbar\omega_z \sum_n P(n) (\alpha \tilde{g}(\delta) + (n + 1) \tilde{g}(\delta - \omega_z) - n \tilde{g}(\delta + \omega_z)) \end{aligned} \quad (5.3)$$

where we have used the fact that $E_R = \eta^2 \hbar\omega_z$. Expressing equation 5.3 in terms of \bar{n}_z ,

$$\frac{d}{dt} (\bar{n}_z + \frac{1}{2}) \hbar\omega_z \simeq \frac{I\sigma_0}{\hbar\omega_s} \eta^2 \hbar\omega_z (\alpha \tilde{g}(\delta) + (\bar{n}_z + 1) \tilde{g}(\delta - \omega_z) - \bar{n}_z \tilde{g}(\delta + \omega_z)) \quad (5.4)$$

$$\Rightarrow \frac{d\bar{n}_z}{dt} \simeq \frac{I\sigma_0}{\hbar\omega_s} \eta^2 (\tilde{g}(\delta - \omega_z) + \alpha \tilde{g}(\delta) - \bar{n}_z [\tilde{g}(\delta + \omega_z) - \tilde{g}(\delta - \omega_z)]). \quad (5.5)$$

To find the minimum temperature we set $d\bar{n}_z/dt = 0$

$$\Rightarrow \bar{n}_z = \frac{\tilde{g}(\delta - \omega_z) + \alpha \tilde{g}(\delta)}{\tilde{g}(\delta + \omega_z) - \tilde{g}(\delta - \omega_z)}. \quad (5.6)$$

For a transition of Lorentzian lineshape of linewidth Γ ,

$$\tilde{g}(\delta) = \frac{\Gamma^2}{\Gamma^2 + 4\delta^2} \quad (5.7)$$

and so equation 5.6 gives

$$\bar{n}_z = \frac{(1 + 4\alpha) \Gamma^2}{16 \omega_z^2} \quad (5.8)$$

when the detuning is set to the first red sideband ($\delta = -\omega_z$) and $\frac{\Gamma^2}{\omega_z^2} \ll 1$.

5.1.2 Temperature Diagnostics

We would like to be able to measure the temperature of a single trapped ion. As a ‘‘thermometer’’ we use transitions in the ion that are sensitive to ion motion. The crudest temperature diagnostic would be to measure the width of a transition in the ion, and compare it to the known width for a stationary ion, allowing us to extract the amount of Doppler broadening provided by ion motion. Only very high temperatures (for our purposes) would be able to be measured this way, because the Doppler width would have to be comparable to the width of the resonance being used, and if this resonance width were comparable to or smaller than the trap frequency, then we would have to take into account the sideband structure. Therefore to measure low temperature we need another approach.

When the width of the diagnostic is narrower than the trap frequency, a very elegant method for determining the mean vibrational excitation, \bar{n} , is available[52]. As will be shown below, by measuring the amount of excitation on the 1st red and blue sidebands of the trapped ion, \bar{n} is very easily calculated.

In a thermal state, the probability that an ion in a trap with trap frequency ω occupies the n th motional (harmonic oscillator) state is given by the Boltzmann distribution:

$$P(n) = \frac{e^{-n\hbar\omega/k_B T}}{\sum_{m=0}^{\infty} e^{-m\hbar\omega/k_B T}} = e^{-n\beta} / Z \quad (5.9)$$

where $\beta = \hbar\omega/k_B T$ and $Z = \sum_{m=0}^{\infty} e^{-m\beta} = 1/(1 - e^{-\beta})$. Therefore

$$\bar{n} = \sum_{n=0}^{\infty} nP(n) = \frac{1}{e^{\beta} - 1} \quad (5.10)$$

$$\Rightarrow e^{-\beta} = \frac{\bar{n}}{\bar{n} + 1}. \quad (5.11)$$

This can be substituted into equation 5.9 to give

$$p(n) = \frac{1}{\bar{n} + 1} \left(\frac{\bar{n}}{\bar{n} + 1} \right)^n. \quad (5.12)$$

Next, we examine the sideband excitation probability. If the ion starts in $|\downarrow\rangle$ and the 1st blue sideband is driven, the probability that the ion is excited to the $|\uparrow\rangle$ state is given by

$$p_{\uparrow}^{\text{bsb}}(t) = \sum_{n=0}^{\infty} p(n) \frac{1}{2} (1 - \cos(\Omega_{n,n+1}t)), \quad (5.13)$$

in the limit where only resonant processes need to be included. $\Omega_{n,n+1}$ is the Rabi frequency for transitions between n and $n + 1$, as defined in equation 4.14. Similarly, for the 1st red sideband we have

$$p_{\uparrow}^{\text{rsb}}(t) = \sum_{n=1}^{\infty} p(n) \frac{1}{2} (1 - \cos(\Omega_{n,n-1}t)) = \sum_{n=0}^{\infty} p(n+1) \frac{1}{2} (1 - \cos(\Omega_{n,n+1}t)). \quad (5.14)$$

The particular form of $\Omega_{n,n+1}$ is unimportant for this derivation, only the fact $\Omega_{n,n+1} = \Omega_{n+1,n}$ is necessary. By taking the ratio of these two excitation probabilities and using equation 5.12 we arrive at

$$r = p_{\uparrow}^{\text{rsb}}(t)/p_{\uparrow}^{\text{bsb}}(t) = \frac{\bar{n}}{\bar{n} + 1}. \quad (5.15)$$

Therefore the ratio of the excitation on the two sidebands, r , is related to \bar{n} by a simple algebraic equation[52], and does not depend on the length or strength of the excitation pulse, as long as an equal time/strength pulse is applied to each sideband, and $\Omega_{n,m} \ll \omega$ so that off-resonant sideband excitations are negligible. This ratio tends to 1 for $\bar{n} \gg 1$, and to \bar{n} for $\bar{n} \ll 1$. By rearranging equation 5.15 we obtain our expression for \bar{n} as a function of r :

$$\bar{n} = \frac{r}{1 - r}. \quad (5.16)$$

Another diagnostic method is to observe Rabi oscillations of the internal state when a blue sideband transition is being driven. Since the Rabi frequency of such an excitation depends on the vibrational excitation of the ion, the excited state population is a sum of oscillations with different frequencies. The values of $P(n)$ can then be extracted by fitting to the observed data. This method is particularly useful in determining the vibrational occupation probabilities of non thermal states[40]. Although the Rabi frequencies of transitions on the carrier also have a motional dependence, the dependence is weak. We have not used this method in the work presented here.

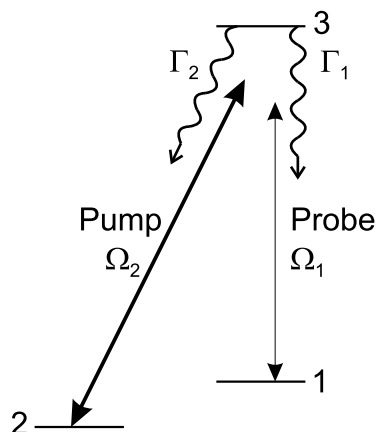


Figure 5.2: The three-level system. Ω_1, Ω_2 are the Rabi frequencies of the two lasers, $\Gamma_1(\Gamma_2)$ the decay rate from the excited state $|3\rangle$ to $|1\rangle$ ($|2\rangle$). The detunings of the lasers from resonance are $\Delta_1 = \omega_{L1} - \omega_{31}$ and $\Delta_2 = \omega_{L2} - \omega_{21}$

5.2 Continuous Raman Sideband Cooling

To get to a lower temperature than that provided by Doppler cooling on the 397 transition, a narrower resonance is required and in practise it is convenient to enter the sideband cooling regime. The $4S_{1/2} \leftrightarrow 4P_{1/2}$ transition we use for Doppler cooling is not the narrowest single-photon transition in $^{40}\text{Ca}^+$. By implementing sideband cooling using one of the $4S_{1/2}$ to D state quadrupole transitions which have a width of < 1 Hz an excitation of $\bar{n}_z \sim 10^{-9}$ is theoretically possible, albeit with an impossibly slow cooling rate as the maximum photon scattering rate on the transition is < 0.5 photons/s. The ion trap group at the University of Innsbruck use one of these transitions in calcium to sideband cool. The cooling rate is increased by coupling the excited state to a third level, to increase the effective linewidth[53]. The cooling transition is $4S_{1/2} \leftrightarrow 3D_{5/2}$, which is broadened by applying light to the $4P_{3/2} \leftrightarrow 3D_{5/2}$ transition. They have observed cooling to $\bar{n}_z \leq 0.01$ in a trap with $\omega_z = 2\pi \cdot 4.51$ MHz[54].

We do not have a laser able to address the narrow quadrupole transitions in the ion. However it is possible to create a narrow resonance in a three-level system. In our experiments the three-level system is formed by $\{|\downarrow\rangle, |\uparrow\rangle, |4P_{1/2} m_J\rangle\}$, where $m_J = +\frac{1}{2}$ or $-\frac{1}{2}$, driven by two laser beams at 397 nm which are detuned from the single photon resonance. Such a system has been used, again by the University of Innsbruck ion trap group, to cool an ion close to the ground state ($\bar{n}=0.1$ in an $\omega_z = 2\pi \cdot 3.3$ MHz trap[55]) using a scheme proposed by Morigi *et al.*[50].

Excitation profile of the three-level system

We start by reviewing the general three-level system, in the λ configuration (see figure 5.2). It can be shown [48] that in the rotating wave approximation, and under the further approximations of zero laser linewidth, $\Omega_1^2 \ll \frac{\Gamma_1}{\Gamma_2} \Omega_2^2$ and $\Delta_1^2 \gg \Gamma^2, \delta^2$, in steady state the excited state population ρ_{33} is

$$\rho_{33} = \frac{\Omega_1^2 \delta^2 \Gamma / \Gamma_1}{4\Delta_1^2 (\delta - \Delta')^2 + \delta^2 \Gamma^2 + 4\delta^2 \Delta_1^2 \frac{\Omega_1^2 \Gamma_2}{\Omega_2^2 \Gamma_1} + \frac{\Omega_2^2 \Omega_1^2}{4} \left(\frac{\Gamma_2}{\Gamma_1} + 2 \right)} \quad (5.17)$$

where $\delta = \Delta_1 - \Delta_2$, $\Gamma = \Gamma_1 + \Gamma_2$ and $\Delta' \equiv \frac{\Omega_2^2}{4\Delta_1}$ is the lightshift that levels 2 and 3 experience when $\delta = 0$. At $\delta = 0$ there is no excitation (this is a dark resonance), and the excitation has a local maximum at $\delta \simeq \Delta'$ (bright resonance).

The more intense laser beam (Rabi frequency Ω_2) is called the pump beam, the less intense (Rabi frequency Ω_1) the probe beam.

Near the bright resonance, the population in the excited state can be further approximated

$$\rho_{33}(\delta) \simeq \frac{\Omega_{\text{eff}}^2 \left(\frac{\delta}{\Delta'}\right)^2 \frac{R}{4\Gamma_1}}{(\delta - \Delta')^2 + \frac{R^2}{4} + \frac{\Omega_{\text{eff}}^2 \Gamma}{2\Gamma_1}} \quad (5.18)$$

where two further quantities, R and Ω_{eff} have been introduced.

$$R \equiv \frac{\Omega_2^2}{4\Delta_1^2} \Gamma \quad (5.19)$$

and $R\rho_{22}$ is the rate at which scattering occurs on the 2-3 transition which is being strongly driven by the pump laser. $\Omega_{\text{eff}} \equiv \Omega_1\Omega_2/(2\Delta_1)$ is the effective Rabi frequency for Raman transitions between 1 and 2, *cf.* section 4.5.

The non-Lorentzian excitation profile given by equation 5.18 has a FWHM of

$$f = \left(R^2 + \Omega_{\text{eff}}^2 \frac{2\Gamma}{\Gamma_1} \right)^{1/2} \quad (5.20)$$

Cooling with a three-level system

The theoretical analysis of cooling a trapped ion using resonances in a three-level atom was considered by Lindberg and Javanainen[56]. They consider an ion in the Lamb-Dicke regime, and expand the equations of motion to 2nd order in the Lamb-Dicke parameters of the two beams. The problem reduces to a set of rate equations for the motional states where, due to the Lamb-Dicke approximation, only transitions between adjacent motional states are possible. They give a general procedure for obtaining the rates for transitions between the motional states from the steady state solution of the non-confined three-level system. These rates therefore take into account the coherences that are important in the behaviour of a three-level system and they allow final temperatures and cooling rates to be calculated. They also gave analytic solutions for the limiting cases of laser intensity tending to zero and for detunings becoming large.

Morigi *et al.*[50] considered the effect of the asymmetry, and more specifically the dark resonance, seen in the excitation profile on the cooling. By careful selection of laser parameters, they show that it is possible to tune the dark resonance so that one of the two heating processes that occur in the Lamb-Dicke limit of laser cooling does not occur. Eliminating this process, which is off-resonant excitation on the carrier ($|n\rangle \rightarrow |n\rangle$) followed by a spontaneous decay, results in the final temperature being reduced. This special case of Raman sideband cooling which makes use of electromagnetically induced transparency to suppress an excitation process has been dubbed ‘EIT cooling’.

We will describe a more approximate treatment of the cooling dynamics than is used in these papers, analogous to that used in section 5.1.1 to derive the steady state temperature for two-level sideband cooling. This provides insight into the cooling process and leads in some cases to the same predictions for temperature and cooling rate.

Suppose the ion starts in $|1\rangle$, then the Raman process will result in population transfer to $|2\rangle$. From there, the intense pump beam (Ω_2) will off-resonantly excite the ion to $|3\rangle$,

whence it decays to $|1\rangle$ or $|2\rangle$. When the Raman transition is tuned to the first red sideband (*i.e.* probe detuning $\delta = \Delta' - \omega_z$), the Raman process driving population from $|1\rangle|n\rangle \rightarrow |2\rangle|n-1\rangle$ acts like the excitation process in two-level sideband cooling. The off resonant excitation from $|2\rangle$ which optically pumps to ion back to $|1\rangle$ is the ‘decay’ step.

For our three-level system driven by a pair of 397 beams, $|1\rangle \equiv |\downarrow\rangle$, $|2\rangle \equiv |\uparrow\rangle$, and $|3\rangle \equiv |4P_{1/2}, m_J = -1/2\rangle$. This means that the pump beam has σ^- polarisation, and the probe π polarisation. The Clebsch-Gordon coefficients are such that $\Gamma_1 = \Gamma/3$ and $\Gamma_2 = 2\Gamma/3$. This implies that on average it takes 3 excitations from $|1\rangle$ to optically pump back to $|2\rangle$. The rate of decays in the system is $\Gamma\rho_{33}$, giving the rate of change of motional energy

$$\begin{aligned} \frac{d\langle E_z \rangle}{dt} &\simeq \frac{1}{3} \sum_n P(n) \sum_f (E_f - E_n + \alpha E_R) I_{fn} \Gamma \rho_{33} (\delta - (E_f - E_n)/\hbar) \\ &\simeq \frac{1}{3} E_R \Gamma \sum_n P(n) (\alpha \rho_{33}(\delta) + (n+1) \rho_{33}(\delta - \omega_z) - n \rho_{33}(\delta + \omega_z)) \end{aligned} \quad (5.21)$$

where we have again expanded I_{fn} to 2nd power in η . The factor $1/3$ accounts for the fact that in steady state the probe excitation rate is $\Gamma_1 \rho_{33} = \Gamma \rho_{33}/3$. Because of the three decays, α also has to incorporate a factor 3. Note that the I_{fn} factor in this equation arises from the fact that since the coupling of the lasers to the ion is weaker when a sideband is being driven, equation 5.18 has to be modified by replacing Ω_1^2 with $I_{fn} \Omega_1^2$. Doing this in the numerator of equation 5.18 leads to the I_{fn} we see. Equation 5.21 does not however take into account the effect this substitution has on the denominator of equation 5.18, where it effectively reduces the power broadening when a sideband is being driven. This reduced broadening is not taken account of here, to simplify the equations.

The steady state solution is

$$\bar{n}_z = \frac{\rho_{33}(\delta - \omega_z) + \alpha \rho_{33}(\delta)}{\rho_{33}(\delta + \omega_z) - \rho_{33}(\delta - \omega_z)}. \quad (5.22)$$

(*cf.* equation 5.6).

Setting the detuning so that the bright resonance addresses the first red sideband, *i.e.* $\delta = \Delta' - \omega_z$:

$$\bar{n}_z = \frac{\rho_{33}(\Delta' - 2\omega_z) + \alpha \rho_{33}(\Delta' - \omega_z)}{\rho_{33}(\Delta') - \rho_{33}(\Delta' - 2\omega_z)} \quad (5.23)$$

$$\simeq \frac{f^2}{16\omega_z^2} \left(\left(1 - \frac{2\omega_z}{\Delta'}\right)^2 + 4\alpha \left(1 - \frac{\omega_z}{\Delta'}\right)^2 \right). \quad (5.24)$$

where we have expressed \bar{n}_z in terms of the width f of the bright resonance and the light shift Δ' .¹

The time dependence of n_z is

$$\begin{aligned} \frac{d\bar{n}_z}{dt} &\sim \frac{1}{3} \eta^2 \Gamma \sum_n P(n) (\alpha \rho_{33}(\delta) + (n+1) \rho_{33}(\delta - \omega_z) - n \rho_{33}(\delta + \omega_z)) \\ &= \frac{1}{3} \eta^2 \Gamma (\alpha \rho_{33}(\delta) + \rho_{33}(\delta - \omega_z) - \bar{n}_z [\rho_{33}(\delta + \omega_z) - \rho_{33}(\delta - \omega_z)]). \end{aligned} \quad (5.25)$$

¹Note that this does not take into account the reduced power broadening of sidebands as noted above. When $\eta \Omega_{\text{eff}} \ll R$ we can simply set the power broadening of the sidebands to zero, and then the predicted value of \bar{n}_z is smaller by a factor $1 + 6(\Omega_{\text{eff}}/R)^2$.

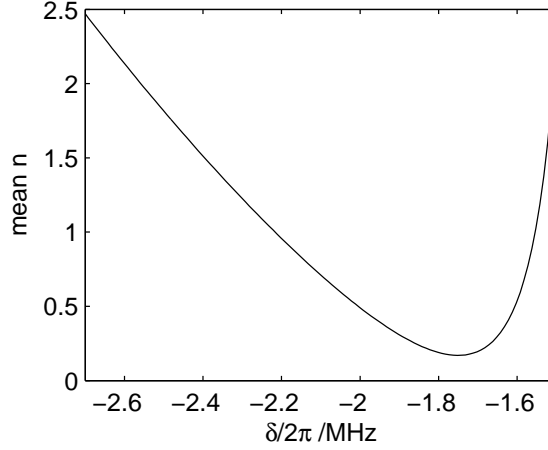


Figure 5.3: Plot of theoretical \bar{n} as a function of δ . Parameters used are $\Omega_1 = 0.05\Gamma$, $\Omega_2 = \Gamma$, $\Delta_1 = -6\Gamma$, where $\Gamma = 2\pi \cdot 22$ MHz and a trap frequency $\omega_z = 2\pi \cdot 815$ kHz. Note that the 2nd sideband is ignored in this theory.

This leads to exponential decay of \bar{n}_z to the final limiting value given by equation 5.24. The rate for this decay (*i.e.* the cooling rate) is then

$$\begin{aligned}
 & \frac{1}{3}\eta^2\Gamma(\rho_{33}(\delta + \omega_z) - \rho_{33}(\delta - \omega_z)) \\
 &= \frac{1}{3}\eta^2\Gamma(\rho_{33}(\Delta') - \rho_{33}(\Delta' - 2\omega_z)) \\
 &\simeq \eta^2 \frac{\Omega_{\text{eff}}^2 R}{f^2} \tag{5.26}
 \end{aligned}$$

when the detuning is set to the first red sideband. The cooling rate is maximised for a given width f when $R = \sqrt{3}\Omega_{\text{eff}}$. In this case, the cooling rate is proportional to the resonance width.

We can compare the final temperature for continuous Raman sideband cooling with that obtained from cooling a two-level atom with a linewidth Γ equal to the width of our resonance f , which was given in equation 5.8. If we start by considering the case where the two cooling beams are red detuned from the single-photon resonance, then this will give negative light shift Δ' and so the final temperature will always be higher than for the two-level case. This is because compared with a Lorentzian lineshape the asymmetry of the excitation enhances the off-resonant carrier and blue sideband excitation which heats the ion.

If the cooling beams are to the blue of the ionic transition, then the light shift is positive, and it is possible to attain temperatures cooler than an equivalent two-level system. In particular, if we consider the case of Morigi *et al.*'s 'EIT' cooling which is realised when the light shift $\Delta' = \omega_z$ then the term in α in equation 5.24 (which is the result of excitation on the carrier) disappears. In that case $\bar{n}_z = f^2/(16\omega_z^2)$, in agreement with equation 8 of [50].

We can use equation 5.22 for the steady state temperature as a function of the excited population, alongside equation 5.17 which gives us these populations, to see what temperature we might expect as a function of the Raman detuning and to confirm that the approximations we made in equation 5.24 are valid. Figure 5.3 shows \bar{n} as a function of δ . The parameters used are $\Omega_1 = 0.05\Gamma$, $\Omega_2 = \Gamma$, $\Delta_1 = -6\Gamma$, where $\Gamma = 2\pi \cdot 22$ MHz and the

trap frequency $\omega_z = 2\pi \cdot 815$ kHz. These parameters combine to give a resonance width of $2\pi \cdot 0.27$ MHz and light shift $-2\pi \cdot 0.92$ MHz. The minimum ($\bar{n}=0.17$) occurs at a detuning within $2\pi \cdot 20$ kHz of the shifted first red sideband and is only different by 2% from that predicted by equation 5.24.

5.3 Red Detuned Continuous Cooling

In this section and the next we will present our experimental implementation of continuous Raman sideband cooling. This section covers experiments with red detuned 397 pump and probe, and the next section covers blue detuned ‘EIT’ cooling.

Although for a given set of parameters ($\Omega_1, \Omega_2, |\Delta|$) working on the red side will always give a larger theoretical steady state ion temperature than at blue detuning, experimentally working with a red detuning is easier, which is why we attempted this first. It is easier because the fact that the lasers are red detuned means that they will still provide small levels of Doppler cooling of the ion irrespective of what the two photon resonance is doing. Conversely, blue detuned beams will heat the ion for all detunings except within the small capture range of the two-photon feature.

In our experimental implementation of continuous Raman sideband cooling, the 397 probe and pump beams are as described in section 2.2.1 of chapter 2. The 397 laser has a linewidth of several MHz. However because the two beams are both derived from the same laser the approximation of zero laser linewidth made in deriving equation 5.17 is reasonable as both beam undergo the same frequency fluctuations. Their difference frequency is stable to within ~ 10 kHz (see section 2.3).

The alignment of beams into the vacuum system was shown in figure 2.6. The pump beam is aligned close to counterpropagating the direction of the magnetic field, differing by $\sim 3^\circ$. It is set to be circularly polarized. Impurity of polarisation due to misalignment with the field is negligible: 99.9% of the intensity of the light felt by the ion is of the correct polarisation. Some experiments were performed with σ^+ polarised light, others used σ^- .

A note on pump polarisation and red and blue sidebands. For the three level ion, the first red sideband occurs at a probe frequency of $\delta = \Delta' - \omega_z$, *i.e.* one trap frequency to the red of the carrier transition. It is possible for confusion to arise when we relate this to the real trapped ion. If the pump beam is σ^- polarised then the ion is optically pumped into the $|\downarrow\rangle$ state, which then corresponds to $|1\rangle$ in the three level theory. The first red sideband then corresponds to the $|\downarrow\rangle|n\rangle \leftrightarrow |\uparrow\rangle|n-1\rangle$ transitions and the first blue sideband the $|\downarrow\rangle|n\rangle \leftrightarrow |\uparrow\rangle|n+1\rangle$ transitions. If however the pump beam is σ^+ polarised then the ion is optically pumped into $|\uparrow\rangle$ (and so $|\uparrow\rangle$ is now $|1\rangle$). The red sideband now corresponds to $|\uparrow\rangle|n\rangle \leftrightarrow |\downarrow\rangle|n-1\rangle$, the same transitions we labelled the first blue sideband when we had a σ^- pump beam.

When discussing Raman transitions driven with the Raman laser (rather than the pump/probe) we use the same labelling: we refer to those sideband transitions which cool the ion when it is in the initial internal state produced by the pump beam as red sidebands, and to transitions which heat the ion when it is in the optically pumped initial state as blue sidebands.

The probe beam enters the vacuum system at 60° to the magnetic field. It is set to horizontal polarization. Due to the fact that the beam is not perpendicular to the magnetic field, the ion sees the beam as a mixture of polarizations such that 3/4 of the intensity is π polarised, the rest divided equally between σ^+ and σ^- .

Note that it is necessary that the pump beam is circularly polarised. This is because although the theory in the previous section ignored the fact that there are actually four levels, this fourth level does exist, and can be coupled to the $|\uparrow\rangle$ and $|\downarrow\rangle$ levels by the two lasers. If the π polarized beam were the pump, then the cooling mechanism would be completely disrupted, because the pump beam would drive single photon transitions from both the ground states removing the ‘directionality’ required of the repumping step.

As with the two Raman beams, the difference k -vector of the cooling beams lies almost parallel to the trap axis, so only axial transitions will be driven by the cooling beams and thus only the axial mode will be cooled. The Lamb-Dicke parameter for the Raman process is equal to ~ 0.2 for a 800 kHz axial trap.

5.3.1 Fluorescence spectrum

The first experiments in cooling with this two-photon transition were performed before we had installed the Raman beams which could be used for temperature measurement, so we needed an alternative diagnostic that would give us information about the cooling. We found that observing the fluorescence emitted by the atom during the continuous Raman cooling as a function of the detuning of the probe beam gave diagnostic information, and allowed an initial estimate of the temperature. This method of viewing the fluorescence only works when the cooling lasers are red detuned.

Because the photon scattering rate during the Raman cooling is orders of magnitude smaller than during Doppler cooling (as we have seen, only 3 photons are scattered by the ion for each trip around the cooling cycle), long integration times were used, and efforts were taken to reduce the amount of stray light reaching the PMT from light sources in the lab and from scattering inside the vacuum system. It was for this reason that the pinhole was inserted into the imaging system, so that only a small area centred on the ion is imaged on the PMT (see section 2.1.5).

The observed fluorescence in steady state while the probe is slowly scanned is shown in figure 5.4. In this scan, $\Delta \sim 2\pi \cdot 180$ MHz and the powers in the probe and pump lasers were $1.7 \mu\text{W}$ and $160 \mu\text{W}$ respectively. For each detuning photons were counted for 42 s.

The fluorescence spectrum obtained has a complex structure. The main peak, labeled a, occurs at a frequency difference between the two laser beams of 7.1 MHz. This frequency difference isn’t equal to $\delta/2\pi$, as the two transitions being driven have different resonant frequencies, due to the Zeeman splitting, which was 4.2 MHz at the time this scan was taken (measured by magnetic resonance). Therefore the main peak is at a Raman detuning $\delta/2\pi = -2.9$ MHz. The separation of peaks b to h accurately matches the axial trap frequency of 812 kHz, which was measured by ‘tickling’ (see section 2.1.2), implying that they are motional sidebands of the Raman transition. The main peak does not fit into this pattern, lying 575 kHz from peak b.

The carrier transition will be located at $\delta = \Delta'$, the lightshift due to the intense pump laser, and since the pump is red detuned, the lightshift is negative. At least some of the sidebands on the scan shown have a positive δ , implying that they must be blue sidebands. Seeing blue sidebands was not expected, as they should be heating the ion, at least according to the simple model in which a sideband transition changes the motional energy while the repumping process does not. If this were the whole story then the ion would be heated until it had sufficient energy to leave the centre of the trap and so uncouple from the lasers. In that case in the steady state no fluorescence would be seen. We explain the observations by including the cooling effect of the (far-off-resonant) single

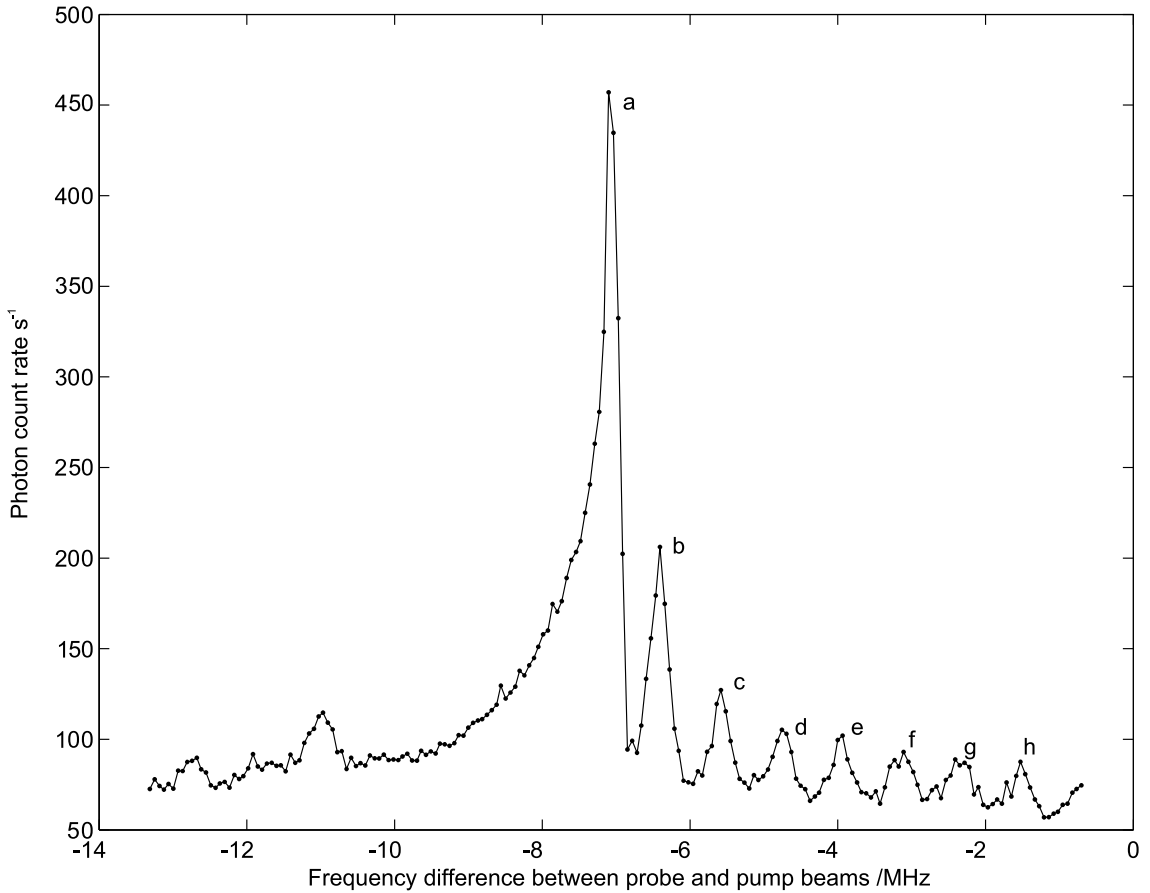


Figure 5.4: Continuous cooling fluorescence scan, showing the number of counts due to ion fluorescence as a function of the frequency of the probe laser. For each probe frequency photons were counted for 42 s. A background of 175 counts/s, mainly due to light scattering from the pump beam into the PMT, has been subtracted from the count rate. The signal is small compared with that produced during Doppler cooling, and for comparison an intense, resonant 397 nm laser produces $\sim 23,000$ counts/s. A series of sharp resonances can be seen in the spectrum. The separation of peaks b to h matches that of the axial trap frequency, measured by tickling to be 812 kHz. Peak a does not fit this pattern, lying 575 kHz to the red of peak b. The detuning from resonance $\Delta \sim 2\pi \cdot 180$ MHz and the probe and pump laser powers were $1.7 \mu\text{W}$ and $160 \mu\text{W}$ respectively.

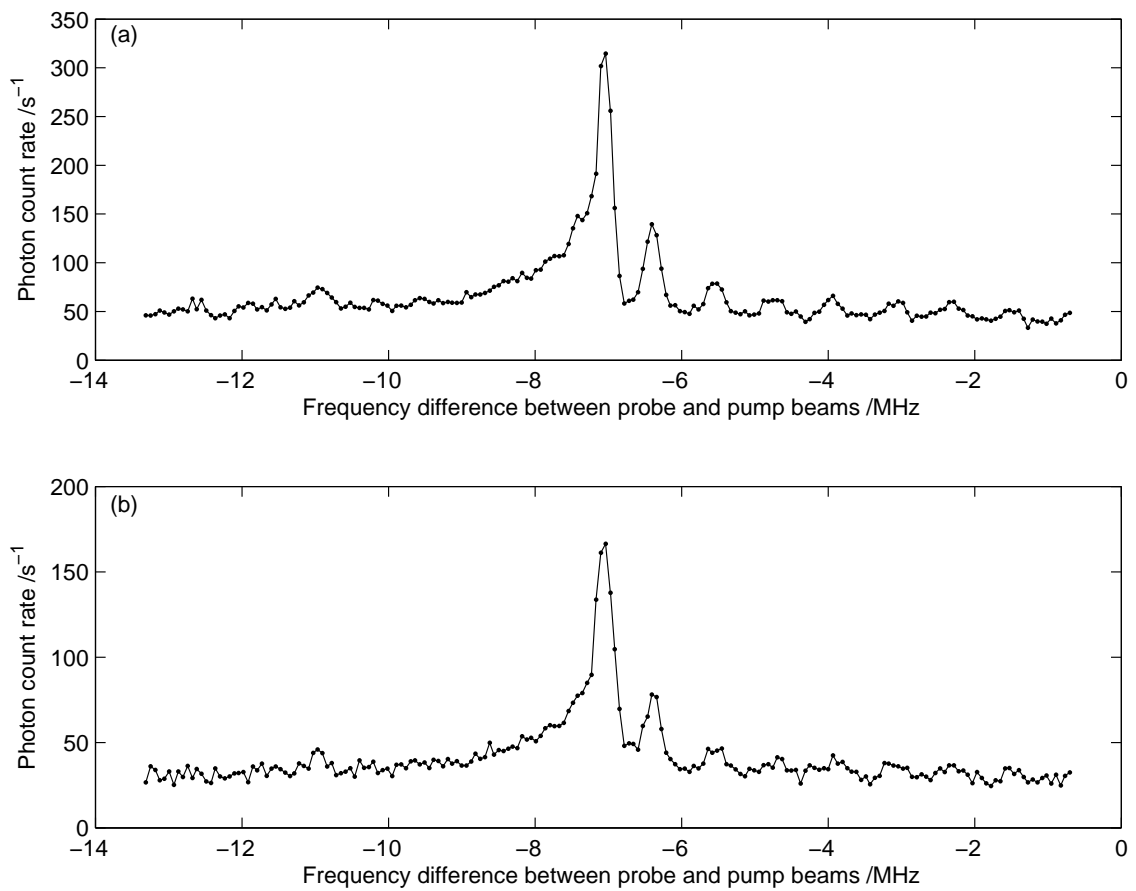


Figure 5.5: Continuous cooling fluorescence scan, showing the number of counts due to ion fluorescence as a function of the frequency of the probe laser. Conditions are identical to those in figure 5.4 except for the probe powers which are 1.0 μW for (a) and 0.46 μW for (b).

photon transitions, see below.

A further difficulty in interpretation is that it is not immediately clear which of the peaks is the carrier. The two possibilities that seem most reasonable is that one of peaks a or b is the carrier transition. The reason peak a is a candidate is that it is the highest peak and has the lowest (*i.e.* most negative) value of δ . When the lasers are tuned to a red sideband then we would expect the ion to be in the $n = 0$ state with high probability. Therefore we expect little fluorescence when tuned to the first red sideband, as there is no lower energy motional state for the ion to make a transition to, but we do expect fluorescence when tuned to the carrier. However, although peak a is at the lowest detuning, it doesn't fit in the pattern of peaks b to h, which are separated from one another, as stated above, by the trap frequency. So if peak a is not the carrier for the reason that it doesn't appear to be a 'normal' sideband, then peak b is the other possibility.

Fluorescence spectra with different probe powers but otherwise identical conditions are shown in figure 5.5.

Determining the light shift

We carried out a series of experiments to determine the light shift caused by the pump beam, and thus find which of the peaks in the fluorescence spectrum corresponds to the carrier. In this thesis so far, we have separately discussed two different pairs of beams which are used to drive Raman transitions. In this section we will now discuss experiments in which both sets of beams are used. So as to avoid confusion let us repeat the terminology we have adopted to describe them. The pair of beam which drive the Raman transition used for continuous sideband cooling are the "397 pump and probe beams". The pair of beams which we call the "Raman beams" are multi-purpose and are used here to measure the light shift caused by the pump beam. They are more intense and have 30 GHz detuning.

Using the 30 GHz detuned Raman beams, we recorded the positions of sidebands (see section 4.5.2 of chapter 4), and thus the splitting between the two qubit states while the pump beam was on. This experiment was performed at a later date from when the high resolution fluorescence spectrum shown in figure 5.4 was taken and the details of the experiment had changed in the intermediate period. The major difference was that the pump beam polarisation was changed from σ^+ (figure 5.4) to σ^- (figure 5.6). In addition, the spot sizes of the probe/pump beams had also been changed, so beam powers aren't immediately comparable. Finally, the axial trap frequency was slightly different, being $2\pi \cdot 816$ kHz. The fluorescence spectrum for which we aimed to discover the pump beam lightshift is shown in figure 5.6a. The spectrum was taken with a pump beam power of $18.9 \mu\text{W}$. The Zeeman splitting of the ground state was measured by the magnetic resonance method to be 4.28 MHz. After completing the fluorescence scans, a series of Raman scans, similar to that shown in figure 4.9, were taken with the pump beam present at various power levels.

Figure 5.6b shows the positions of peaks in these Raman spectra as a function of pump power. Using the results of the four low pump powers, indicated by circular data points, we get a lightshift of $-37.5 \text{ kHz}/\mu\text{W}$ of pump power. Therefore the pump power $18.9 \mu\text{W}$ implies a lightshift of -0.71 MHz in the experiment giving the spectrum of figure 5.6a. This unambiguously indicates that peak b corresponds to the carrier transition². The de-

²Also shown in the 2nd graph are positions of two sidebands measured with the pump power equal to $18.9 \mu\text{W}$. The photon scattering from the pump at this power meant that we had to quadruple the power of each of the Raman beams to be able to see the sideband structure.

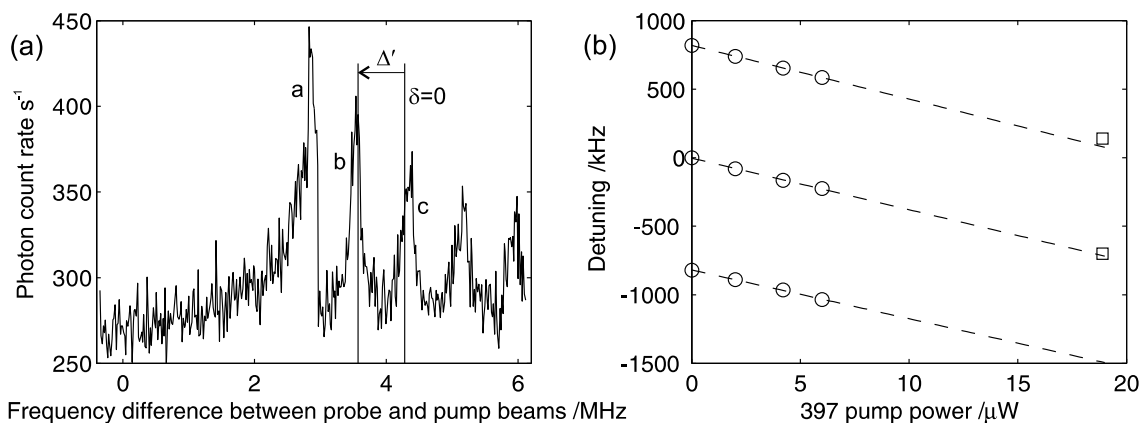


Figure 5.6: (a) Fluorescence detected as a function of probe detuning during continuous Raman cooling. The vertical lines indicate the probe frequency corresponding to $\delta = 0$ *i.e.* pump and probe beams in Raman resonance which occurs when the frequency difference equals the Zeeman splitting of 4.28 MHz, and where the carrier transition is expected, based on the light shift measurement in (b) and measured pump power. (b) Positions of carrier and first red and blue sidebands in the 30 GHz detuned Raman spectrum, as a function of the power of the pump beam, which was also on while these spectra were taken. Fitting to the data at the four lowest pump powers gives a lightshift of $-37.5 \text{ kHz}/\mu W$ of pump power.

tuning of the pump beam $\Delta = 2\pi \cdot 150 \text{ MHz}$ combined with the light shift measurement enables us to deduce the Rabi frequency $\Omega_2/\sqrt{P} = 2\pi \cdot 4.7 \text{ MHz}/\mu W^{1/2}$.

Model of cooling process

Having determined that peak b is the carrier of the cooling Raman transition, a model explaining the fluorescence spectrum will now be put forward. The model will be presented for the conditions used in the initial experiments, *i.e.* σ^+ polarized pump beam.

During the cooling there are two processes occurring in the ion. The two-photon Raman process moves population between the two ionic ground states, $|\uparrow\rangle$ and $|\downarrow\rangle$. Also the σ^+ polarized pump laser off resonantly excites the ion if it is in $|\downarrow\rangle$, optically pumping into the $|\uparrow\rangle$ state. Consider starting with an ion in the $|\uparrow\rangle$ state. Depending on the detuning for the two-photon process, the ion will be transferred to the $|\downarrow\rangle$ state, with some average change in n , the change depending on which particular sideband(s) are closest to resonance (note that the average change in n does not have to be integral). When in the $|\downarrow\rangle$ state, the ion will then be pumped back to $|\uparrow\rangle$. The repumping step, which consists on average of 3 absorption decays will also have an effect on the motional state of the ion. A decay on average heats the ion by a fraction of recoil energy $E_R = (\hbar k)^2/(2M)$ as discussed above. For an 800 kHz trap, $E_R/(\hbar\omega_z) = 0.04$. The effect of the absorption, however, varies, heating the ion if it is in a low n state, and cooling it if n is high. For low n two effects serve to heat the ion. Firstly, the level structure is not symmetric, stopping at $n = 0$. The effect of this is most obvious for the $n = 0$ motional state. Absorption out of this level can only either leave the ion in the same motional state, or increase n . The other effect is that even when motional states exist below the one the ion is in, the Rabi frequencies favor increase in n . For example $\Omega_{1,2} = \sqrt{2}\eta\Omega_0$ whereas $\Omega_{1,0} = \eta\Omega_0$. For large n the Rabi

frequencies for heating and cooling are almost balanced, but here the transition to lower n will be more likely because the detuning from the resonance is slightly less. That is to say the red detuned pump beam is providing weak Doppler cooling. Equation 5.24 was derived by considering only those processes important for low n , and detuning set to the first red sideband.

The steady state temperature is reached when the heating and cooling rates are equal. When the detuning of the probe is to the blue of the carrier, the Raman transition is heating the ion, and the ion heats up until the cooling provided by the repumping step matches it. The reason that a sideband structure is seen on the blue sidebands is the variation in the rate at which the process is occurring. When tuned to a sideband the Raman transition occurs at a much higher rate than when the detuning lies between sidebands, and since a Raman transition has to occur before the repumping step provides on average 3 photons, this produces the increased fluorescence seen when the laser pair is tuned to the sidebands. The carrier (peak b) is visible for the same reason. The ion is still hot at this point, as although the carrier is providing no heating, the cooling is still only being provided by the repumping. As the Raman detuning moves towards the 1st red sideband, the sideband cooling mechanism cools the ion down to close to the ground state. At this point some fluorescence is still produced by off-resonant excitation of the carrier. This fluorescence is the peak a in the spectrum. The reason this part of the carrier gives more fluorescence than when the laser is tuned to resonance with the carrier is that when the ion is cold the motional matrix element is much larger than when the ion is hot, and this causes the Raman process to occur much faster, giving more fluorescence. The red sidebands are not seen, because the ion has little population outside the manifold $n = 0 \dots (k - 1)$ for detunings near the k th red sideband.

With this model in mind, we can make a rough consistency check using the data of figure 5.4 as an example. Using the information that peak b at -6.4 MHz is centred at the carrier frequency, together with the known Zeeman splitting (obtained from magnetic resonance) of 4.2 MHz, we deduce that the light shift is -2.2 MHz. The known detuning of 180 MHz (to the red of the single-photon resonances) then allows us to deduce that the pump Rabi frequency is 40 MHz, (*i.e.* $\Omega_2 = 2\pi \times 40$ MHz). We assume that the ion is cold when the Raman detuning is in the vicinity of the first few red sidebands (see the next section for confirming evidence of this), and then the fluorescence is dominated by off-resonant excitation of the carrier. Therefore the fluorescence rate for the data between -9 and -7 MHz on the horizontal axis of figure 5.4 may be modelled as given by equation 5.17, *i.e.* we take the predicted excited state population ρ_{33} and multiply by the decay rate $\Gamma = 1.32 \times 10^8 \text{ s}^{-1}$. The observed count rate can be interpreted since we know the overall collection/detection efficiency to be $0.75 \times 1.3 \times 10^{-3} = 9.75 \times 10^{-4}$. We find that the data suggests a probe Rabi frequency of $\Omega_1 = 0.15\Gamma = 2\pi \times 3.5$ MHz. This is consistent with the measured beam power and spot size.

Numerical study of main features

We carried out a simple numerical analysis in order to confirm that the above model can indeed explain the details of the observed fluorescence signals. In particular, the location of the sharp drop in fluorescence as δ increases, which we interpret as due to the ion temperature rising abruptly, gives information about the cooling and heating rates in the system. If the heating and cooling processes in the system were purely those associated with the expected two-photon resonance, as we implicitly assumed in our analysis such as

equation 5.21, then we would expect this abrupt change to take place at a value of detuning such that the cooling provided by off-resonant excitation of the first red sideband is just unable to compensate for the heating associated with the carrier and 1st blue sideband, for low but non-zero values of n . Therefore a rough estimate for the expected detuning δ at the sharp edge is given by

$$\eta^2 \hbar \omega_z \rho_{33}(\delta + \omega_z) \simeq \alpha E_R \rho_{33}(\delta) + \eta^2 \hbar \omega_z \rho_{33}(\delta - \omega_z) \quad (5.27)$$

$$\Rightarrow \rho_{33}(\delta + \omega_z) \simeq \rho_{33}(\delta) + \rho_{33}(\delta - \omega_z) \quad (5.28)$$

where we set $\alpha = 1$ and ignored the reduced saturation of the sidebands for simplicity. This is valid when $2\Omega_{\text{eff}}^2 \Gamma / \Gamma_1 \ll \max(R^2, (\delta - \Delta' + \omega_z)^2)$ because then removing the incorrectly assigned power broadening from the sideband excitations has little effect. If there were a further heating effect not included in this model, for example due to electric field noise or stray light, then the sharp edge would be closer to the 1st red sideband position. If such a heating rate were independent of the laser parameters, then the sharp edge would move towards the 1st red sideband position as the laser cooling rate is reduced, for example through reduction of the probe power. Note that there is no evidence of such a move in figures 5.4 and 5.5.

In principle equation 5.21 contains all the relevant physics to describe both the low temperature regime when the probe laser is tuned to the red of Δ' , and the high temperature regime when the probe laser is tuned to the blue of Δ' , as long as we understand ρ_{33} to be calculated without approximation (but still using a 3-level model of the atom), so that it includes the influence of the broad single-photon resonance at $\Delta_1 = 0$ as well as the narrow two-photon resonance at $\delta = \Delta'$. When the Raman detuning is blue, *i.e.* $\delta > \Delta'$, then the narrow resonance provides heating but the broad resonance provides cooling. However, calculation of the balance between these processes is very lengthy using equation 5.21 because the high values of n , and the large width (23 MHz) of the broad resonance, mean that hundreds of sidebands would need to be taken into account. We will therefore introduce a deliberately very simple model, which allows quick calculations and confirms the physical picture.

The simple model is to assume the probe laser drives a narrow resonance centred at $\delta = \Delta'$ while the pump laser drives the broad single-photon resonance and acts as a repumper. We estimate the net rate of change of energy for an ion in vibrational level n as

$$\frac{dE_n}{dt} = \sum_f \left(E_f - E_n + \alpha E_R + 6E_R n \frac{\omega_z}{\Delta} + \epsilon_1 \right) I_{fn} g(\delta - (E_f - E_n)/\hbar) + \epsilon_2, \quad (5.29)$$

where g is a lineshape function describing the narrow resonance, which we take to be Lorentzian of width γ . The first terms in the bracket are familiar from equation 5.21. ϵ_1 and ϵ_2 are extra heating terms introduced in case they are needed in order to obtain reasonable fits to the data. ϵ_1 is an energy representing heating associated with the probe laser driven processes (such as from the asymmetry of the two-photon resonance which a Lorentzian function does not account for); ϵ_2 represents heating processes not associated with the probe laser excitation. The term $6E_R n \omega_z / \Delta$ accounts for Doppler cooling associated with the repumping process. It is only significant at high n , and is estimated by a semiclassical argument as follows.

The excitation to $4P_{1/2}$ has a Lorentzian lineshape. For the high values of detuning Δ that we are concerned with, this has simply a $1/\Delta^2$ dependence. Consider an ion

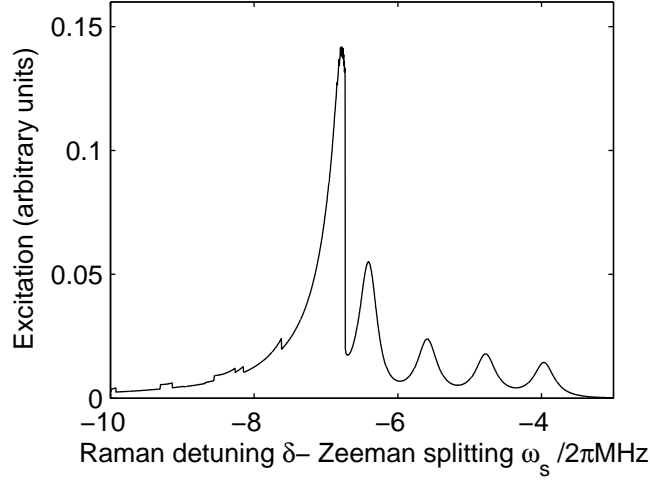


Figure 5.7: Excitation of ion resulting from the simple model of cooling presented in equation 5.29. For frequencies below the edge of the resonance the equilibrium n predicted is 0 for most of the wing of the resonance, rising sharply to ~ 250 at the edge of the resonance.

undergoing sinusoidal oscillations in the trap. When the speed is v the Doppler shift is kv and hence the scattering rate changes to $1/(\Delta + kv)^2$, therefore the proportions of scattering events which tend to cool or heat are in the ratio $(\Delta - kv)^2/(\Delta + kv)^2$. The proportions are therefore $(1/2) \mp kv/\Delta$ for $|kv| \ll |\Delta|$. Each photon scattered results in a kinetic energy change approximately $dE = v\hbar k$. Hence the average motional energy change per scattering event is

$$\langle dE \rangle = \frac{2\hbar k^2 \langle v^2 \rangle}{\Delta}. \quad (5.30)$$

If the sinusoidal oscillations have velocity amplitude v_0 , then $\langle v^2 \rangle = v_0^2/2$ and $(1/2)mv_0^2 \simeq n\hbar\omega$, hence $\langle dE \rangle = 4E_R n \omega_z / \Delta$. We multiply this by 3 in equation 5.29 to account for the fact that on average 3 scattering events are required to repump the ion to level 1 (*cf.* figure 5.2), and then divide by 2 since the laser beams are propagating at 60° to the trap axis. Note that we are ignoring the radial degrees of freedom, as we have done throughout this chapter.

For each value of δ we find an approximate equilibrium value for n by solving³ $dE_n/dt = 0$. Then the fluorescence rate is calculated as $\sum_f I_{fn} g(\delta - (f - n)\omega_z)$. We do not attempt to get an absolute estimate for the expected count rate, but we already commented above that the observed count rates are roughly consistent with expectations.

Figure 5.7 shows the predicted fluorescence as a function of δ , for parameters chosen to match the experimental conditions of figure 5.4: $\Delta/2\pi = 180$ MHz, a Zeeman splitting of 4.2 MHz and light shift of -2.9 MHz. The other parameters were adjusted to obtain the best fit to the data: Lorentzian linewidth $\gamma/2\pi = 300$ kHz, heating parameters $\epsilon_1 = 0$, $\epsilon_2 = 0.007\gamma\hbar\omega_z$. Note that in this and other examples, it was found that ϵ_1 was not needed but a non-zero value for ϵ_2 was needed in order to get a reasonable match with the experimental observations. This suggests there may be a small extraneous heating process in the experiment. However an analysis using a non-Lorentzian lineshape function would

³This is done by searching for the value where dE_n/dt changes sign.

be useful to check whether the conclusion is sensitive to this.

The equilibrium value of n in the model is found to be small for red detunings, as expected, *cf.* figure 5.3. At the carrier position it is around a few hundred, rising to 5000 over the range of detunings calculated. It goes through local minima at the carrier and blue sideband positions; this has the effect of enhancing the visibility of the observed blue sideband resonances. This behaviour of n is owing, at least in part, to the fact that when the laser-driven processes are faster the heating term ϵ_2 is proportionately less important.

5.3.2 Temperature measurements

We used the Raman laser beam pair in the comparison of sidebands method described in section 5.1.2 to measure the temperature of the ion. The final temperature produced by continuous cooling was thus studied as a function of probe detuning.

To get the most accurate measurement at low temperatures, the length of pulse used for the Raman sideband pulses should be about equal to a π time, giving the largest possible signal. The typical sequence of experiments undertaken to get a temperature measurement was as follows. Firstly, a scan to observe the fluorescence as a function of probe detuning was taken. The probe detuning was then set to where the first red sideband was inferred to be (*i.e.* ω_z to the red of the carrier). A sideband spectrum was then taken using the Raman beams. This allowed us to determine the frequency offsets needed for the Raman laser AOMs to excite the red and blue sidebands resonantly. We then tuned the Raman laser frequencies to the blue sideband, and looked at the excitation of the ion as a function of the sideband excitation pulse length. This allowed us to measure the π time on the 1st sideband, which is the time which gives the most accurate temperature measurement for low temperatures. Finally, an experimental sequence consisting of ‘‘Doppler cool, continuous Raman cool, optical pump to $|\downarrow\rangle$, Raman π pulse on sideband, measure spin state’’ was implemented. We thus obtained the height of the sidebands (*i.e.* our temperature diagnostics) as a function of a parameter of our cooling technique (*e.g.* detuning δ of the 397 probe laser). The actual sequence was first to find the blue sideband height as a function of δ , then find the red sideband height as a function of δ , and then combine the data afterwards. We also took a continuous fluorescence scan so that we could compare the features of this spectrum with the temperature diagnostic information.

Figure 5.8 shows the result of making one of these sets of measurements. The upper part of the figure shows the ratio of the measured sideband heights (above the background set by the shelving) as a function of the probe detuning. The lower part of the figure shows a fluorescence spectrum taken shortly after, over the same probe detuning range. The fluorescence scan is broadly similar to that shown in figure 5.4. This scan was taken with the pump beam σ^+ polarised and with the pump detuning $\sim 2\pi \cdot 140$ MHz. From this detuning, and the light shift, which we obtain from the fluorescence spectrum, we infer a Rabi frequency for the pump beam of $\Omega_2 = 2\pi \cdot 32$ MHz. The probe power was $15 \mu\text{W}$.

Note that the detuning which gives the coolest ion as indicated by the sideband ratio (upper figure) coincides with the first red sideband location on the fluorescence spectrum (lower figure). The sideband ratio r at this point is equal to 0.28, implying $\bar{n}_z = 0.4$. As the probe beam detuning is decreased, \bar{n} increases rapidly, reaching ~ 1.2 when the probe is detuned 250 kHz below the first red sideband and slowly increasing from this point to ~ 1.4 at a detuning corresponding to the 2nd red sideband.

This behaviour is as expected, as tuning to the second red sideband will still cool the ion, at least if it has population in motional states $n \geq 2$. Note however that tuning to

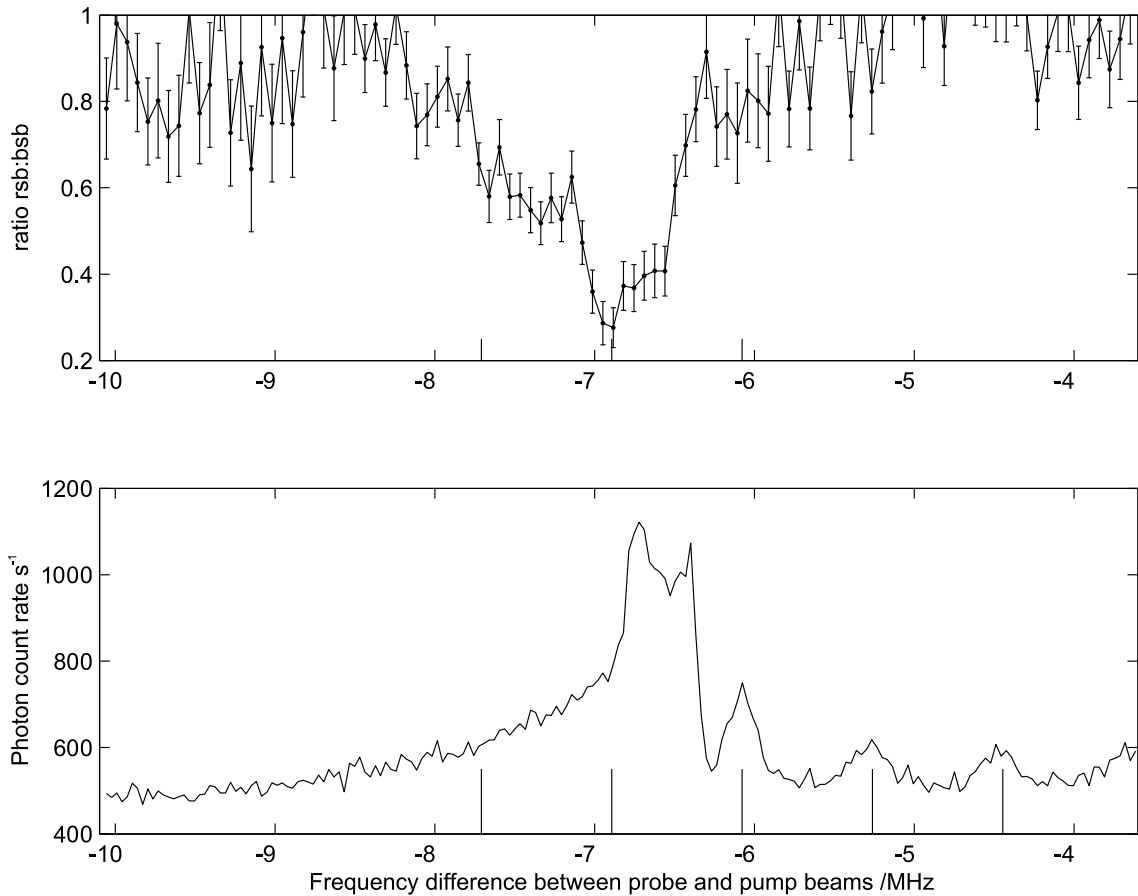


Figure 5.8: Ratio of sidebands as a function of probe detuning. Underneath is shown a fluorescence spectrum taken under the same conditions. The position of the red sidebands can be inferred from the positions of the resonances due to the carrier and first two blue sidebands, and are marked on the graph. The detuning at which the ion is coldest corresponds with the detuning of the first red sideband, and at this detuning $\bar{n}_z=0.4$. The probe power was $15 \mu\text{W}$.

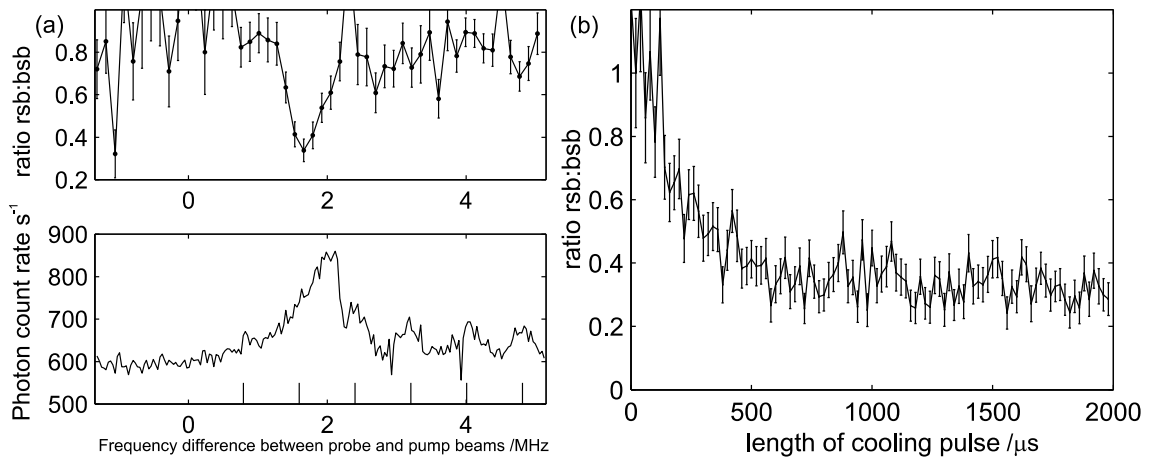


Figure 5.9: (a) Fluorescence spectrum and associated sideband ratio. The pump power and detuning are similar figure 5.8. The pump polarisation is σ^- not σ^+ and the probe power is approximately halved to $7 \mu\text{W}$. (b) Sideband ratio as a function of the time spent in continuous cooling, for the same conditions. (Probe tuned to first red sideband). $\bar{n}_z \sim 0.5$ reached after ~ 0.6 ms.

the second red sideband is not expected to produce an ion in a thermal state, because population in the $n = 1$ motional state does not have a second red sideband. This means that using the ratio of sideband heights to assign a temperature to the ion is not valid. The fact that the fluorescence spectrum has no resonance at the detuning corresponding to the 2nd red sideband is evidence that there is little population in $n \geq 2$.

Now consider probe detunings of higher frequency than the first red sideband. In the fluorescence spectrum there is an additional resonance not seen in the earlier fluorescence scan. This resonance in the fluorescence has its highest point at a probe detuning 170 kHz to the blue of the first red sideband. Putting aside the cause of this resonance until later, it can be seen that the ion remains cool at detunings corresponding to this resonance, with mean excitation values of $\bar{n}_z = 0.6-0.7$. As the detuning changes to take the ion over the edge of the main peak, the ion heats up, over the course of a detuning change of 200 kHz.

We do not currently have a model to account for the presence of this extra resonance. The resonance was present in all scans taken for a range of probe and pump powers and detunings. These all used a σ^+ polarised pump beam. When the polarisation of the pump beam was changed to σ^- however, the resonance was not present. One possibility is that the resonance is caused by Raman transitions driven by other polarisation components present in the pump and/or probe beams. By changing the polarisation of the pump beam, the detuning of the Raman resonance changes by $\sim 2 \times 4.3$ MHz, and so whatever resonance was being excited is now far from resonance.

Figure 5.9a shows a ratio of sidebands plot and fluorescence spectrum with the pump beam σ^- polarised. The pump power and detuning are similar to that in figure 5.8, and produce a similar light shift. The probe power is smaller by approximately a factor two being $7 \mu\text{W}$. The data implies $\bar{n}_z = 0.5$ when the probe is tuned to the first red sideband. For detunings to the red of this the cooling is less efficient than in the case with twice the probe power to the extent that a resonance is visible in the fluorescence at the position of the second red sideband.

The temperature measurements in figures 5.9a and 5.8 were taken after 1 ms of continuous sideband cooling. To check that this is enough time the temperature was measured as a function of the length of the cooling pulse. The probe laser was set to the first red sideband and the red and blue sidebands recorded as a function of the length of the cooling pulse. The ratio of the two can be seen in figure 5.9b. For these parameters, the ion reaches a final excitation of $\bar{n}_z = 0.5$, after a time of ~ 0.6 ms. Since this was measured with the lower probe power, 1 ms is also more than sufficient for the higher probe power scan.

The reduction of probe power had little effect on the measured temperature and in view of equation 5.24, this suggests that we are in the regime where the width of the two photon resonance, f given by equation 5.20, is dominated by the scattering caused by the pump beam. In this regime the change in probe power would still affect the cooling rate, with a halving of probe power reducing the cooling rate by a factor 2 (equation 5.26). This would also lead to the approximate halving of the number of photons detected in the fluorescence spectrum at the first red sideband position which is observed as the rate at which the carrier Raman transition causes population transfer is halved.

The temperatures that we observe using the continuous sideband cooling method give minimum excitation around $\bar{n}_z \sim 0.5$ for the parameters we have tried. From the fluorescence scans that are shown the linewidth of the two photon cooling process is small compared with the trap frequency and so from equation 5.24 we would expect $\bar{n}_z \ll 1$.

To be more quantitative, we can compare the information given in figure 5.8 with equation 5.24. The light shift Δ' and trap frequency ω_z are measured quantities. The carrier and blue sideband resonances should have a width similar to the width of the bright resonance, so if we take $f \sim 2\pi \cdot 0.2$ MHz we get a prediction of $\bar{n}_z \sim 0.05$. Even if the width is as much as $f = \omega_z/2$ this would result in $\bar{n}_z = 0.2$ whereas the value $\bar{n}_z = 0.4$ is measured.

The fact that we do not reach the predicted low temperature is likely to be due to heating of the ion by processes other than those shown in figure 5.1b. There are two types of heating process which may be present: a process associated with laser excitation, such as stray light or effects not accounted for in the 3-level model of the ion, and a process which is present even when all the lasers are off, such as fluctuating electric fields.⁴

We studied the heating rate of the second kind (electric field noise) by looking at the sideband ratio after inserting a variable delay between the end of cooling and the sideband driving pulse we use as our temperature diagnostic. When this experiment was performed the mean vibrational excitation with only the small delay due to the LCU (section 2.3) was $\bar{n}_z = 0.8(2)$. After a delay of 10 ms there was only a small increase in motional energy, with $\bar{n}_z = 1.0(2)$. This gives $d\bar{n}_z/dt = 0.02(3)/\text{ms}$. This is very low and implies that the temperature attained in sideband cooling is not being limited by heating due to processes external to the cooling.

We therefore made a careful study of the possibility of stray light reaching the ion, checking AOM extinction ratios and so on. We do not to date have a satisfactory explanation of the observed cooling limit. Excitation to the 2nd Zeeman sublevel of $4P_{1/2}$

⁴The rate of excitation from $n = 0$ to $n = 1$ ($\Gamma_{0 \rightarrow 1}$) is proportional to the spectral density of the component of the electric field along the trap axis at the trap frequency, and inversely proportional to trap frequency[57]. There are many mechanisms which produce such fluctuating fields, such as voltage noise on the end cap electrodes, or external electric fields. Two mechanisms usually studied are heating due to fields produced by thermal noise in the trap electrodes, and heating due to fluctuating patch potentials on the surface of the electrodes. Both effects decrease as the size of the trap is increased (for thermal noise $\Gamma_{0 \rightarrow 1} \propto d^{-2}$, for patch potentials $\Gamma_{0 \rightarrow 1} \propto d^{-4}$).

(*i.e.* outside the 3-level model) will interrupt the cooling and cause some heating but this is not expected to be large enough to explain the observations.

5.4 ‘EIT’ cooling

As we saw in our analysis of cooling (equation 5.24), the final temperature reached depends on the light shift and the width of the cooling resonance, whereas the cooling time constant depends only on the resonance width. The experiments in the previous section used red detuned lasers. By using blue detunings, and matching light shift to trap frequency so that we are in Morigi’s EIT cooling regime, for a given theoretical final temperature we can get a larger cooling rate.

The steady-state is obtained when heating and cooling processes are equal. This is what enabled us to reach a steady-state temperature in the experiments set out in section 5.3 even when the Raman process was set for heating, as the cooling provided by the single photon absorption balances it at large values of n_z . This process does not occur when the cooling beams are blue detuned. Then the single photon absorption process heats the ion on average for all n_z . This means that it is not possible to obtain steady-state fluorescence spectra outside a small range of Raman detuning near the optimal cooling point.

In the continuous cooling above, the probe/pump beam detuning was set relative to the Doppler beam detuning by using all three AOMs in -1st order, giving the pump/probe laser beams a frequency ~ 115 MHz lower than that of the Doppler cooling beam. To perform cooling with a blue detuned Raman transition, the experimental setup has to be changed slightly, so that the Doppler cooling beam now has a lower frequency than the Raman pump/probe beams. This was done by using the pump/probe AOMs in 1st order. The frequency of the pump/probe beams can then be either ~ 285 MHz or ~ 115 MHz higher than the Doppler beam, depending on which order of the Doppler AOM is used. To reduce the realignment needed when switching between AOM orders we turn the AOMs round, so that the 1st order beam travels along the same path as the -1st order beam did.

In figure 5.8 the pump power and detuning (of ~ -140 MHz) combined to give a light shift of $\sim -2\pi \cdot 1.8$ MHz. To produce a (positive) light shift equal to the trap frequency, we could reduce the intensity of the pump beam, increase the magnitude of the detuning or a combination of the two. We have two positive detunings available to us with our setup, ~ 90 MHz or ~ 260 MHz, of which we choose the second. This is because to match the light shift to the trap frequency with a detuning of 90 MHz would require a low pump Rabi frequency of $2\pi \cdot 17$ MHz ($=0.8\Gamma$), and correspondingly lower probe Rabi frequency. To obtain a detuning of 260 MHz requires that the Doppler AOM remains in -1st order.

Figure 5.10 shows two sets of sideband ratio measurements. The pump power in these cases is not set correctly, as the probe frequency which results in the coolest ion implies $\delta/2\pi = -0.3$ MHz and a light shift of $2\pi \cdot 0.5$ MHz rather than the $2\pi \cdot 0.8$ MHz it would need to match the trap frequency. Nevertheless good cooling is still observed in both cases, as the EIT condition does not have to be met for cooling, it simply offers a lower \bar{n} by suppressing one of the heating mechanisms. (In fact equation 5.24 implies even better cooling (for a given feature width f) at light shifts greater than ω_z , where both heating processes are partially suppressed.) The values of \bar{n}_z reached in the two cases are approximately the same, $\bar{n}_z=0.31$ and 0.29 . The difference between the two cases is in the cooling time (2 ms in the first, 3 ms in the second) and probe power (halved from $8 \mu\text{W}$ in the first to $4 \mu\text{W}$ in the second).

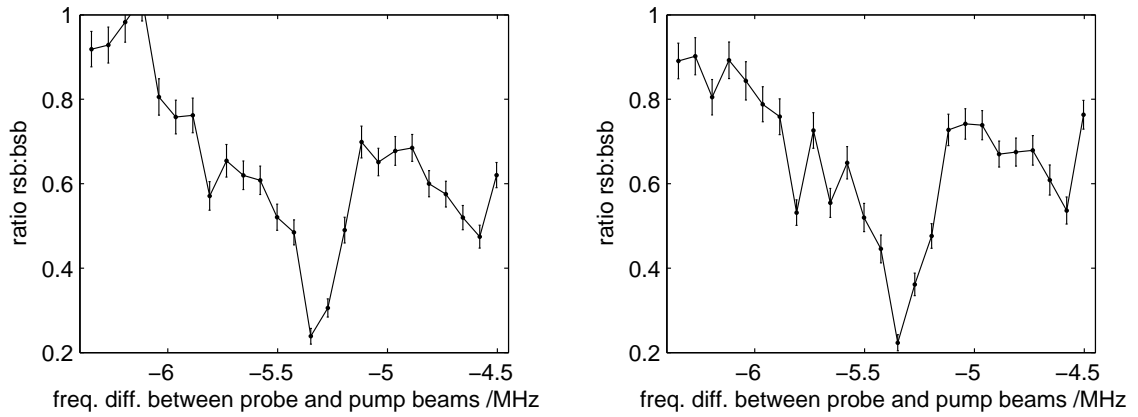


Figure 5.10: Two sets of sideband ratio plots for continuous cooling set with positive detunings (EIT cooling). The frequency corresponding to the lowest temperature, and thus the position of the first red sideband, is -5.3 MHz and since the Zeeman splitting was 5.0 MHz this corresponds to $\delta/2\pi = -0.3$ MHz. The EIT cooling time in (a) is 3 ms. In (b) the probe power was halved and the cooling time increased to 4 ms.

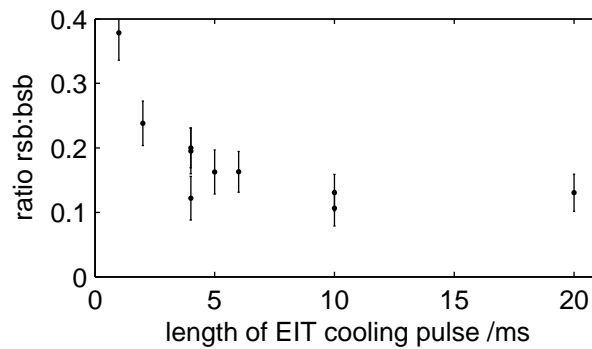


Figure 5.11: Ratio of sidebands as a function of the length of the cooling pulse. The conditions are as in figure 5.10b, with the probe detuning set to -5.3 MHz, which gave the coldest ion in the previous figure. After 10 ms the limiting temperature is reached, with $\bar{n}_z = 0.14$

Figure 5.11 gives the variation in ratio as a function of cooling time for the same conditions as in figure 5.10b with the probe tuned to the coolest point. The cooling rate here is slow, with \bar{n} dropping from 0.31 after 2 ms to 0.14 after 10 ms, slower than for red-detuned cooling. This is only partially explained by the reduced probe power.

5.5 Pulsed sideband cooling

Using the continuous cooling methods described above we are able to achieve near ground state cooling. With cooling on the red side we observed values of \bar{n} around the 0.4 level, while with blue detuned ‘EIT’ like cooling we reached $\bar{n}=0.15$. When $\bar{n}=0.15$ the ion occupies the ground state with over 85% probability. The third sideband cooling method we explored was pulsed sideband cooling.

We use the Raman beams to perform a further round of sideband cooling, after our continuous cooling, but this time not in a continuous fashion, but in a pulsed manner. Cooling with Raman transitions in this way is closest to the model of sideband cooling shown in figure 5.1. A pulse on the red sideband transfers population from $|\downarrow, n\rangle \rightarrow |\uparrow, n-1\rangle$. The Raman lasers are then turned off, and the σ^- pump laser that was used during the continuous cool optically pumps the ion back to the $|\downarrow\rangle$ state. This cycle is then repeated as required. We do not operate pulsed sideband cooling directly on a Doppler cooled ion in our trap because after only Doppler cooling \bar{n}_z is too high. As each Raman pulse/repump cycle can remove at most one quantum of vibrational energy (at least if we are tuned to the first red sideband), it would require a large number of cycles to cool to the ground state. More importantly, the Rabi frequency of a first red sideband transition depends strongly on the motional state of the ion. In particular, although the frequency increases at first as the motional quantum number of the ion increases, for our trap strength it reaches a maximum for n in the early twenties before falling again, with the frequency for $n = 94 \rightarrow n = 93$ only 1% that of the $n = 1 \rightarrow n = 0$ transition. This low Rabi frequency would cause population with $n \geq 94$ to become trapped in this motional state, unable to make the transition to the lower state. For an ion at twice the Doppler temperature the probability of being in $n \geq 94$ is $\sim 2.5\%$.

This means that we have to apply one of our other sideband cooling techniques before pulsed sideband cooling. The final temperature is determined by the Rabi frequency with which the sideband is driven, which determines the likelihood of a carrier or 1st blue sideband excitation.

We determine the optimum time for the cooling pulse experimentally. By looking at excitation on the 1st blue sideband, which will oscillate at the same frequency as the 1st red sideband, but with greater amplitude, we can determine the ‘ π ’ time for our thermal state.

Figure 5.12a shows a sideband spectrum which was taken after the ion was cooled by 1 ms of red-detuned continuous sideband cooling. The spectrum is obtained by measuring the shelving obtained after a $12 \mu\text{s}$ pulse from the Raman lasers. The frequency of the parallel Raman beam is varied, with 500 scans taken per data point. From the sideband height, we see the mean excitation of the ion is $\bar{n}_z=0.5$. Figure 5.13 (dashed line) shows the result of observing Rabi flopping on the 1st sideband for an ion under the same cooling conditions. It can be seen that maximum population transfer from the initial state occurs at a time of around $13 \mu\text{s}$. We can then use this time for our pulsed sideband cooling

Five rounds of sideband cooling were performed, each consisting of a population transfer Raman pulse, and then a pulse from the 397 pump beam to reinitialise the ion’s

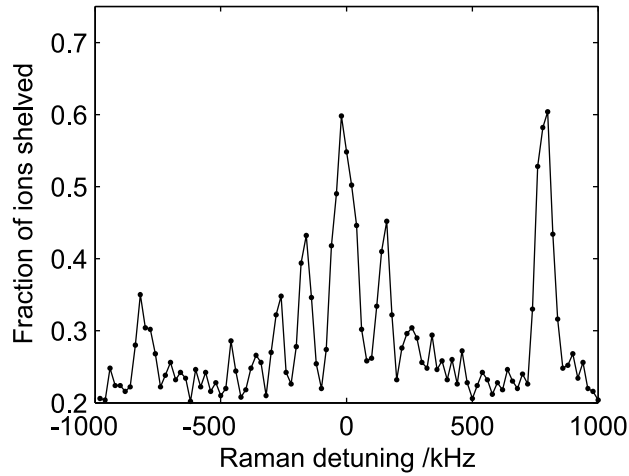


Figure 5.12: Raman spectrum obtained after 1 ms of continuous cooling. The carrier and 1st red and 1st blue sidebands can be seen. The relative heights of the red and blue sidebands imply $\bar{n}_z=0.5$. The Rabi frequency for excitation on the carrier is much higher than that for driving the sidebands, hence the large number of peaks due to carrier excitation. Solid line joins data points.

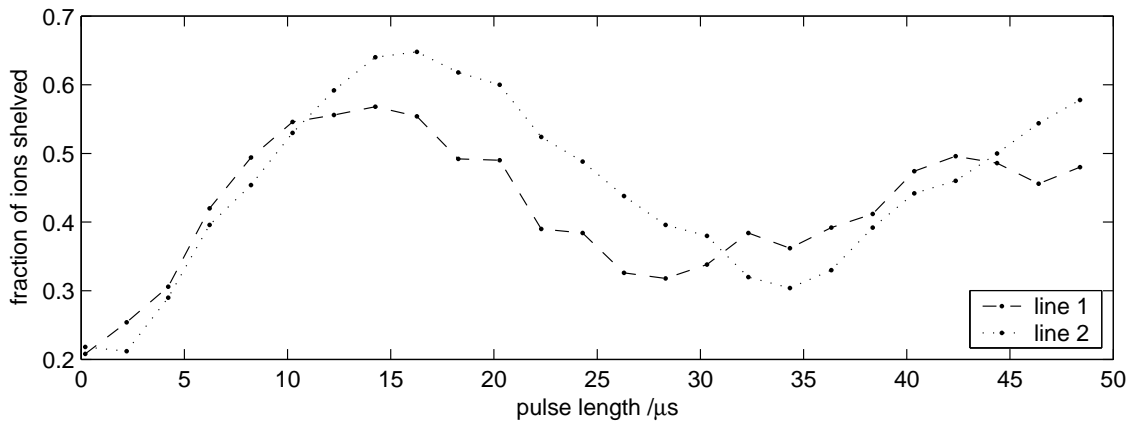


Figure 5.13: Sideband scans. Rabi flopping on the 1st blue sideband is shown for two different cooling regimes. For line one the sideband pulse occurs after 1 ms of continuous red-detuned sideband cooling. For line two the ion was cooled with 1 ms of continuous cooling, followed by $5\times$ (red sideband pulse then repump pulse). Each sideband pulse lasted $13\ \mu\text{s}$. The amplitude of the Rabi flopping is greater, and the time for maximum transfer longer, after the additional cooling, due to the ion being cooler.

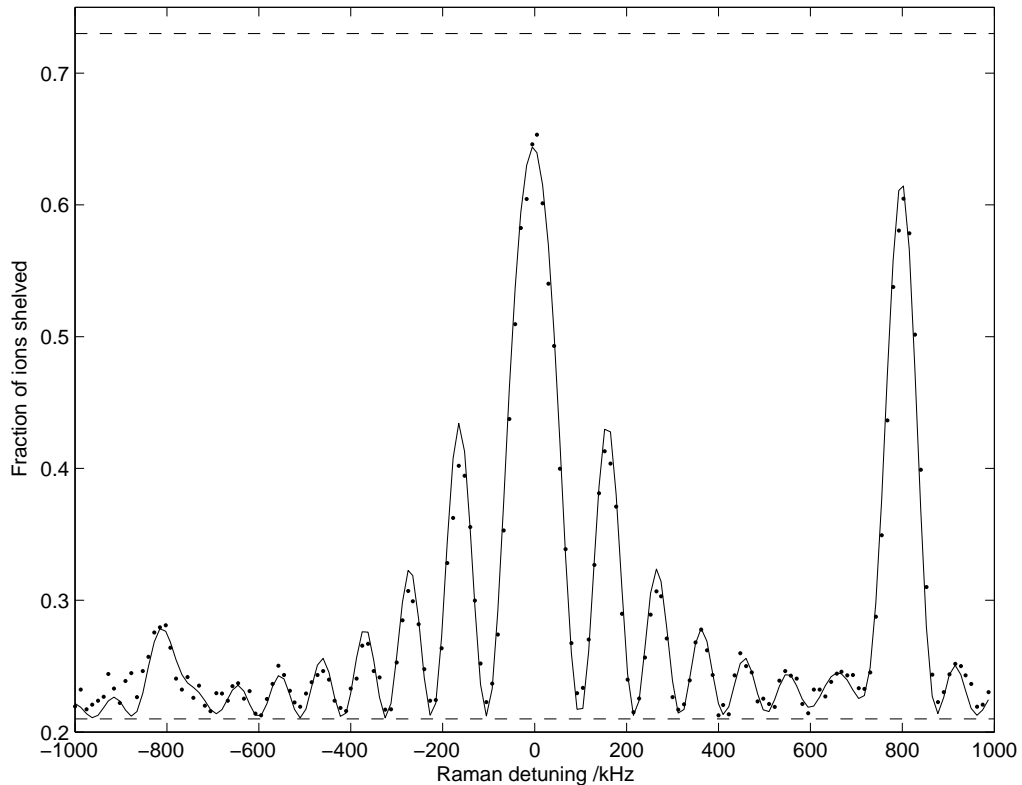


Figure 5.14: Raman spectrum after 5 rounds of pulsed sideband cooling (see text for details). The solid line is a fit to the data. The fit gives an effective Rabi frequency of $2\pi \cdot 144$ kHz, and an $\bar{n}_z=0.17$. The dashed lines indicate the shelving levels obtained from the fit, which agree with the measured values.

internal state. After this, a new Rabi flopping scan was performed, and is shown in figure 5.13 (dotted line). The ion is visibly cooler for this scan as can be seen by the increased maximum shelving, and the decreased oscillation frequency. The timing of the sideband cooling pulses was then changed to reflect this decreased frequency and sideband cooling with pulses of length 13,13,13,15,16 μ s was performed. A high resolution sideband spectrum with a large number of repetitions per point (4000) was then taken, which is shown in figure 5.12b. This also shows a fit to the spectrum. The fit parameters are a thermal distribution of vibrational states with $\bar{n}_z=0.17$ and a carrier effective Rabi frequency of $2\pi \cdot 144$ kHz. The fit has the pulse time set to 11.4 μ s, rather than the 12 μ s pulse length produced by the LCU. This is required to get the correct spacing of the fringes in the excitation pattern of the carrier. Higher effective Rabi frequencies are possible but not used so as to keep carrier excitation at the sideband frequencies to a low level.

5.5.1 Conclusions

In this chapter we have presented a simple theoretic model of continuous sideband cooling of a single ion and experimentally implemented continuous cooling with both red and blue detuned lasers, as well as additional cooling using pulsed Raman sideband excitation.

The theoretical model simply considers a rate equation in which the scattering processes for all possible motional and spin state changes are summed. This is a standard

simple way to treat cooling by single photon transitions, but here it was applied in the case of two-photon effects in a three-level system. This may be understood as a dressed atom approach, in which the atom plus pump laser field form a single system which is then excited by the probe laser. The model gives the same prediction for steady-state temperature under EIT cooling in the Lamb-Dicke limit as the more thorough analysis by Morigi [50], which suggests it gives valid quantitative as well as qualitative insights. This permits us to understand quickly and easily the main issues affecting the cooling rate and final temperature.

Experimentally, we have studied in some detail the fluorescence emitted by an ion being continuously Raman cooled as a function of the probe detuning for red-detuned probe/pump beams. By measuring the light shift induced by the pump laser we are able to unambiguously identify the feature in these fluorescence spectra which corresponds to the carrier transition, and we are able to interpret the form of the spectra.

Using red-detuned continuous cooling, the minimum excitation achieved was $\bar{n}_z=0.4$, which is greater than we would have expected, and we are not able to explain the reason for this. This excitation places the ion within the Lamb-Dicke regime, and well placed to be further cooled using pulsed sideband cooling. Using blue-detuned cooling we have achieved lower excitations, of around $\bar{n}_z=0.14$. While this is colder than the red-detuned method, the red-detuned cooling method is more simple to use in practice. Observing the fluorescence spectrum allows the probe detuning to be easily set, by noting the values of detuning at which the carrier and blue sidebands are found. The method of setting the probe frequency for blue-detuned cooling, as set out in section 5.4 is much more involved. In addition, when experiments are being performed the accidental use of the blue-detuned probe or pump beams on the ion can result in the ion being lost due to it Doppler heating out of the trap. For these reasons we currently only use the red-detuned method. For the trap strength used in these experiments the Doppler temperature for cooling on the 397 transition corresponds to $\bar{n}_z=13$. These results are the first sub-Doppler cooling we have performed in our laboratory.

We have also implemented pulsed Raman sideband cooling to further reduce vibrational excitation after red-detuned continuous cooling. In section 5.5 we presented cooling from $\bar{n}_z=0.5$ to $\bar{n}_z=0.17$ using 5 sideband cooling pulses. Pulsed cooling should be able to produce much lower temperature than this however, and recent progress within the group has demonstrated $\bar{n}_z = 0.02 \pm 0.01$.

Finally, we have been able to use an ion cooled using these methods to make a measurement of the heating rate of an ion in our trap. We measured a heating rate of $d\bar{n}_z/dt = 0.02(3)/\text{ms}$. This rate is low (compared with those measured in [57]), particularly taking into account the much lower trap frequency. This is probably due to the large size of our trap compared with those in use at NIST. The rate is similar to those measured in Innsbruck[54] using a trap with similar, relatively large, distances from the ion to the electrode surfaces.

Chapter 6

Cooling two ions

The previous chapter presented experiments in which a single ion was cooled down to temperatures corresponding to a mean vibrational quantum number $\bar{n}_z \sim 0.15$ for the axial mode. A single ion cooled to the ground state of one of its motional modes can be used as a two qubit system, via the internal and motional state, and allowing very basic information processing to be performed. Using the motional state to store several qubits is not scalable to many qubits, so if larger numbers of qubits are to be realised we require more ions. This chapter discusses the dynamics of a two ion system and the measurement of its temperature. We then describe our preliminary work on the cooling of two ions. We make use of both the continuous sideband cooling method (for red detuned pump/probe) and pulsed sideband cooling.

6.1 Dynamics of two trapped ions

We want to study two ions which are in a trapping regime such that they form a crystal lying along the z axis of the trap.

We begin by looking at the classical behaviour of such a crystal, specifically the two motional modes of the crystal along the z axis. These two modes can then be quantised and their quantum behaviour studied. To determine the temperature of a single, thermal, ion a simple method exists. For a two-ion crystal the determination is less straightforward, and this is discussed.

6.1.1 Normal modes

Consider the case that the radial confinement is such that the ions lie along the z axis, and we do not need to consider motion of the ions in the radial direction.

The total energy of such a two ion system is simply equal to the energies of two uncoupled trapped ions plus the energy of their Coulomb repulsion:

$$E = \frac{p_1^2}{2m} + \frac{p_2^2}{2m} + \frac{1}{2}m\omega_z^2 z_1^2 + \frac{1}{2}m\omega_z^2 z_2^2 + \frac{e^2}{4\pi\epsilon_0|z_2 - z_1|}. \quad (6.1)$$

Defining the centre of mass and stretch coordinates and momenta as

$$z_c = \frac{1}{2}(z_1 + z_2), \quad z_s = z_2 - z_1, \quad p_c = p_1 + p_2, \quad p_s = \frac{1}{2}(p_2 - p_1) \quad (6.2)$$

and then substituting them into the energy equation we get

$$E = \frac{p_c^2}{2M} + \frac{p_s^2}{2\mu} + \frac{1}{2}M\omega_z^2 z_c^2 + \frac{1}{2}\mu\omega_z^2 z_s^2 + \frac{e^2}{4\pi\epsilon_0 z_s}, \quad (6.3)$$

where $M = 2m$ and $\mu = m/2$.

To find the separation z_{s0} when the ions are at rest we set the partial derivative of the energy wrt z_s equal to zero:

$$\left(\frac{\partial E}{\partial z_s}\right)_{z_s=z_{s0}} \Rightarrow z_{s0} = \left(\frac{e^2}{2\pi\epsilon_0 m\omega_z}\right)^{\frac{1}{3}}. \quad (6.4)$$

Expanding the Coulomb energy about $z_s = z_{s0}$ gives

$$E \simeq \frac{p_c^2}{2M} + \frac{p_s^2}{2\mu} + \frac{1}{2}M\omega_z^2 z_c^2 + \frac{3}{2}\mu\omega_z^2 (z_s - z_{s0})^2 + \frac{3}{2}\mu z_{s0} \quad (6.5)$$

Thus we have cast the energy in the form of a sum of two independent harmonic modes, with frequencies ω_z and $\sqrt{3}\omega_z$. The lower frequency mode is the motion of the centre of mass (COM) of the ions where the two ions move in phase with each other, while the higher frequency motion, known as the stretch or breathing mode, has the two ions moving in anti-phase, so that their separation oscillates.

6.1.2 Quantisation of the motion

The two normal modes may be quantised in the usual way, by replacing positions and momenta with the appropriate operators. z_c, z_s, p_c and p_s , (now understood to be operators) which are linear combinations of the single particle positions and momenta, obey the canonical commutation relations for position and momenta, and so our motional Hamiltonian is that of a pair of harmonic oscillators. We denote the creation(annihilation) operators for the COM mode as $a_c^\dagger(a_c)$, and those for the stretch mode as $a_s^\dagger(a_s)$.

We can now write down the complete Hamiltonian for interaction of the two ions with radiation. We do not individually address the ions in our experiment and assume here both couple equally to the radiation. $H = H_0 + H_I$ where

$$H_0 = \frac{1}{2}\hbar\omega_s(\sigma_{z1} + \sigma_{z2}) + \hbar\omega_z(a_c^\dagger a_c + \sqrt{3}a_s^\dagger a_s), \quad (6.6)$$

$$H_I = \hbar\Omega_0(\sigma_1^+ + \sigma_1^-) \cos(kz_1 - \omega t) + \hbar\Omega_0(\sigma_2^+ + \sigma_2^-) \cos(kz_2 - \omega t). \quad (6.7)$$

As in chapter 4 we use a Raman transition to drive population between the two internal states, for which $\Omega_0 \equiv \Omega_{\text{eff}}$, $k \equiv \Delta k$, $\omega \equiv \omega_1 - \omega_2$, and ω_s is modified to take into account the light shifts caused by the two Raman beams. For simplicity we have omitted phase factors from the oscillating terms in H_I as we are only interested in the behaviour of the system under a single pulse for measurement of temperature, for which these laser phases are unimportant.

To solve Schrödinger's equation we follow the same procedure as for a single ion, as follows. First we express the positions in terms of creation and destruction operators:

$$kz_1 = \eta_c(a_c^\dagger + a_c) - \eta_s(a_s^\dagger + a_s) - c \quad (6.8)$$

$$kz_2 = \eta_c(a_c^\dagger + a_c) + \eta_s(a_s^\dagger + a_s) + c \quad (6.9)$$

Populations	1st red sideband	1st blue sideband
$ \langle \downarrow\downarrow \Psi \rangle ^2$	$\left(1 - \frac{n}{2n-1}[1 - \cos(g_r \Omega t/2)]\right)^2$	$\left(1 - \frac{n+1}{2n+3}[1 - \cos(g_b \Omega t/2)]\right)^2$
$ \langle \downarrow\uparrow \Psi \rangle ^2, \langle \uparrow\downarrow \Psi \rangle ^2$	$\frac{n}{2(2n-1)} \sin^2(g_r \Omega t/2)$	$\frac{n+1}{2(2n+3)} \sin^2(g_b \Omega t/2)$
$ \langle \uparrow\uparrow \Psi \rangle ^2$	$\frac{n(n-1)}{(2n-1)^2} [1 - \cos(g_r \Omega t/2)]^2$	$\frac{(n+1)(n+2)}{(2n+3)^2} [1 - \cos(g_b \Omega t/2)]^2$

Table 6.1: Populations in the four different internal states of the two ion system after resonant excitation on one of the first red or blue sidebands of the state $|\downarrow\downarrow n\rangle$ by a single pulse of length t . $g_r = \eta_m \sqrt{2(2n-1)}$ and $g_b = \eta_m \sqrt{2(2n+3)}$ where η_m equals either η_c or η_s .

where the two ion Lamb-Dicke parameters η_c and η_s are defined in terms of the single ion parameter η : $\eta_c = \eta/\sqrt{2}$ and $\eta_s = \eta/\sqrt{2\sqrt{3}}$. The constant $c = \frac{1}{2}kz_{s0}$, which arises from the separation of the ions, contributes only an additional phase factor and so will be dropped.

We next transform into the interaction picture and move straight to the case of a weakly driven system ($\Omega \ll \omega_z$) in the Lamb-Dicke regime. If the Raman laser beams are tuned to one of the first red sidebands then

$$H_I' = \frac{1}{2}i\hbar\eta\Omega_0(\pm a\sigma_1^+ + a\sigma_2^+) + \text{h.c.} \quad (6.10)$$

where η and a are as appropriate for the mode (COM or stretch) driven and if it is the centre of mass mode we take the plus sign, stretch mode the minus sign. Similarly for the first blue sideband

$$H_I' = \frac{1}{2}i\hbar\eta\Omega_0(\pm a^\dagger\sigma_1^+ + a^\dagger\sigma_2^+) + \text{h.c.} \quad (6.11)$$

These Hamiltonians cause the two trapped ions to decouple into a series of independent four-level systems. For the red sideband the four states are $\{|\downarrow\downarrow n\rangle, |\downarrow\uparrow n-1\rangle, |\uparrow\downarrow n-1\rangle, |\uparrow\uparrow n-2\rangle\}$ and for the blue sideband $\{|\downarrow\downarrow n\rangle, |\downarrow\uparrow n+1\rangle, |\uparrow\downarrow n+1\rangle, |\uparrow\uparrow n+2\rangle\}$.

We are interested in the populations in the four internal states after a system beginning in the $|\downarrow\downarrow\rangle$ state is driven by a single pulse. By finding the eigenvectors the Hamiltonian can be diagonalised and the solution found. Table 6.1 shows the populations of the four internal states after the state $|\downarrow\downarrow n\rangle$ is driven on one of these sidebands, which were calculated by J. Home[58, 59].

6.1.3 Determining the qubit state

We use the same method of readout for the two ions as with a single ion, that of shelving followed by fluorescence detection. For two ions there are four possible combinations of fluorescing/non-fluorescing. Using the PMT we cannot distinguish between the two ions, so when only one ion is fluorescing we cannot tell which of the two ions it is.

By suitable use of two thresholds in the fluorescence level it should be possible to distinguish between zero, one or two fluorescing ions. This requires the mean number of photons produced per ion to be large enough that the Poissonian probability distributions for detecting a given number of photons are non overlapping. To be able to distinguish between one and two ions fluorescing requires a larger mean number of photons detected per ion than is required to distinguish zero from one ion's fluorescence. This implies a longer collection time is required.¹

¹An alternative to thresholding is to fit a sum of Poissonian distributions to the observed photon counts

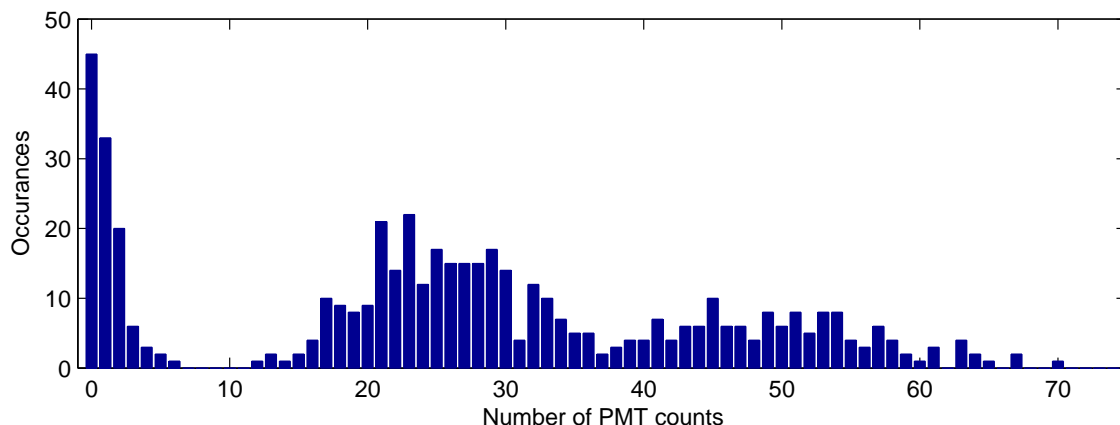


Figure 6.1: Photon distributions for two ion shelving. By use of two thresholds (*e.g.* 7, 36 in this case) it is possible to distinguish between 0, 1 or 2 ions fluorescing. The collection time used was 7 ms. With shorter photon counting times the probability distributions for 1 and 2 ions fluorescing would have significant overlap.

To probe the temperature of the two ion system we do not need to be able to distinguish all three possibilities (0, 1, 2 ions fluorescing). It is sufficient to distinguish the case of no fluorescence (both ions shelved) from some fluorescence (one or no ions shelved), and this is easier to do. Therefore we use the observed proportion of times where both ions are shelved as our temperature probe.

The probability that both ions are shelved is $p_{s,s} = p_{s,s|\downarrow\downarrow}p_{\downarrow\downarrow} + p_{s,s|\downarrow\uparrow}p_{\downarrow\uparrow} + p_{s,s|\uparrow\downarrow}p_{\uparrow\downarrow} + p_{s,s|\uparrow\uparrow}p_{\uparrow\uparrow}$. We can find $p_{s,s|\downarrow\downarrow}$ and $p_{s,s|\uparrow\uparrow}$ by preparing the ions in either $|\downarrow\downarrow\rangle$ or $|\uparrow\uparrow\rangle$ by optical pumping and implementing the readout sequence. We assume that the shelving probabilities for the separate ions are the same (which should be the case as typical ion separation is significantly less than the spot sizes of the shelving beams) so that the other two conditional probabilities can be calculated from the two measured ones. The probability that both ions are shelved is then

$$p_{s,s} = p_{s,s|\downarrow\downarrow}p_{\downarrow\downarrow} + \sqrt{p_{s,s|\downarrow\downarrow}p_{s,s|\uparrow\uparrow}}(p_{\uparrow\uparrow} + p_{\downarrow\downarrow}) + p_{s,s|\uparrow\uparrow}p_{\uparrow\uparrow}. \quad (6.12)$$

6.1.4 Temperature diagnostics

As we saw in the previous chapter, we can deduce the temperature of a single trapped ion in a thermal state from the ratio of the excitation strength on the first red and blue sidebands, because the mean value of n is a simple function of this ratio. An obvious question to ask is, does such a simple method carry over to measuring the temperature of two ions?

The answer to this question is yes. Assuming the ion starts in a thermal state, in the $|\downarrow\downarrow\rangle$ internal state, then the ratio of the excitations to $|\uparrow\uparrow\rangle$ after pulses on the red and blue sidebands is independent of pulse length and a simple function of \bar{n} . The probability of

(*i.e.* the histogram of counts detected when a given experimental sequence is repeated many times). The weights of the three Poissonian functions in the best fit give an estimate of the proportion of trials in which 0, 1 or 2 ions were fluorescing. We tried both methods (*i.e.* fits and thresholds) and found them to give similar results.

the pair of ions being in the upper state after a pulse of length t on the blue sideband is

$$p_{\uparrow\uparrow}^{\text{bsb}}(t) = \sum_{n=0}^{\infty} p(n) \frac{(n+1)(n+2)}{(2n+3)^2} [1 - \cos(g_{b,n}\Omega t/2)]^2, \quad (6.13)$$

and similarly on the red sideband

$$p_{\uparrow\uparrow}^{\text{rsb}}(t) = \sum_{n=2}^{\infty} p(n) \frac{n(n-1)}{(2n-1)^2} [1 - \cos(g_{r,n}\Omega t/2)]^2 \quad (6.14)$$

$$= \sum_{n=0}^{\infty} p(n+2) \frac{(n+1)(n+2)}{(2n+3)^2} [1 - \cos(g_{r,n+2}\Omega t/2)]^2 \quad (6.15)$$

$$= \left(\frac{\bar{n}}{\bar{n}+1} \right)^2 p_{\uparrow\uparrow}^{\text{bsb}}(t) \quad (6.16)$$

since $g_{r,n+2} = g_{b,n}$. The ratio r of the two sideband excitations to $|\uparrow\uparrow\rangle$ is thus the square of the ratio for the one ion case.

$$r = p_{\uparrow\uparrow}^{\text{rsb}}(t)/p_{\uparrow\uparrow}^{\text{bsb}}(t) = \left(\frac{\bar{n}}{\bar{n}+1} \right)^2. \quad (6.17)$$

The quadratic dependence makes accurate measurement of a low temperature difficult since for low temperatures the ratio is small, approximately equal to \bar{n}^2 for $\bar{n} \ll 1$. In practice the shot noise and other noise in the experiment imply that for small r we can only place an upper bound on r using the experimental data. For example if this upper bound is 0.01 then we would be able to deduce an upper bound on \bar{n} of 0.01 in a single-ion experiment but only of 0.1 in a two-ion experiment by this method.

To place a tighter upper bound we should use the data where only one rather than both ions have their spin flipped, and then there is no longer a simple relationship between r and \bar{n} .

We do not measure $p_{\uparrow\uparrow}$ directly, but rather $p_{s,s}$. This combines information from all the possible spin states of the ions (eq. 6.12). Figure 6.2a shows the signal we would expect to see for a thermal population distribution with $\bar{n} = 0.5$ and the two shelving levels being $p_{s,s|\downarrow\downarrow} = 0.2$ and $p_{s,s|\uparrow\uparrow} = 0.7$ (corresponding to single ion shelving ratios of 0.45 and 0.84). As can be seen, the two signals are not in a simple ratio. Instead the shelved population is oscillating faster on the red sideband than the blue sideband. Figure 6.3b shows the ratio r of these two shelved probabilities as a function of pulse length (taking into account the lower conditional probability *i.e.* $r = (p_{s,s}^{\text{rsb}} - p_{s,s|\downarrow\downarrow}) / (p_{s,s}^{\text{bsb}} - p_{s,s|\uparrow\uparrow})$)

Let us take the ratio at the time corresponding to the maximum probability of finding the two ions both in the shelved state $p_{s,s}$ when driving the blue sideband. For $\bar{n}=0.5$ this time corresponds to $\eta_m\Omega_0 t = 2.25$ and the ratio at this time is 0.21. Figure 6.3 shows the value of the ratio (evaluated at this time of maximum $p_{s,s}$) as a function of \bar{n} . Also shown are curves representing the ratio expected for a single ion at that temperature and the ratio expected when the shelving method is perfect ($\epsilon_s = 1$, corresponding to equation 6.17). The time at which the ratio is taken varies from $\eta_m\Omega_0 t = 2.56$ at $\bar{n}=0$ to $\eta_m\Omega_0 t = 1.71$ at $\bar{n}=2$. We conclude that as long as both the shelving levels are known, the ratio of the sideband heights allows the temperature of a thermal two ion crystal to be determined.

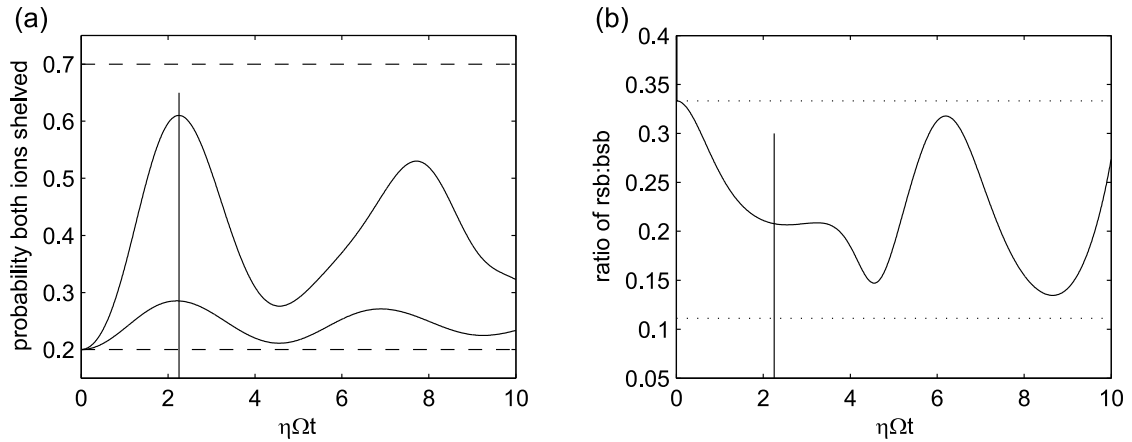


Figure 6.2: (a) Plot showing expected value of the probability $p_{s,s}$ of detecting that both ions are in the shelved (non-fluorescing) state when the two ion system is resonantly driven on either the first red or first blue motional sideband of one of the axial modes. This is for a thermal motional state distribution with $\bar{n}=0.5$ and the two conditional probabilities $p_{s,s|\downarrow\downarrow} = 0.2$ and $p_{s,s|\uparrow\uparrow} = 0.7$. The vertical line marks the value of $\eta\Omega t$ for which the blue sideband signal is at its maximum and the two dashed horizontal lines mark the conditional probabilities. (b) Plot of the ratio of the two probabilities for detection $p_{s,s}$ (taking into account the baseline probability of 0.2). The vertical line is at same time as in (a). Note that for pulse durations equal to and slightly larger than this the ratio is almost independent of the pulse duration. The upper dashed line is the ratio for a single ion of the same temperature, the lower the ratio expected if we had perfect shelving.

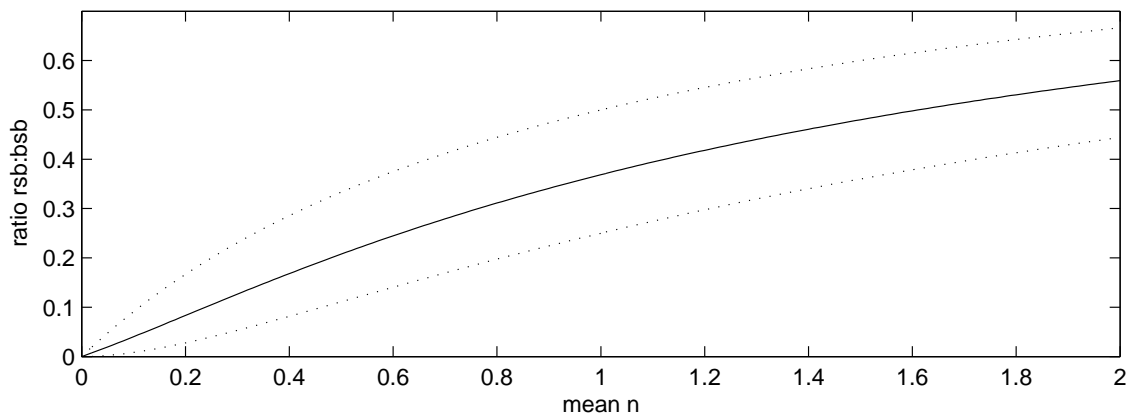


Figure 6.3: Solid line: ratio evaluated at the blue sideband maximum as a function of \bar{n} , for the two ion shelving probabilities $p_{s,s|\downarrow\downarrow} = 0.2$ and $p_{s,s|\uparrow\uparrow} = 0.7$. Upper dotted line: ratio for single ion at same temperature. Lower dotted line: ratio given by equation 6.17 for perfect shelving efficiency. The pulse length used for the non-perfect shelving case varies with \bar{n} , for example $\eta\Omega_0 t = 2.57, 2.02$ and 1.71 for $\bar{n}=0,1$ and 2 respectively.

6.2 Experiments

In the single ion cooling experiments in the last chapter we were only interested in the axial trap frequency, which we made as large as possible. For these two ion experiments we require that the ions lie along the z axis, and so the axial trap frequency is limited by the size of the radial frequency. It was found that even when $\omega_z < \omega_r$ the two ions would not necessarily lie along the z axis. The ions were able to adopt two different configurations, one the required axial crystal, the other perpendicular to the z axis. When the magnitude of the axial frequency is close to the radial one, only the perpendicular crystal was formed. At lower axial frequencies, an axial crystal could be formed when the ion was being strongly Doppler cooled, with the perpendicular crystal corresponding to a more energetic state. However, when the ions were only weakly cooled, as for example during the continuous sideband cooling, the perpendicular configuration was metastable and occasionally the ions would switch to it. In this case a brief burst of Doppler cooling was required to return them to the desired state.

The cooling experiments presented here are for a $2\pi \cdot 306$ kHz axial frequency, and a radial frequency of around $2\pi \cdot 750$ kHz. These values were required to reduce the instability to acceptable levels. More recent experiments have used an axial trap frequency of around $2\pi \cdot 500$ kHz. A frequency of $2\pi \cdot 306$ kHz gives values for the two Lamb-Dicke parameters of $\eta_c = 0.23$ and $\eta_s = 0.17$.

6.2.1 Continuous Sideband Cooling

Fluorescence spectrum

Figure 6.4 shows two fluorescence spectra obtained for two ions with the 397 probe and pump beams as described for single-ion experiments in section 5.3.1. The x axis, displaying the frequency difference between the probe and pump beam, is also a time axis, with the data shown in the figure acquired over time of 147 s.

The two different ion configurations described above are evident here. When the ions are in the unwanted perpendicular configuration the amount of fluorescence seen is independent of the probe frequency, and the count rate observed is around 270 s^{-1} . This is a higher rate than when the ions form an axial crystal (the increased fluorescence is because when the ions are away from the axis they undergo micromotion which gives a Doppler shift making the single-photon transitions nearer to resonance). Several regions producing this count rate are evident in the figure. While the ions can spontaneously return to the axial configuration, in most cases the ions were forced back to the axial configuration by application of the 397 Doppler beam, at times marked by an asterisk ‘*’, for a short (< 1 s) time. This provides a high cooling rate, and produces a burst of fluorescence.

The lower fluorescence level is produced when the ions are the the axial configuration. The feature of primary interest in the spectrum is the broad asymmetric resonance at a frequency difference of 2 MHz. This is reminiscent of the single-ion fluorescence observations for example in the upper half of figure 5.8. In view of our understanding of the single-ion observations, we take this resonance to be off-resonant excitation of the carrier when the probe/pump lasers are tuned near the first red sideband, giving cooling to near the ground state. With two ions we do not expect to see a sideband structure for probe/pump Raman detunings equal to, or blue detuned from, the carrier. This is because of the large number of resonance frequencies present. Whereas with a single ion there was a ladder of

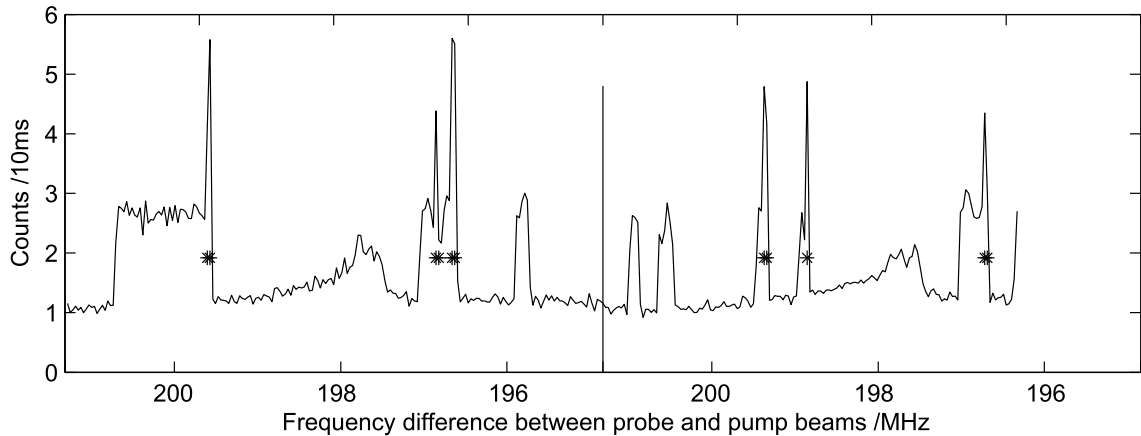


Figure 6.4: Two-ion fluorescence spectrum. Two spectra are shown. The x axis also records time, the data shown here taking 147 s to acquire. The higher fluorescence level (270 s^{-1}) occurs when the ions are not configured in an axial crystal. The 397 Doppler beam can be used to return the ion to this state, and times when this was done are indicated by a star on the graph.

resonance frequencies at detunings $\delta n \omega_z$ (where δn is the change in vibrational quantum number), for two ions the resonance frequencies occur for detunings $\delta n_c \omega_z + \delta n_s \sqrt{3} \omega_z$ (δn_c , δn_s being the change in vibrational quantum number for the COM, stretch modes respectively) and since the two mode frequencies ω_z and $\sqrt{3} \omega_z$ are non-commensurate a forest of different resonance frequencies results.

This forest of resonant frequencies similarly affects the taking of a sideband spectrum using the Raman beams, so in contrast to the case of a single ion (figure 4.9), a sideband structure will only be seen when a two-ion crystal is cooled well below the Doppler limit temperature.

Raman spectrum

As we cannot identify the carrier position directly on the fluorescence spectrum, the correct positioning in frequency of the probe beam is more uncertain for the two-ion experiment. We know that for one ion the ‘edge’ of the resonance observed in continuous fluorescence occurs between the carrier and the first sideband, and detunings to the red of this edge produce cooling. The same should occur for two ions, and therefore we pick a probe detuning 200-300 kHz to the red of the edge. Note that it would be difficult to measure the light shift, and thus deduce the carrier position, because unlike in the case of one ion we need to have cold ions to be able to see a Raman spectrum, which requires the use of the beam we are trying to measure.

To diagnose the result of the continuous cooling, we used the Raman laser beam pair to take Raman spectra. A first Raman spectrum was recorded to confirm the position of the sidebands, and then a time scan on the first blue sideband for the stretch mode was performed. The time for maximum population inversion was $16 \mu\text{s}$. A Raman spectrum scan with this Raman pulse time was performed, and is shown in figure 6.5. As discussed in section 6.1.3 we do not perform a complete tomography of the spin state, instead what is shown is the probability of finding both ions shelved ($p_{s,s}$). The conditional probabilities for the shelving were measured to be $p_{s,s|\downarrow\downarrow} \simeq 0.08$ and $p_{s,s|\uparrow\uparrow} \simeq 0.68$. Marked above the

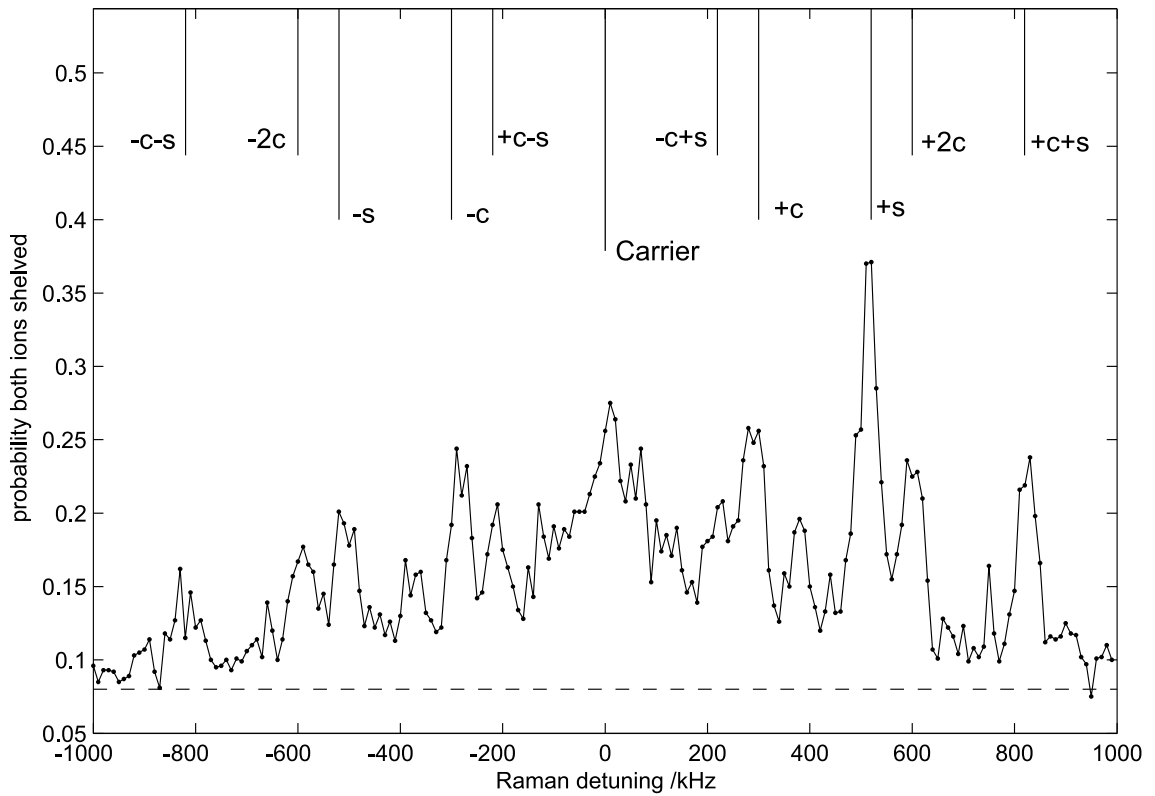


Figure 6.5: Two ion Raman spectrum after 1 ms of continuous cooling. The data shows the probability that both the ions are found to be shelved, after a $16\ \mu\text{s}$ pulse from the Raman laser, followed by a shelving pulse. The resultant spectrum is more complex than that for a single ion, with a large number of resonances. The lines above the spectrum show the expected positions of low-order sideband transitions, with the lines labelled by the change in vibrational quantum number, c indicating a COM transition and s indicating a stretch transition. The COM frequency is $2\pi \cdot 306\ \text{kHz}$.

spectrum are the positions of all the possible sideband transitions to 2nd order in Lamb-Dicke parameter (except the 2nd stretch sidebands, which are of too high a frequency). These match the resonances seen in the sideband spectrum. The size of the sidebands can be used to estimate a temperature for the stretch mode of $\bar{n}_s \sim 1.3$.

6.2.2 Pulsed sideband cooling

To achieve lower temperatures we used pulsed sideband cooling to reduce the motional energy of the two ion system. Unlike the continuous cooling method, which cools both motional modes, each pulse of sideband cooling acts on only one of the modes, allowing us to cool either one of the modes only, or by alternating which sideband is driven to cool both the modes.

We demonstrate here the cooling of both axial modes using the pulsed technique. In addition to the synth driving the 60° Raman beam AOM, we require three synths to be connected to the parallel Raman beam AOM, so as to be able to generate frequency differences corresponding to the two modes we wish to cool as well as a scannable frequency difference to generate Raman spectra.

The pulsed cooling we give results for here consists of ten repeats of the following sequence:

$22 \mu\text{s}$ pulse on the first red centre of mass sideband, followed by a repumping pulse, followed by a $29 \mu\text{s}$ pulse on the first red stretch sideband and then a second repumping pulse. The time for the stretch mode pulse was picked to provide good inversion of the population, and this time used to set the duration of the COM pulse, $t_c = t_s/3^{1/4}$, as set by the ratio of the Lamb-Dicke parameters.

The pulse duration scan used to set the pulse length for the temperature measurement of the stretch mode is shown in figure 6.6(a). The time of maximum inversion (our ‘ π ’ time for finite temperature) was $28 \mu\text{s}$. Frequency scans over the first blue and red sideband of the stretch mode are shown in parts (b) and (c) respectively of the same figure. The conditional shelving probabilities were measured as $p_{s,s|\downarrow\downarrow} \simeq 0.14$ and $p_{s,s|\uparrow\uparrow} \simeq 0.73$ and the observed ratio of sideband heights is 0.20. Using the method of analysis described in section 6.1.4 this implies $\bar{n}_s=0.5$. A similar set of scans were made for the centre of mass mode. This gave a sideband ratio of 0.33, implying $\bar{n}_c=0.9$.

Comparison of inversion times

We can compare the population inversion times on the first sideband for the two modes with the carrier, to check for consistency. For the stretch mode $t_s = 28 \mu\text{s}$, the COM $t_c = 14 \mu\text{s}$ and the carrier $t_{\text{car}} = 5.5 \mu\text{s}$. First we will compare the stretch time with the carrier time. If we initially consider the case of $\bar{n}_s=0$ and perfect shelving we can work analytically. For the carrier transition, the two ions behave in exactly the same way as the single ion did, *i.e.* independent Rabi flopping. The amplitude $\langle \uparrow\uparrow | \Psi(t) \rangle$ oscillates with frequency $\Omega/2$ and the population with frequency Ω . For the first blue stretch sideband transition, the amplitude $\langle \uparrow\uparrow | \Psi(t) \rangle$ oscillates with frequency $\sqrt{6}\eta_s\Omega/2$ (see table 6.1), and the population undergoes a non-sinusoidal oscillation of the same period. Therefore the π times differ by a factor $\sqrt{6}\eta_s/2 \simeq 0.21$. If we take into account the temperature and shelving, the ratio of times should be 0.24. We measure a ratio of 0.20. We can perform a similar calculation for the COM mode. Again taking into account the finite temperature and shelving, we would expect a ratio of the times on the carrier to those on the first COM sideband to be 0.35; the observed value was 0.39.

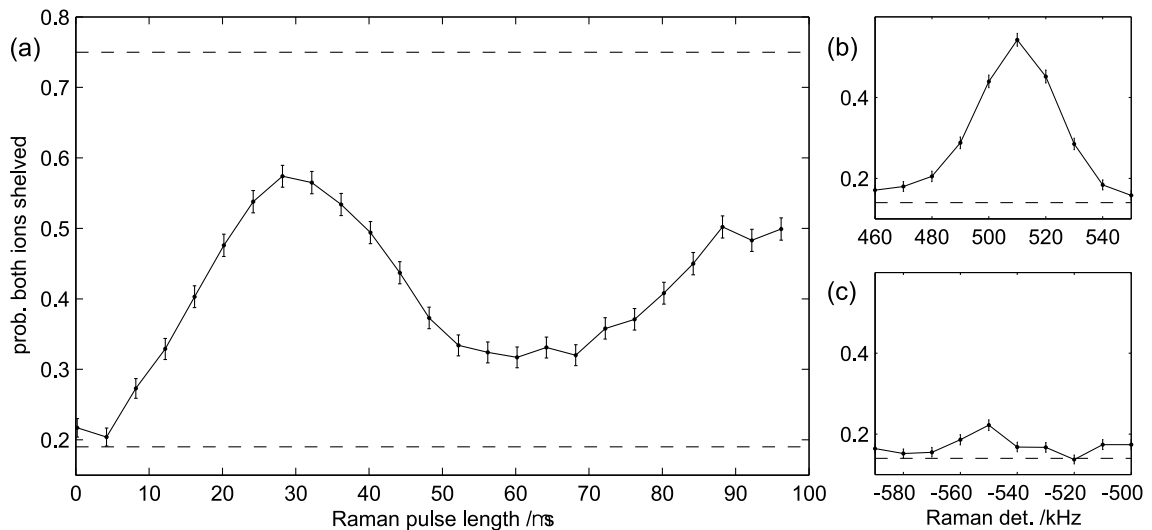


Figure 6.6: Temperature measurement of stretch mode. (a) Time scan on first blue stretch sideband. Maximum population inversion occurs at $28 \mu\text{s}$. (b) Scan over first blue stretch sideband. (c) Scan over first red stretch sideband. Ratio of sidebands implies $\bar{n}_s=0.5$. For plots (b) and (c) zero detuning on the x axis corresponds to a Raman beam frequency difference of 4.70 MHz , nominally the Zeeman splitting. Magnetic field drift has caused the sideband frequencies to be offset from $\pm 530 \text{ kHz}$.

6.3 Conclusions

In this chapter we presented analysis and experiments on the cooling of two ions.

The analysis of Rabi flopping signals expected with a pair of trapped ions showed that some care is required in using the Raman beams to perform a measurement of the mean excitation of a motional mode. It is still possible to extract the degree of excitation by making measurement of the excitation of the ion pair on the first red and blue sideband of the mode under investigation, however unlike the case of the single ion where we only had to know $p_{s|\downarrow}$ and the two sideband excitation probabilities, for the pair of ions both shelving probabilities $p_{s,s|\downarrow\downarrow}$ and $p_{s,s|\uparrow\uparrow}$ are required. In addition we have to ensure that the length of time the sidebands are driven for matches the time of maximum inversion on the blue sideband, as the ratio measurement is not time independent.

Experimentally, we have performed preliminary cooling experiments on pairs of ions. We have demonstrated cooling of an ion pair using red detuned continuous cooling, and then further pulsed sideband cooling on both of the axial motional modes. After pulsed cooling temperatures of $\bar{n}_c=0.9$ and $\bar{n}_s=0.5$ were measured. This corresponds approximately to each of the two modes having the same energy, and implies that the both modes are comfortably in the Lamb-Dicke regime.

Chapter 7

$^{43}\text{Ca}^+$

The experiments described up until this point have used the $^{40}\text{Ca}^+$ isotope. The lack of hyperfine structure makes this easy to work with, while the fact that it is by far the most abundant isotope makes it the easiest isotope to trap. This chapter gives a largely theoretical study of some of the issues involved in using a different calcium ion isotope $^{43}\text{Ca}^+$. Loading of $^{43}\text{Ca}^+$ ions is described in chapter 3 and appendix A.

The first section examines why we would want to switch isotope, specifically with reference to readout, and the phase stability of qubits embodied by the ions.

The following section gives details of modelling the populations in the sublevels of the ion using a rate equation approach. This is then used to perform a fit to a fluorescence spectrum taken from a $^{43}\text{Ca}^+$ ion when driven by the 393, 397, 866 and 854 lasers. We then investigate how to obtain the maximum fluorescence when using a 397 laser modulated using an EOM, and the effect of also modulating the 866. Finally we look at using a combination of circularly and linearly polarised 397 light to optically pump the population to the high m_F sublevels of the ground state while still obtaining a high fluorescence rate.

7.1 Why change isotope?

There are two properties of $^{40}\text{Ca}^+$ and the way in which we use it as a qubit which limit it for quantum information experiments. These are the efficiency ϵ_s of our readout method and the phase stability of the qubit.

The efficiency of our readout method is not currently an important limitation for the types of experiments we are performing. As already explained in section 4.2 of chapter 4, to perform tomography on a qubit and determine the values of $|\alpha|^2$ and $|\beta|^2$ for a qubit in the pure state $|\Psi\rangle = \alpha|0\rangle + \beta|1\rangle$ requires multiple measurement of copies of the qubit, even for perfect measurement ($\epsilon = 1$). For less efficient measurement, to determine the coefficients to the same accuracy merely requires more measurements to be repeated. To be able to perform experiments such as teleportation and error correction however requires measurement efficiencies close to 1, as the fidelity of the overall process depends on the accuracy of the measurement process.

The efficiency of our current method could be improved with a higher 850 laser power, as well as decreased laser linewidth of the 393 and 850 lasers, as this would increase the darkness of the dark resonance used to inhibit excitation. Even if these improvements could be made the maximum efficiency is limited to $\sim 92\%$ [31] by decay from $4P_{3/2}$ to the $3D_{3/2}$ level. Other methods of readout are considered in [30] and very briefly listed here.

The 393 and 854 lasers can be used to drive a Raman transition from one of the ground states into the shelf, however to achieve an efficient transfer requires the laser linewidths to be small. Alternatively, a stimulated Raman adiabatic passage (STIRAP) process could be performed using the same lasers. This process again requires a low laser linewidth. Alternatively, the $4S_{1/2} \leftrightarrow 3D_{5/2}$ transition can be driven directly by a 729 nm laser. This is similar to the Innsbruck group who use as their qubit one sublevel from each of these levels, driven by the 729 laser. They achieve efficiencies of readout close to 1[54]. All of these would require technically demanding high stability lasers.

The other limiting factor of $^{40}\text{Ca}^+$ lies in the phase stability of the qubit. All of the transitions in the ion have a first order Zeeman effect. This means that fluctuations in the magnetic field experienced by the ion can cause phase decoherence of the qubit. For the qubit we use, $\delta\omega_0 = 2\pi \cdot 2.8 \text{ MHz/G}$. For a qubit split between the $4S_{1/2}$, $3D_{5/2}$ levels as above, the effect depends on which magnetic sublevels are used, but the minimum value is $\delta\omega_0 = 2\pi \cdot 0.56 \text{ MHz/G}$. One way to beat phase decoherence due to fluctuating magnetic fields is to recognize that two ions in the same trap will experience the same fluctuations. It is then possible to store a single qubit of information in a decoherence free subspace (DFS)[60] of the two ions, such that the logical qubit is not affected by the common phase noise (for example $|0\rangle_{\text{logical}} = |\uparrow\rangle_1|\downarrow\rangle_2$ and $|1\rangle_{\text{logical}} = |\downarrow\rangle_1|\uparrow\rangle_2$). This would however add much complexity to the design. This DFS can be seen in results from Innsbruck. They created the 4 Bell states in a pair of ions. The states $(|00\rangle \pm |11\rangle)/\sqrt{2}$ had a decoherence time of $200 \mu\text{s}$, whereas the states $(|01\rangle \pm |10\rangle)/\sqrt{2}$ had a decoherence time of 5 ms [61]¹.

These problems can be overcome in part by using the $^{43}\text{Ca}^+$ isotope, and encoding the qubits in two sublevels of the hyperfine structure of the ground state, one in each F state. An energy level diagram showing the hyperfine splittings is shown in figure 7.1. This choice of levels allows easy readout, as the two states are separated by 3.2 GHz, allowing optical pumping of population into the $3D_{5/2}$ ‘shelf’ via the $4P_{3/2}$ level from one of the qubit states, with only minimal excitation from the other. A choice of qubit levels of $|0\rangle \equiv |F=3, m_F=3\rangle$ and $|1\rangle \equiv |F=4, m_F=4\rangle$ would allow easy initialisation by optical pumping, and a state dependent force could easily be applied, allowing a wobble type gate to be performed.

These levels however have a large Zeeman effect ($\delta\omega_0 = 2\pi \cdot 2.45 \text{ MHz/G}$). There exist transitions which are first order insensitive to field fluctuations, such as $|0\rangle \equiv |F=3, m_F=0\rangle$ and $|1\rangle \equiv |F=4, m_F=0\rangle$ and also various possibilities when a stronger field is applied and the Zeeman effect is in the intermediate field regime. The disadvantage of these states is that the state dependent force which allows us to perform a wobble gate is no longer present, requiring either a different gate or for population in one of the two basis states to be transferred to another sublevel whenever a gate operation is required.

7.2 Modelling $^{43}\text{Ca}^+$

We use a rate equations program to model the internal dynamics of the $^{43}\text{Ca}^+$ ion. This only takes into account the populations in each of the sublevels (144 in total), and does not keep track of the coherences between levels. This approach is valid for situations in which these coherences have no effect on the dynamics, so for instance is not appropriate when levels are coupled together by two lasers in Raman resonance or when the magnetic

¹By removing other decoherence sources, these DFS states were shown to have a lifetime of 1 s, limited by the spontaneous decay of the D state used by Innsbruck.

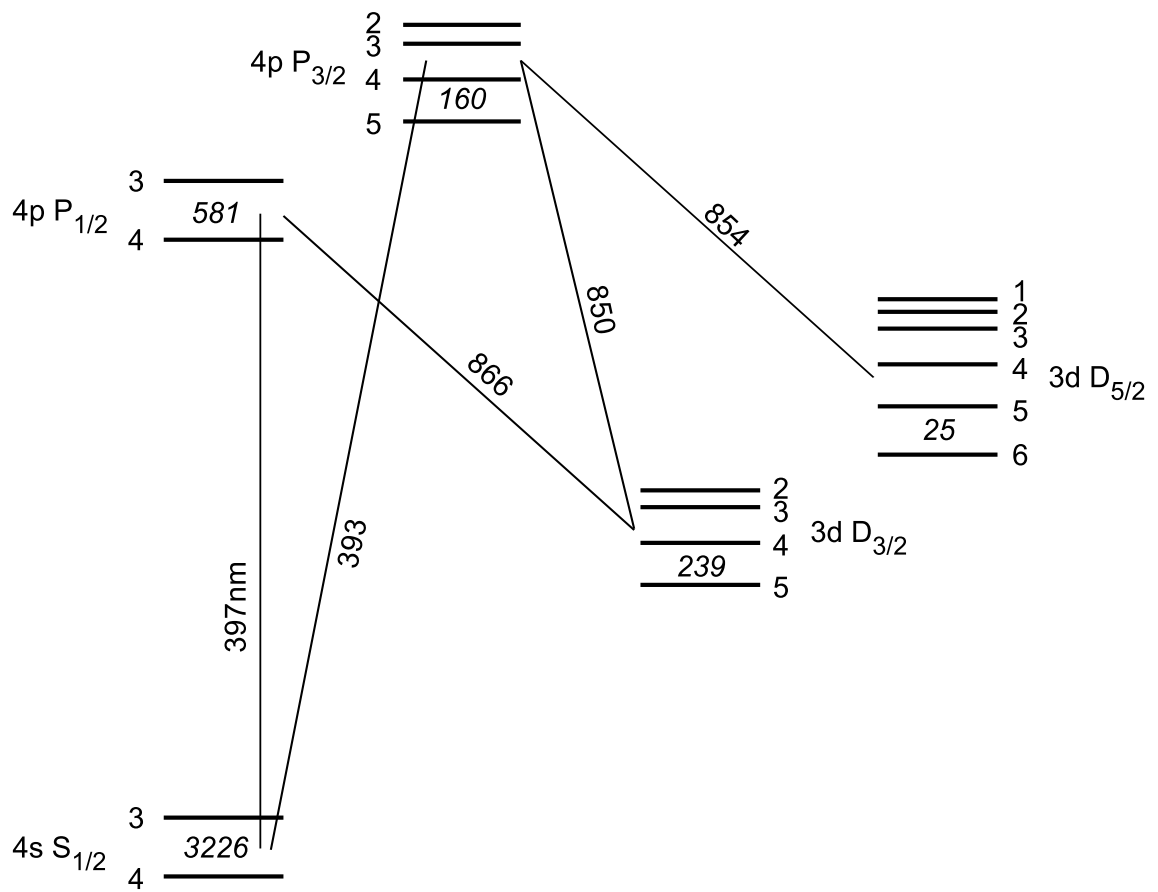


Figure 7.1: Energy level diagram for $^{43}\text{Ca}^+$. The largest hyperfine splitting of each fine structure level is indicated in MHz (the level spacings approximately conform to an interval rule). Hyperfine levels are labelled by their total angular momentum F .

	$4S_{1/2}$	$3D_{3/2}$	$3D_{5/2}$	$4P_{1/2}$	$4P_{3/2}$
A	-806.402	-47.3(2)	-3.8(6)	-145.4(1)	-31.0(2)
B	-	-4(2)	-4(6)	-	-7(2)

Table 7.1: Hyperfine structure constants for $^{43}\text{Ca}^+$ / MHz

field is very small and the ion can be driven into a dark state by a laser[62]. To model these coherences would require substantially more complexity, with $144^2 = 20736$ different density matrix elements needed.

Two sets of information are required, the structure of the bare atom and the rates that population moves between the sublevels when it is illuminated by a set of laser fields.

Hyperfine splitting

The energy shift of the hyperfine components relative to the centre of gravity is given by[63]

$$\Delta E_F = \frac{A}{2}C + \frac{B}{4} \frac{\frac{3}{2}C(C+1) - 2I(I+1)J(J+1)}{(2I-1)(2J-1)IJ} \quad (7.1)$$

where A is the magnetic dipole coupling constant and B the electric quadrupole coupling constant, which are tabulated in table 7.2[64, 65, 66]. J , I ($= 7/2$) and F are the electronic, nuclear and total angular momenta and $C = F(F+1) - I(I+1) - J(J+1)$.

Spontaneous and stimulated rates

The rate of spontaneous decay between two different hyperfine sublevels connected by an electric dipole transition, upper sublevel j , lower sublevel i , can be written as[67]:

$$\Gamma_{j \rightarrow i} = C^2 S A_{ij} \quad (7.2)$$

C^2 is the square of the Clebsch-Gordon coefficient for the transition and S is the relative strength of the particular $F_j \rightarrow F_i$ hyperfine component of the transition. These quantities depend only on the angular momenta of the sublevels and of the photon emitted. A_{ij} is the Einstein A coefficient for the transition. Table 7.2 gives the coefficients for the five transitions in which we are interested. We ignore the electric quadrupole decays from the metastable levels.

The Clebsch-Gordon coefficient is expressed as follows, using a $3j$ symbol:

$$C^2 = (2F_j + 1) \left(\begin{array}{ccc} F_i & 1 & F_j \\ m_{F_i} & q & m_{F_j} \end{array} \right)^2 \quad (7.3)$$

where q is the projection of the angular momentum of the emitted photon along the axis, equal to $1(\sigma^+)$, $0(\pi)$ or $-1(\sigma^-)$. The Clebsch-Gordon coefficient is only non-zero if $m_{F_i} + q = m_{F_j}$.

The strength S of the component is expressed in terms of a $6j$ symbol:

$$S = (2J_j + 1)(2F_i + 1) \left\{ \begin{array}{ccc} F_j & F_i & 1 \\ J_i & J_j & \frac{7}{2} \end{array} \right\}^2 \quad (7.4)$$

The total decay rate from the j th sublevel is simply the sum over all destination sublevels

$$\Gamma_j = \sum_i \Gamma_{j \rightarrow i}. \quad (7.5)$$

Transition	A coefficient / Ms^{-1}	Saturation intensity I_0 W/ m^2
$4\text{S}_{1/2} \leftrightarrow 4\text{P}_{1/2}$	132	937
$4\text{S}_{1/2} \leftrightarrow 4\text{P}_{3/2}$	136	986
$3\text{D}_{3/2} \leftrightarrow 4\text{P}_{1/2}$	8.4	90.1
$3\text{D}_{3/2} \leftrightarrow 4\text{P}_{3/2}$	0.91	97.8
$3\text{D}_{5/2} \leftrightarrow 4\text{P}_{3/2}$	7.7	96.3

Table 7.2: Einstein A coefficients and saturation intensities for Ca^+ electric dipole transitions

We can now work out the stimulated rates. The Rabi frequency for transitions from lower sublevel i to upper sublevel j can be shown to be [68, 69]

$$\Omega_{ij}^2 = \frac{6\pi c^3 C^2 S A_{ij}}{\hbar \omega_{ij}^3} \frac{I}{c} = C^2 S A_{ij} \Gamma_j \frac{I}{I_0} \quad (7.6)$$

where we have defined a reference saturation intensity

$$I_0 = \frac{\hbar \omega_{ij}^3 \Gamma_j}{6\pi c^2}. \quad (7.7)$$

Values of the saturation intensity for the five dipole transitions are listed in table 7.2.

The stimulated excitation/emission rate is given by Fermi's Golden Rule:

$$R_{ij} = \frac{\pi}{2} \Omega_{ij}^2 g(\omega_l - \omega_{ij}) \quad (7.8)$$

where the lineshape function $g(\delta)$ is given by

$$g(\delta) = \frac{\Gamma_j / (2\pi)}{\delta^2 + \Gamma_j^2 / 4}. \quad (7.9)$$

For convenience we can write our rate in terms of the decay rates

$$R_{ij} = \frac{\pi}{2} \Gamma_j \Gamma_{j \rightarrow i} \frac{I}{I_0} g(\omega_l - \omega_{ij}) \quad (7.10)$$

7.2.1 Rate equations

For each sublevel, the rate of change of the population equals the rate that population is being added to the sublevel by stimulated and spontaneous processes from the other sublevels, minus the rate population is leaving the sublevel by stimulated and spontaneous processes.

Writing this algebraically,

$$\frac{dn}{dt} = \mathbf{Mn} = (\mathbf{M}^{inc} - \mathbf{M}^{dec})\mathbf{n} \quad (7.11)$$

where n_i is the population in the i th sublevel and \mathbf{M}^{inc} (\mathbf{M}^{dec}) is a matrix detailing the processes causing population to enter (leave) the sublevels. These matrices are as follows:

$$M_{ij}^{inc} = R_{ij} + \Gamma_{j \rightarrow i} \quad (j > i) \quad (7.12)$$

$$= R_{ij} \quad (j < i) \quad (7.13)$$

$$M_{ii}^{dec} = - \sum_j M_{ij}^{inc}, \quad M_{i,j \neq i}^{dec} = 0 \quad (7.14)$$

Once this matrix \mathbf{M} has been generated, we can calculate the populations in the ion. We will start with the calculation of the steady-state population vector \mathbf{n}^s . Setting equation 7.11 equal to zero will not produce a unique solution as, due to the way \mathbf{M} is generated, the problem is underconstrained. This is a consequence of the fact we only need to know 143 of the populations to know the 144th, as the total population is equal to one, and we use this constraint to find the steady-state. Therefore we replace one of the population rate equations with $\sum n_i = 1$. To be specific we construct a vector $y_i = 0 (i \neq 144), = 1 (i = 144)$ and a matrix $M'_{ij} = M_{ij} (i \neq 144), = 1 (i = 144)$. Now, if we have picked lasers and polarisations such that there is a unique steady-state (for instance, we must always include an 854 laser since we have not included decay from the $3D_{5/2}$ level) the equation $\mathbf{M}'\mathbf{n}^s = \mathbf{y}$ can be solved to obtain the steady-state.

The results presented below are all concerned with steady state populations. Nevertheless it is also possible to study the dynamics of the ionic populations by integrating equation 7.11, and provided \mathbf{M} is constant we get

$$\mathbf{n}(t) = e^{\mathbf{M}t} \mathbf{n}_0 \quad (7.15)$$

7.3 Program results

Here we investigate the steady state fluorescence emitted by a $^{43}\text{Ca}^+$ ion for various laser situations, using the rate equations approach detailed above. Contained in appendix B is a program listing for Matlab which contains routines for generating the matrix \mathbf{M} , and a short example program which generates the fit shown in section 7.3.1.

7.3.1 Cooling with the 393 laser

During our photoionization experiments we were able to trap and cool single $^{43}\text{Ca}^+$ ions. Since the ground state of the ion has two hyperfine components separated by 3.2 GHz we were not able to Doppler cool using a single 397 laser as population would remain in whichever hyperfine level the laser did not excite. The use of both 393 and 397 lasers allows efficient excitation from both levels and thus effective Doppler cooling. We gave an example of cooling $^{43}\text{Ca}^+$ using these two blue lasers in our paper (contained in appendix A).

The 393 laser was used as the cooling laser and was red-detuned from the $4S_{1/2} F = 4 \leftrightarrow 4P_{3/2} F = 5$ transition. This transition is almost closed, as the only decay back to the ground state is to $F = 4$. Decay to the D states, and the resultant repumping by the 854 and 866 or 854, leads to population entering the $4S_{1/2} F = 3$ level. The 397 laser can then be used as a repumper to excite the ion from $4S_{1/2} F = 3$. To further enhance the scattering rate the 393 laser was σ^+ polarised so that the ion is optically pumped into the $m_F = 4$ sublevel and the cooling transition is the $F = 4 m_F = 4 \rightarrow F = 5 m_F = 5$ ‘stretch’ transition.

Since the 397 is being used as a repumper the width of the fluorescence spectrum, as the frequency of the 397 is altered, can be much greater than the natural linewidth of the upper state. By reducing the power of the 397 the two hyperfine components $4S_{1/2} F = 3$ to $4P_{1/2} F = 3$ and 4 can be resolved.

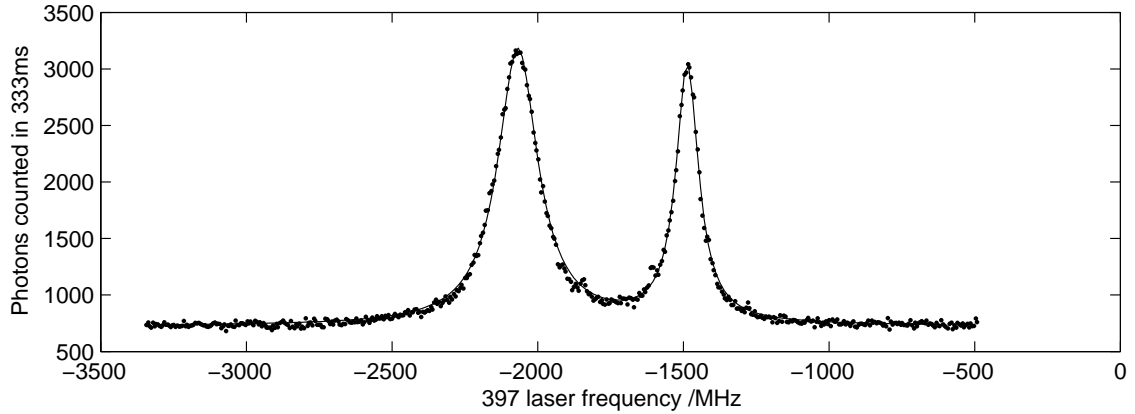


Figure 7.2: Scan of the 397 laser over two hyperfine transitions in $^{43}\text{Ca}^+$. The points are data, the line is a fitted curve. A σ polarised 393 laser provided the main Doppler cooling, with σ^+/σ^- polarised 397, 866 and 854 acting as repumpers. To obtain this plot the 397 intensity was substantially reduced so as to be able to resolve the two hyperfine components. The intensities of the lasers used for the fit are $0.26I_0^{397}$, $0.26I_0^{393}$, $96I_0^{866}$ and $2110I_0^{854}$.

Shown in figure 7.2 is data taken in this way. The fluorescence emitted by the ion was measured as the 397 frequency is scanned over the hyperfine components of the $4P_{1/2}$ upper state. Each data point is the result of photon counting for 333 ms. The four lasers used, their polarisations and their intensities inferred from measured beam sizes and powers are as follows. The 397 was σ^+/σ^- with intensity $0.36I_0^{397}$, the 393 was σ^+ polarised with intensity $0.22I_0^{393}$, the 866 σ^+/σ^- with intensity $96I_0^{866}$ and the 854 σ^+/σ^- with intensity $2110I_0^{854}$.

Also shown in figure 7.2 is a fit to the experimental data using the rate equations program. The predicted count rate is easily calculated from the population in the 4P levels and the known net collection efficiency of the optical system of 0.13% [39] (this data was taken before the imaging system was modified by adding a pinhole before the PMT). The frequency offset and background counts are set to match the data.

The other parameters to set are the frequencies of the 393, 866 and 854 lasers. The 866 and 854 frequencies are set to produce maximum fluorescence. The 393 frequency is detuned to the red of the $4S_{1/2} F = 4 \leftrightarrow 4P_{3/2} F = 5$ by $2\pi \cdot 20$ MHz, which produces half the fluorescence that zero detuning results in, mimicking experimental conditions.

To achieve a good fit the intensities of the 393 and 397 lasers had to be assigned the values $I^{393} = 0.26I_0^{393}$ and $I^{397} = 0.26I_0^{397}$. These agree with the measured values within experimental uncertainty.

7.3.2 Cooling with multiple 397 frequencies

To be able to read out using an electron shelving method requires of course that the ion cannot be excited to the $3D_{5/2}$ shelf level during Doppler cooling, which precludes the use of the 393 laser as above. By using an electro-optic modulator (EOM) to add sidebands to the 397 laser at 3.2 GHz it is possible to get a high scattering rate using just the 397 and 866 lasers. This is important of course both for a high cooling rate and for a short detection period during readout.

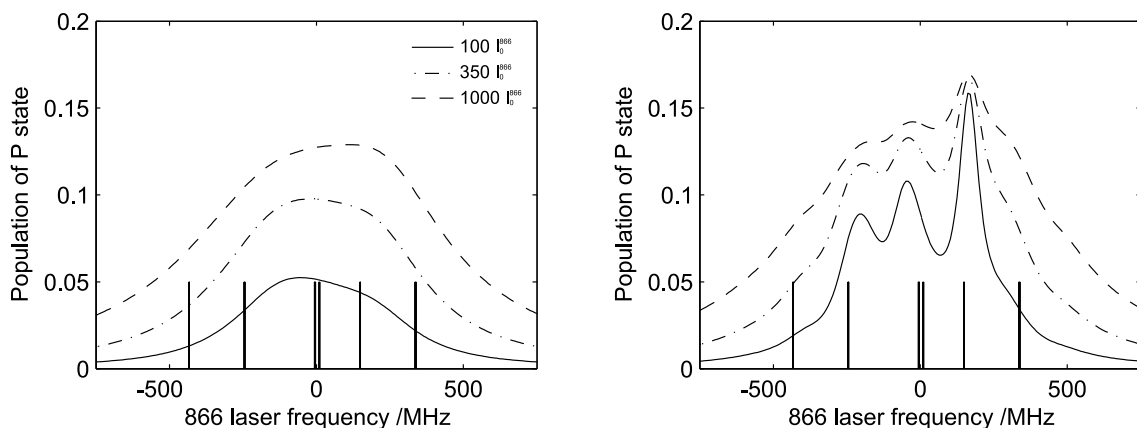


Figure 7.3: Scan of 866 frequency for three different 866 powers. The 397 carrier frequency is resonant with the $4S_{1/2} F = 4$ to $4P_{1/2} F = 4$ transition, a 397 sideband is resonant with the $4S_{1/2} F = 3$ to $4P_{1/2} F = 4$ transition. The total 397 intensity is $10I_0^{397}$, $5I_0^{397}$ in the carrier, $2.5I_0^{397}$ in each of the sidebands. The 866 intensities used are 100, 350 and $1000I_0^{866}$. Figure (a) is for a single 866 frequency. Figure (b) shows the result of adding sidebands at 170 MHz to the 866 laser, with the intensity levels in the carrier and sidebands in the same proportion as for the 397, *i.e.* 50% intensity in the carrier, and 25% in each of the sidebands. The vertical lines mark the frequencies of the different hyperfine transitions which can be driven by the 866.

We assume in these studies that the 397 power available is $10I_0^{397}$, and that the power in each of the two sidebands is half that found in the carrier (*i.e.* carrier power $5I_0^{397}$, and $2.5I_0^{397}$ in each of the sidebands). An EOM frequency equal to the hyperfine splitting of 3.226 GHz is also assumed. We are interested in maximising the amount of fluorescence emitted by the ion when the 397 laser is resonant with its transition.

Shown in figure 7.3a is the population in the $4P_{1/2}$ state as the frequency of the 866 laser is scanned, for three different 866 intensities. The 397 frequency is set so that the carrier frequency is resonant with the $4S_{1/2} F = 4$ to $4P_{1/2} F = 4$ transition, making one of the sidebands resonant with the $4S_{1/2} F = 3$ to $4P_{1/2} F = 4$ transition. The power in the other sideband has negligible effect on the ion, being far from resonant. The 866 powers used are 100, 350 and $1000I_0^{866}$. Both lasers have σ^+/σ^- polarisation.

The different hyperfine components mean that a single 866 frequency requires moderately high intensities to be able to repump from the different F levels efficiently. The effect on maximum $4P_{1/2}$ excitation of the 397 carrier frequency addressing one of the other three $4S_{1/2} \leftrightarrow 4P_{1/2}$ transitions is relatively small, with this 397 frequency offering the highest P state populations. We deduce we do not require the repumping laser to have sidebands for reasonable $4P_{1/2}$ population. We can however investigate how much the upper state population increases if we do add sidebands to the 866, and the result of this is shown in figure 7.3b.

We considered the same three total 866 intensities as before, and split it so that 50% of the intensity is at the carrier frequency and 25% in each of the sidebands. The modulation frequency used is 170 MHz. This was found by numerical exploration to be the most effective 866 modulation frequency in the case where the 397 laser excites to $4P_{1/2}$

$F=4$.² Figure 7.3(b) shows that the $4\text{P}_{1/2}$ state population is highest when the carrier frequency of the 866 laser is almost resonant with the $3\text{D}_{3/2} F=3 \leftrightarrow 4\text{P}_{1/2} F=3$ transition. Population in all of the $3\text{D}_{3/2}$ levels is repumped efficiently for all three intensities, as is evident from the only small increase in $4\text{P}_{3/2}$ population with increased 866 powers.

7.3.3 Cooling using circularly polarised 397 light

Finally, we investigate if it is possible to concentrate the population of the ground state levels in high m_F sublevels during this 397-866 Doppler cooling. This is useful because it means that fewer photons have to be scattered during the optical pumping into the initial state, reducing heating due to the scattering.

We do this by making the modulated 397 laser σ^+ polarised. If this were the only laser present then we would observe no fluorescence as the system would be optically pumped to the $4\text{P}_{1/2} F=4 m_F=4$ sublevel from where no transitions would occur. To counter this we introduce a π polarised 397 beam which can excite from this sublevel. We make this the same frequency as the carrier in our model, as experimentally both lasers would be derived from the same source and it is most practical not to have to introduce a frequency difference between the two beams. With these lasers and polarisations, only one choice of 397 carrier frequency gives non-minimal excitation from the $4\text{S}_{1/2}$ levels, that corresponding to the $4\text{S}_{1/2} F=4 \leftrightarrow 4\text{P}_{1/2} F=4$ transition we have used in the examples above. See figure 7.4a.

We consider laser intensities the same as one of the cases above - an 866 intensity of $350I_0^{866}$, with 170 MHz modulation as above, and a total 397 intensity of $10I_0^{397}$, which is divided between the two beams. Figure 7.4b shows the excitation as a function of 866 frequency, as an example, when the 397 intensity is split in the ratio 4:1 between the σ^+ and π beams. In comparison to the use of a single σ^+/σ^- beam the excitation to the upper state is actually greater, so we would not lose out in terms of scattered rate by using this arrangement of two beams.

Looking at the population in the different sublevels we can see that populations are shifted to higher m_F states. Figure 7.5 shows the steady state population in the sublevels of the ground state, as well as the total population in the P and D levels, for four different divisions of intensity, for the conditions listed above. The populations are plotted for the 866 detuning giving the greatest P level population. Figure 7.5a gives the populations for a ratio 4:1 between the intensity in the σ^+ and π beams. As can be seen, there is substantial shifting of the ground state population to high m_F sublevels, with 47% of the ground state population in $|F=3, m_F=3\rangle$ or $|F=4, m_F=4\rangle$. As the intensity of the π polarised 397 beam is reduced, the population in $4\text{P}_{1/2}$ (and thus the fluorescence emitted) reduces and the proportion of the ground state population in the highest m_F sublevels increases.

Even with just a 40th of the 397 intensity in the π polarised beam (figure 7.5d) there is still substantial population in $4\text{P}_{1/2}$, with 11% of the population in these sublevels compared with 17% in the 4:1 intensity ratio case. Just over 75% of the ground state population is then in either $|F=3, m_F=3\rangle$ or $|F=4, m_F=4\rangle$.

²If the 397 laser excites to $4\text{P}_{1/2} F=3$ then a larger modulation frequency of 210 MHz is best.

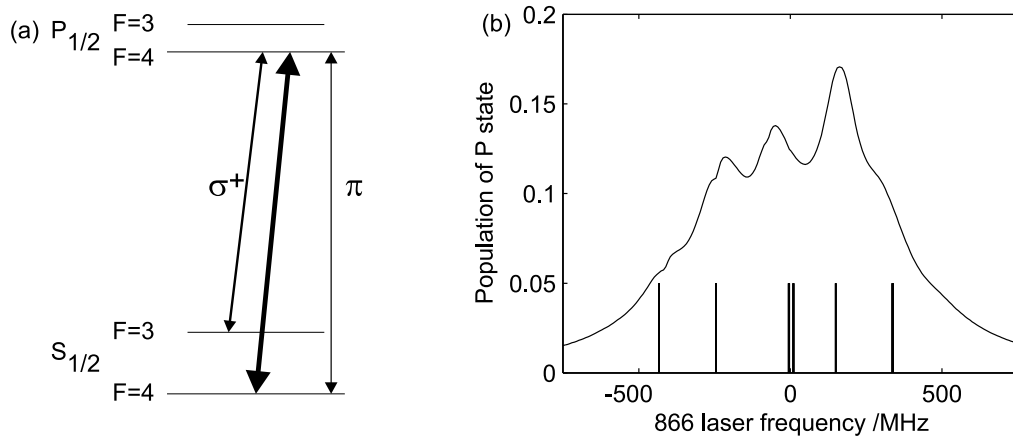


Figure 7.4: (a) Excitation from the ground state using σ^+ and π polarised 397 light. The majority of 397 intensity is the σ^+ polarised beams, with multiple frequencies provided by the EOM. In addition a small amount of intensity is in a π polarised beam, at the same frequency as the carrier of the modulated 397 beam. In this way a high excitation rate is combined with concentration of population in the high m_F states. (b) Scan of 866 frequency for cooling with σ polarised light. The total 397 intensity is again $10I_0^{397}$, with this split in the ratio 4:1 between the σ^+ modulated beam and the unmodulated π beam. The 866 beam is of intensity $350I_0^{866}$ and modulated with 170 MHz sidebands as described in section 7.3.2.

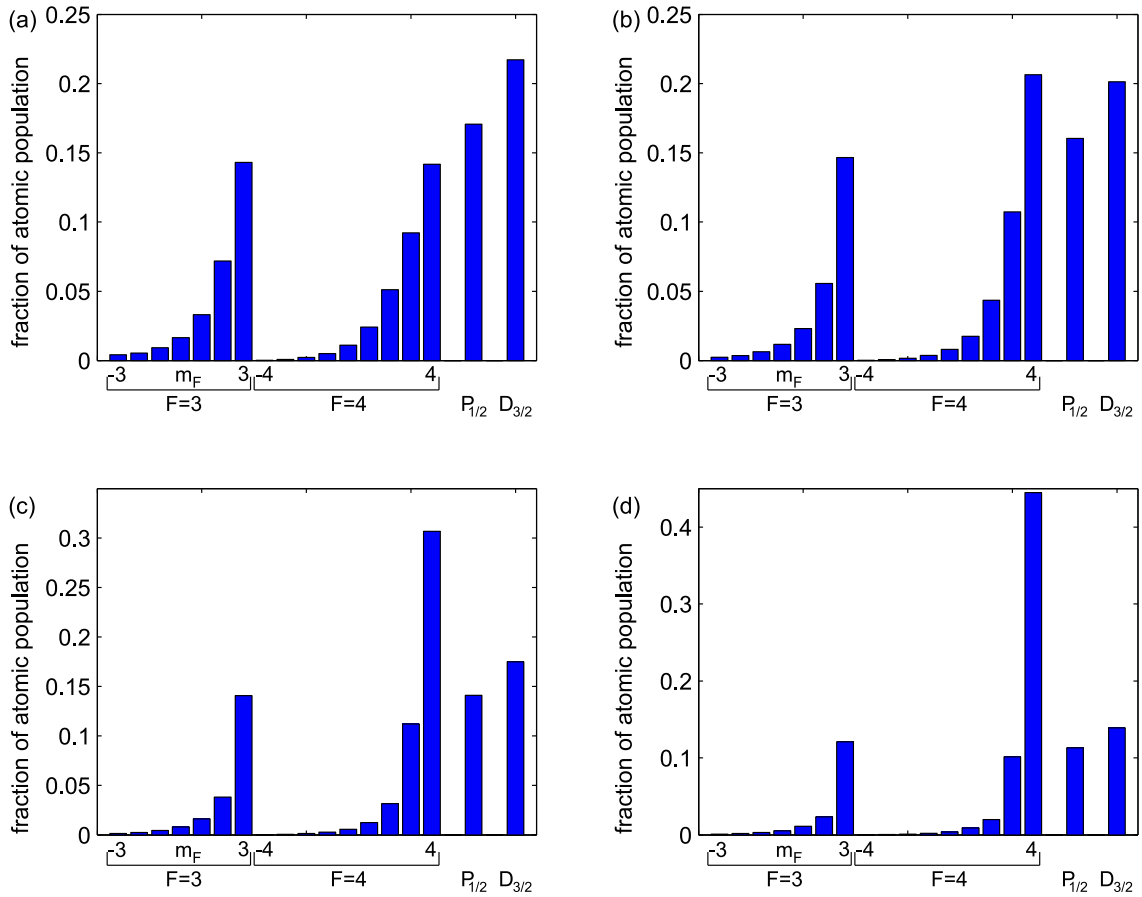


Figure 7.5: Study of steady state populations when the cooling laser (397) is polarized to provide some optical pumping. The histograms show the populations in the ground state Zeeman sublevels and the total population in $4P_{1/2}$ and $3D_{3/2}$. The 866 repumping laser was modulated at 170 MHz as discussed in section 7.3.2 and has an intensity of $350I_0^{866}$. The 397 light has a total intensity of $10I_0^{397}$ split between a σ^+ polarised beam modulated by an EOM and a π polarised beam with single frequency. The ratio of intensities of the σ^+ and π beams was 4:1, 9:1, 19:1, 39:1 for figures (a) through to (d).

Chapter 8

Conclusion

This thesis described experiments primarily concerned with the manipulation of the spin and motional state of one or a pair of ions.

In chapter 3 and appendix A we presented an experimental investigation of photoionization of Ca I via laser excitation of its $4s4p^1P_1$ state, as a means to load Ca II ions into a trap. compared with our previous method of electron bombardment, photoionization allows more controlled loading of a specific calcium isotope in a non-perturbative manner. We made measurements of the loading rate of the most abundant isotope ^{40}Ca into the trap as a function of laser powers and detunings. In combination with a measurement of the number density in the atomic beam, the loading rate allowed the cross section for ionization of the 1P_1 state of calcium I by the 389 laser to be found. We demonstrated loading and laser cooling of all the naturally occurring isotopes of calcium, including ^{43}Ca . We obtained the first laser-cooled Coulomb crystals of $^{43}\text{Ca}^+$. this isotope will be used in the next generation of experiments in our group.

The coherent manipulation of a single qubit using magnetic resonance and a.c. Stark shifts was presented in chapter 4. We used $^{40}\text{Ca}^+$ ions, the Zeeman sublevels of the ground state forming the qubit. The magnetic resonance allowed us to measure the magnetic field experienced by an ion to sub-mG precision. Before this work our most accurate method of determining the magnetic field magnitude at the ion was the use of dark resonances between the 397 and 866 transitions, which gave an accuracy of 0.1 G[30]. This method however does not give good results at the low magnetic field we now work with because the Zeeman components of the dark resonance, whose frequency difference gives the magnetic field, are unable to be unresolved. By making use of the two-photon transition between ground state Zeeman levels we use for cooling, we are now able to determine the field to similar accuracy at low field. Once the field has been measured this way, we can then use the magnetic resonance to determine the qubit splitting to around 1 kHz (corresponding to a field precision of 0.4 mG), which is less than the magnitude of the 50 Hz fluctuations in field strength.

Using the magnetic resonance we have demonstrated coherent manipulation of an ionic qubit, driving Rabi oscillations with Rabi frequencies of $\sim 2\pi \cdot 5$ kHz. Based on 1 ms of population oscillation data, the time constant for the exponential decay of the amplitude of flopping can be as long as 4 ms. A Ramsey-spin-echo type of experiment was used to measure phase changes induced in the ion by the light shift caused by each of the Raman beams. This allowed us to implement single-qubit phase rotations with a π time of order a few μs , and to gain precise knowledge of the coupling of the laser to the ion. The same experimental set-up was also used to set the polarisation of each of the Raman

beams accurately to linear, so that they induced no differential light shift, and thus phase, between the two spin states of the ion.

Although the Rabi frequency obtainable with the magnetic resonance is low compared with that possible using the lasers to drive Raman transitions, it provides a useful diagnostic. It enables accurate measurement of the Larmor frequency, the driving is independent of the motional state of the ion, and for multiple ions, the same strength on each of the ions is guaranteed.

Once an ion has been cooled into the Lamb-Dicke regime it is possible to use the Raman lasers to drive spin changing transitions with much higher Rabi frequencies. We used Raman transitions both on the carrier and the sidebands as a standard tool throughout our studies of sideband cooling. A typical example gave a carrier Rabi frequency of $2\pi \cdot 270$ kHz. The observed time dependence was consistent with the expected behaviour for a thermal state of the ion.

The cooling of single ions was discussed in chapter 5. A simple theoretical model of continuous Raman sideband cooling was presented. This treated the cooling process as an excitation by the probe laser of a narrow resonance in the atom created by the presence of the pump laser. The excitation profile is calculated from the optical Bloch equations for a three-level Λ system. It includes the null (dark resonance) caused when the probe/pump beams are in Raman resonance, and the narrow bright resonance. This analysis permits the cooling rate and steady state temperature to be understood. It guided the choice of experimental parameters and our interpretation of the results.

All of the one-ion cooling experiments were performed in a trap of axial frequency of around $2\pi \cdot 816$ kHz. Temperature measurements were performed by comparing the excitation on the first red and first blue sidebands driven by the Raman beams after a given motional state had been achieved.

We studied experimentally continuous cooling using both red and blue detuned beams. The steady state fluorescence spectrum emitted by the ion as a function of the probe laser frequency was examined in detail for the case of red detuning. By measuring the light shift produced by the pump beam we were able to identify features seen in the spectrum with specific motional transitions. Taking such a spectrum allows the probe detuning which corresponds to the 1st red sideband to be easily deduced. Using the Raman beams to measure the mean vibrational quantum number showed that the coldest ion was obtained for a probe detuning corresponding to the first red sideband, confirming our interpretation of the fluorescence spectrum. Using this cooling method a mean vibrational excitation of $\bar{n}_z=0.4$ has been achieved, which while low is higher than we would expect. Lower values of \bar{n}_z were obtained – around 0.15 – using blue detuned beams, albeit with a lower cooling rate. The blue detuned method, while producing lower temperatures, is however less convenient to implement experimentally.

To provide additional cooling we performed pulsed Raman sideband cooling after red-detuned continuous cooling. A sequence of 5 pulses on the first red sideband caused the observed motional excitation to fall from $\bar{n}_z=0.5$ to $\bar{n}_z=0.17$ (corresponding to $20 \mu\text{K}$).

By introducing a delay between cooling and temperature measurement a first measurement of the heating rate in our trap was taken. A value $d\bar{n}_z/dt = 0.02(3)/\text{ms}$ was obtained. This is a low value. Heating of an ion is caused by fluctuating electric fields at the ion position. The comparatively large size of our trap compared with those used at NIST would lead one to expect a low heating rate, assuming the voltage sources connected to the electrodes are stable. Our observed rate is consistent with the d^{-4} scaling of electric field noise in ion traps reported in world-wide studies to date.

Cooling of a pair of ions was described in chapter 6. We first presented theoretical analysis of a pair of ions being driven on the first red or blue sidebands of one of the two axial motional modes. For a single ion the comparison of sidebands method is an elegant and robust way of determining ion temperature. A similar method exists for a pair of ions, however it requires that the populations in the four different spin states be determined. We instead just measured the probability that both ions were shelved, which is easily distinguished from the case of one or both ions being shelved by looking for fluorescence. Determining temperatures then requires care to be taken with the analysis, and the sideband excitation pulses should be timed to produce maximum change in internal state.

In a trap with $\omega_z = 2\pi \cdot 306$ kHz we demonstrated cooling of both motional modes into the Lamb-Dicke regime, with the excitation of the COM mode being measured as $\bar{n}_c=0.9$ and of the stretch mode $\bar{n}_s=0.5$. Such temperatures are sufficient to allow a ‘wobble’ gate to be performed without significant infidelity due to ion temperature.

Finally, in chapter 7 we presented theoretical work concerning the $^{43}\text{Ca}^+$ ion. The use of the $|F = 3, m_F = 3\rangle$ and $|F = 4, m_F = 4\rangle$ sublevels of the ground state will allow a high readout efficiency due to the hyperfine splitting. A system of rate equations was described which allows the populations in different sublevels of the ion to be calculated for a given set of laser parameters. This was applied to create a fit to data taken with a $^{43}\text{Ca}^+$ ion during our photoionization experiments. We also investigated the efficiency of excitation to the $4P_{1/2}$ level (and thus the fluorescence rate) for different 866 parameters and modulations. We explored the possibility of maintaining strong fluorescence at the same time as optical pumping into high m_F sublevels.

The wobble gate

The next experimental goal in the Oxford ion trap group is the entanglement of a pair of ions using the ‘wobble’ gate as described in the introductory chapter. This involves the use of the Raman beams set to have a frequency difference close to the stretch mode frequency. The basic building blocks required for this gate are now in place and while the data presented in the two ion cooling chapter was being taken some first (unsuccessful) attempts at performing the gate were performed.

A successful implementation of the entangling operation will require further experiments to be performed, to optimise and further characterise the system.

One set of experiments, some of which have been done whilst this thesis has been written, is to use wobble type pulses to drive a single ion coherent state around phase space, similarly to the “Schrödinger’s cat” experiments performed at NIST[70]. These experiments allow the use of the Raman beams to displace coherent states to be demonstrated, and should allow their further characterisation.

The wobble gate requires that two ions should be separated by an integral number of standing-wave wavelengths, so that the stretch mode is only driven when the two ions are in different internal states. Owing to uncertainty in the angles between the Raman beams and the trap axis, the standing wave period is not known with sufficient accuracy to allow us to meet this condition without a further diagnostic experiment. The ion separation is easily controlled through the setting of the axial trap frequency. It is possible to determine experimentally when the ions are separated by an integer number of wavelengths by preparing the $|\downarrow\downarrow\rangle$ state, applying a displacement pulse resonant with the stretch mode frequency, and observing whether the motional state is heated. If it is not then both ions

are experiencing the same force and their separation is correct for the gate.

Future experimental improvements

Further into the future several aspects of the experiment will need to be improved to allow more complicated experiments to be undertaken.

A tighter trap would allow faster gate operations and lower the values of \bar{n}_z obtained by cooling. Combined with the lower Lamb-Dicke parameter this would place us deeper in the Lamb-Dicke regime. As stated in chapter 6, although not presented here two ion experiments with a COM frequency of $2\pi \cdot 500$ kHz have been performed. To allow higher axial frequencies the radial confinement needs to be increased. This has been attempted by using a helical resonator instead of the Colpitts oscillator[32] however this has proved unreliable up until now.

Currently, each different Raman laser detuning (or same detuning but different phase) added to the experiment requires the use of an additional synthesizer to be incorporated into the network described in section 2.3. As pulse sequences become more elaborate this will become unwieldy and a more sophisticated r.f. system will be needed.

The most time consuming part of the experimental sequence is often the photon counting for read out, particularly if we need to be able to distinguish between one and two shelved ions in two ion experiments. Increased photon scattering rate would reduce this time, and a better imaging system that is able to collect more photons would be a great improvement.

The use of $^{43}\text{Ca}^+$ would provide benefits in terms of read out, and qubit stability. Construction of laser systems specific to this isotope are already underway[45].

Finally, a more complicated trap structure with segmented electrodes and multiple trapping regions is a promising route towards implementing general quantum networks on larger numbers of ions.

Appendix A

Photoionization publication

Following is a copy of a paper published in Physical Review A describing photoionization, as discussed in chapter 3.

Appendix B

Rate equations code

This appendix contains the Matlab code used to implement the $^{43}\text{Ca}^+$ rate equations described in chapter 7. The two most important functions are `gentrans` and `genstim`. `gentrans` only needs to be called once, at the start of the Matlab session. It generates 15 lists covering the possible combinations of laser (397, 866 etc) and polarisation ($\sigma^+/\sigma^-/\pi$). Each list contains all the transitions which can be driven by that combination giving the values of i, j and $\Gamma_{j\rightarrow i}$ (which are defined in section 7.2). It also generates the part of the matrix \mathbf{M} that results from spontaneous processes from these $\Gamma_{j\rightarrow i}$. `genstim` generates the other part of the matrix \mathbf{M} , that which results from stimulated processes. Its parameters include the transition lists already generated and details of the laser parameters. Other functions generate needed values such as the frequency of different hyperfine structure components, which are needed by `genstim` to calculate detunings.

The program `hfsscan.m` is an example program, which generates the fit in section 7.3.1.

```
%----- hfsscan.m -----
% scan 397 laser over hyperfine transitions
setuprates %generate transition lists, Mdecay etc

B=1.5;      %magnetic field /G

I393=0.26; %laser intensities /I_0
I397=0.26;
I854=2110;
I866=96;

d397=-2069; %laser detunings /MHz
d854=135;
d866=-177;
d393=d393_45-20;

%fixed lasers - laser {397,393,866,850,854}, pol (1=sp,0=pi,-1=sm), I/I_0, f\MHz
flasers=[
    854,1,I854/2,d854;
    854,-1,I854/2,d854;
    393,1,I393,d393;
    866,1,I866/2,d866;
    866,-1,I866/2,d866;
];
```

```

flasers(:,4)=flasers(:,4)*2*pi*1e6;      %convert MHz -> angular s-1
Mstimf=genstim(trans,dE,width,flasers); %stimulated rates of fixed lasers

numpoints=200;
det=linspace(-3300,-600,numpoints);
clear pops1 p0 p1

for a=1:numpoints;

    d397=det(a);

    slasers=[          %scanned lasers, same format as flasers
        397,1,I397/2,d397;
        397,-1,I397/2,d397;
    ];

    slasers(:,4)=slasers(:,4)*2*pi*1e6;

    Mstims=genstim(trans,dE,width,slasers);      %stimulated rates of scanning lasers
    M=Mdecay+Mstimf+Mstims;

    c =ones(1,144);
    M(144,:)=c;
    r =zeros(144,1);
    r(144)=1;
    y1 = M\r;          %steady state population - 144 element vector

    pops1(:,a)=y1;
end

ps1=sum(pops1(1:16,:),1);      %vector of population in S1/2 for each detuning
pd3=sum(pops1(17:48,:),1);    %vector of population in D3/2 for each detuning
pd5=sum(pops1(49:96,:),1);    %etc...
pp1=sum(pops1(97:112,:),1);
pp3=sum(pops1(113:144,:),1);

R=132e6*pp1+136e6*pp3;      %scattering rate from P level populations and A coeffs
counts=0.333*0.13e-2*R+730; %0.333s per point, offset of 730 counts

%----- setuprates.m -----
if exist('trans')~=1
    global term L J F mF
    global trans Mdecay
    disp('Generating transition strengths');
    [term,term1,L,J,F,mF]=genLEVELS;
    [trans,Mdecay]=gentranlists(term,term1,L,J,F,mF);
    width=-diag(Mdecay); %sum each row to get total decay rate from each
    dEhfs=genhfsenergy(term,L,J,F);
end

loaddetuningdefs          %list of detunings for various hyperfine components

if exist('B')~=1
    disp('No B field value set, setting to zero');

```

```

    B=0;
end

dEzmn=genzmnenergy(term,L,J,F,mF,B);
dE=dEhfs+dEzmn;          %level offsets from no hfs/Zeean

%----- genLEVELS.m -----
function [term,term1,L,J,F,mF]=genLEVELS
% generates lists detailing the properties of each sublevel
% [term,term1,L,J,F,mF]=genLEVELS
% term,L,J,F,mF 144*1 vector giving the relevent parameter.
% term=1 is S_{1/2}, up in energy to term=5, P_{3/2}
% term1 is a 5*2 matrix, giving the start and end level of each term

term=zeros(144,1);
L=zeros(144,1);
J=zeros(144,1);
F=zeros(144,1);
mF=zeros(144,1);

%term #1 - 4S_{1/2}
term(1:16)=1;
term1(1,:)=[1,16];
L(1:16)=0;
J(1:16)=1/2;
F(1:7)=3;
F(8:16)=4;
mF(1:7)=-3:3;
mF(8:16)=-4:4;

%term #2 - 3D_{3/2}
term(17:48)=2;
term1(2,:)=[17,48];
L(17:48)=2;
J(17:48)=3/2;
F(17:21)=2;
F(22:28)=3;
F(29:37)=4;
F(38:48)=5;
mF(17:21)=-2:2;
mF(22:28)=-3:3;
mF(29:37)=-4:4;
mF(38:48)=-5:5;

%term #3 - 3D_{5/2}
term(49:96)=3;
term1(3,:)=[49,96];
L(49:96)=2;
J(49:96)=5/2;
F(49:51)=1;
F(52:56)=2;
F(57:63)=3;
F(64:72)=4;
F(73:83)=5;

```

```

F(84:96)=6;
mF(49:51)=-1:1;
mF(52:56)=-2:2;
mF(57:63)=-3:3;
mF(64:72)=-4:4;
mF(73:83)=-5:5;
mF(84:96)=-6:6;

%term #4 - 4P_1/2
term(97:112)=4;
term1(4,:)=[97,112];
L(97:112)=1;
J(97:112)=1/2;
F(97:103)=3;
F(104:112)=4;
mF(97:103)=-3:3;
mF(104:112)=-4:4;

%term #5 - 4P_3/2
term(113:144)=5;
term1(5,:)=[113,144];
L(113:144)=1;
J(113:144)=3/2;
F(113:117)=2;
F(118:124)=3;
F(125:133)=4;
F(134:144)=5;
mF(113:117)=-2:2;
mF(118:124)=-3:3;
mF(125:133)=-4:4;
mF(134:144)=-5:5;

return

%----- gextranlists.m -----
function [trans,Mgamma]=gextranlists(term,term1,L,J,F,mF)
% generates lists of possible transitions for each laser and a decay matrix
% [trans,Mgamma]=gextranlists(term,term1,L,J,F,mF)
% trans={'lasnam',upperterm,lowerterm,pol,tranlist;...}; tranlist=[ulev,llev,decay;...]
% treats the D levels as stable (ie no decays/transitions from D to S)

trans={ '397s+',4,1,1,[];           %cell matrix detailing transitions
        '397pi',4,1,0,[];           %trans{*,1}=name
        '397s-',4,1,-1,[];         %trans{*,2}=upper term
        '866s+',4,2,1,[];         %trans{*,3}=lower term
        '866pi',4,2,0,[];         %trans{*,4}=polarization
        '866s-',4,2,-1,[];        %trans{*,5}=list of transitions
        '393s+',5,1,1,[];
        '393pi',5,1,0,[];
        '393s-',5,1,-1,[];
        '850s+',5,2,1,[];
        '850pi',5,2,0,[];
        '850s-',5,2,-1,[];
        '854s+',5,3,1,[];

```

```

'854pi',5,3,0,[];
'854s-',5,3,-1,[] };

a=size(trans,1); %how many transitions are there?
Mgamma=zeros(144,144);

A=zeros(5,5); %A coefficients
A(2,1)=0.83;
A(3,1)=0.86;
A(4,1)=132e6;
A(5,1)=136e6;
A(4,2)=8.4e6;
A(5,2)=0.91e6;
A(5,3)=7.7e6;

for f1=1:6 %6j symbols
    for f2=1:6
        for j1=1:2:5
            for j2=1:2:5
                sjs(f1,f2,j1,j2)=sixj(f1,f2,1,j1/2,j2/2,3.5);
            end
        end
    end
end

for l=1:a %for all transitions
    tran=[];
    uppert=trans{1,2};
    lowert=trans{1,3};
    pol=trans{1,4};
    for m=term1(uppert,1):term1(uppert,2) %loop over the levels in the upper term
        for n=term1(lowert,1):term1(lowert,2) %loop over the levels in the lower term
            if abs(F(m)-F(n))<2 & (mF(m)-mF(n))==pol %if dF=+-1,0 and dmF=pol then:
                CG2=(2*F(m)+1)*threej(F(n),1,F(m),mF(n),pol,-mF(m))^2; %Square of CG coeff
                S=(2*J(m)+1)*(2*F(n)+1)*sjs(F(m),F(n),J(n)*2,J(m)*2)^2; %Component strength S
                gamma=CG2*S*A(term(m),term(n)); %decay rate from upper to lower
                tran=[tran;[m,n,gamma]]; %add to list of transitions
                Mgamma(n,m)=gamma; %and put into the decay matrix
            end
        end
    end
    trans{1,5}=tran;
end

Mgamma=-diag(sum(Mgamma))+Mgamma; %generate diagonal elements

return

%----- genhfsenergy.m -----
function dEhfs=genhfsenergy(term,L,J,F)
%generate the hfs splittings for calcium in angular units s^{-1}

A=[-806.4;-47.3;-3.8;-145.4;-31.0]; %in MHz
B=[0;-4;-4;0;-7];

```

```

I=7/2;

C=F.*(F+1)-I*(I+1)-J.*(J+1);
D=(3/2)*C.*(C+1) - 2*I*(I+1).*J.*(J+1);
E=(2*I-1)*I*(2.*J-1).*J;
E(find(E==0))=1;           %strip out all zeros, as will cause NaNs in dEhfs.
                           %doesn't matter what we replace with as B=0 for these cases

dEhfs=(A(term).*C/2 + (1/4)*B(term).*D./E)*2*pi*1e6;   %convert to angular /s

return

%----- genzmnenergy.m -----
function dEzman=genzmnenergy(term,L,J,F,mF,B)
% B in Gauss, returns angular frequency s^{-1}

I=7/2;
S=1/2;
mu_B=9.274e-24/1.0546e-34; %in angular units

gJ=( 3.*J.*(J+1)+S*(S+1)-L.*(L+1) ) ./ (2*J.*(J+1)); %taking g_s=2.
gF=gJ.*( F.*(F+1)+J.*(J+1)-I*(I+1) )./( 2*F.*(F+1) );

dEzman=mu_B*B*1e-4*gF.*mF;

return
%----- genstim.m -----
function [Mstim]=genstim(trans,energy,width,lasers)
% generates stimulated transition matrix

numl=size(lasers,1); %how many lasers?
Mstim=zeros(144,144);

for a=1:numl %loop over lasers
    pol=lasers(a,2);
    int=lasers(a,3);
    ldetune=lasers(a,4);

    switch lasers(a,1)
    case 397
        tranlist=trans{2-pol,5}; %get the transitions list for this laser
    case 866
        tranlist=trans{5-pol,5}; %get the transitions list for this laser
    case 393
        tranlist=trans{8-pol,5}; %get the transitions list for this laser
    case 850
        tranlist=trans{11-pol,5}; %get the transitions list for this laser
    case 854
        tranlist=trans{14-pol,5}; %get the transitions list for this laser
    otherwise
        disp('Laser set incorrectly! Las num ',num2str(a),' labelled: ',num2str(lasers(a,1)))
        tranlist=[144,1,0];
    end
end

```

```
numtran=size(tranlist,1);
for b=1:numtran           %loop over each transition
    ulev=tranlist(b,1);
    lolev=tranlist(b,2);
    gamma=tranlist(b,3);
    detune=ldetune - (energy(ulev)-energy(lolev));

    g=(1/(2*pi))*width(ulev)/( detune^2 + width(ulev)^2/4 );
    rabi2=int*width(ulev)*gamma;
    rate=(pi/2)*rabi2*g;

    Mstim(ulev,lolev)=Mstim(ulev,lolev)+rate;           %in case a laser is listed twice
end
end

Mstim=Mstim+Mstim';           %rate(lo->up)==rate(up->lo)
Mstim=-diag(sum(Mstim))+Mstim;           %generate diagonal elements

return
```

Bibliography

- [1] H. S. Margolis, G. P. Barwood, G. Huang, H. A. Klein, S. N. Lea, K. Szymaniec, and P. Gill. Hertz-level measurement of the optical clock frequency in a single $^{88}\text{Sr}^+$ ion. *Science*, 306:1355–1358, 2004.
- [2] C. A. Sackett, D. Kielpinski, B. E. King, C. Langer, V. Meyer, C. J. Myatt, M. Rowe, Q. A. Turchette, W. M. Itano, D. J. Wineland, and C. Monroe. Experimental entanglement of four particles. *Nature*, 404:256–259, 2000.
- [3] M. Riebe, H. Häffner, C. F. Roos, W. Hansel, J. Benhelm, G. P. T. Lancaster, T. W. Korber, C. Becher, F. Schmidt-Kaler, D. F. V. James, and R. Blatt. Deterministic quantum teleportation with atoms. *Nature*, 429:734–737, 2004.
- [4] M. D. Barrett, J. Chiaverini, T. Schaetz, J. Britton, W. M. Itano, J. D. Jost, E. Knill, C. Langer, D. Leibfried, R. Ozeri, and D. J. Wineland. Deterministic quantum teleportation of atomic qubits. *Nature*, 429:737–739, 2004.
- [5] A. Steane. Multiple particle interference and quantum error correction. *Proc. R. Soc. Lond. A*, 452(2551–2577), 1996.
- [6] J. Chiaverini, D. Leibfried, T. Schaetz, M. D. Barrett, R. B. Blakestad, J. Britton, W. M. Itano, J. D. Jost, E. Knill, C. Langer, R. Ozeri, and D. J. Wineland. Realization of quantum error correction. *Nature*, 432(7017):602–605, 2004.
- [7] D. Deutsch. Quantum computational networks. *Proc. R. Soc. Lond. A*, 425:73–90, 1989.
- [8] A. Barenco. Quantum physics and computers. *Contemp. Phys.*, 37:357–389, 1996.
- [9] D. P. DiVincenzo. The physical implementation of quantum computation. *Fortschr. Phys.*, 48(9–11):771–783, 2000.
- [10] D. Kielpinski, C. Monroe, and D. J. Wineland. Architecture for a large-scale ion trap quantum computer. *Nature*, 417:709–711, 2002.
- [11] J. P. Home and A. M. Steane. Electric octopole configurations for fast separation of trapped ions. [quant-ph/0411102](https://arxiv.org/abs/quant-ph/0411102).
- [12] J. I. Cirac and P. Zoller. Quantum computations with cold trapped ions. *Phys. Rev. Lett.*, 74:4091–4094, 1995.
- [13] F. Schmidt-Kaler, S. Gulde, M. Riebe, T. Deuschle, A. Kreuter, G. Lancaster, C. Becher, J. Eschner, H. Häffner, and R. Blatt. The coherence of qubits based on single Ca^+ ions. *J. Phys. B: At. Mol. Opt. Phys.*, 36(3):623–636, 2003.

- [14] J. J. Garcia-Ripoll, P. Zoller, and J. I. Cirac. Speed optimized two-qubit gates with laser coherent control techniques for ion trap quantum computing. *Phys. Rev. Lett.*, 91(15):157901, 2003.
- [15] W. Nagourney, J. Sandberg, and H. Dehmelt. Shelved optical electron amplifier: Observation of quantum jumps. *Phys. Rev. Lett.*, 56:2797–2799, 1986.
- [16] Th. Sauter, W. Neuhauser, and R. Blatt. Observation of quantum jumps. *Phys. Rev. Lett.*, 57:1696–1698, 1986.
- [17] J. C. Bergquist, R. G. Hulet, W. M. Itano, and D. J. Wineland. Observation of quantum jumps in a single atom. *Phys. Rev. Lett.*, 57:1699–1702, 1986.
- [18] D. J. Wineland, C. Monroe, W. M. Itano, D. Leibfried, B. E. King, and D. M. Meekhof. Experimental issues in coherent quantum-state manipulation of trapped atomic ions. *J. Res. Natl. Inst. Stand. Technol*, 103(3):259–328, 1998.
- [19] C. Monroe, D. Leibfried, B. E. King, D. M. Meekhof, W. M. Itano, and D. J. Wineland. Simplified quantum logic with trapped ions. *Phys. Rev. A*, 55:2489, 1997.
- [20] F. Schmidt-Kaler, H. Häffner, M. Riebe, S. Gulde, G. P. T. Lancaster, T. Deuschle, C. Becher, C. F. Roos, J. Eschner, and R. Blatt. Realization of the Cirac–Zoller controlled-NOT quantum gate. *Nature*, 422:408–411, 2003.
- [21] C. F. Roos, M. Riebe, H. Häffner, W. Hänsel, J. Benhelm, G. P. T. Lancaster, C. Becher, F. Schmidt-Kaler, and R. Blatt. Control and measurement of three-qubit entangled states. *Science*, 304:1478–1480, 2004.
- [22] A. Sørensen and K. Mølmer. Quantum computation with ions in thermal motion. *Phys. Rev. Lett.*, 82(9):1971–1974, 1999.
- [23] K. Mølmer and A. Sørensen. Multiparticle entanglement of hot trapped ions. *Phys. Rev. Lett.*, 82(9):1835–1838, 1999.
- [24] G.J. Milburn and S. Schneider a D.F.V. Jamesnd. Ion trap quantum computing with warm ions. *Fortschr. Phys.*, 48(9–11):801–810, 2000.
- [25] A. Sørensen and K. Mølmer. Entanglement and quantum computation with ions in thermal motion. *Phys. Rev. A*, 62:022311, 2000.
- [26] D Leibfried, B DeMarco, V Meyer, D Lucas, M Barrett, J Britton, W M Itano, B Jelenkovic, C Langer, T Rosenband, and D J Wineland. Experimental demonstration of a robust, high-fidelity geometric two ion-qubit phase gate. *Nature*, 422:412–415, 2003.
- [27] D. Leibfried, M. D. Barrett, T. Schaetz, J. Britton, J. Chiaverini, W. M. Itano, J. D. Jost, C. Langer, and D. J. Wineland. Toward Heisenberg-limited spectroscopy with multiparticle entangled states. *Science*, 304:1476–1478, 2004.
- [28] P. Carruthers and M. M. Nieto. Coherent states and the forced quantum oscillator. *Am. J. Phys.*, 7:537–544, 1965.

- [29] D. M. Lucas. Development of a linear ion trap for quantum computing. In *Proc. First. Int. Conf. on Experimental Implementations of Quantum Computers*, pages 91–98, Princeton, 2001. Rinton Press.
- [30] M. McDonnell. *Two-Photon Readout Methods for an Ion Trap Quantum Information Processor*. PhD thesis, University of Oxford, 2003.
- [31] M. J. McDonnell, J.-P. Stacey, S. C. Webster, J. P. Home, A. Ramos, D. M. Lucas, D. N. Stacey, and A. M. Steane. High-efficiency detection of a single quantum of angular momentum by suppression of optical pumping. *Phys. Rev. Lett.*, 93(15):153601, 2004.
- [32] J. P. Stacey. *Stabilization and Control in a Linear Ion Trap*. PhD thesis, University of Oxford, 2003.
- [33] N. Kjærgaard, L. Hornekær, A. M. Thommesen, Z. Videsen, and M. Drewsen. Isotope selective loading of an ion trap using resonance-enhanced two-photon ionization. *Appl. Phys. B: Lasers Opt.*, 71:207–210, 2000.
- [34] S. Gulde, D. Rotter, P. Barton, F. Schmidt-Kaler, R. Blatt, and W. Hogervorst. Simple and efficient photo-ionization loading of ions for precision ion-trapping experiments. *Appl. Phys. B*, 73:861, 2001.
- [35] K. Koo, J. Sudbery, D. M. Segal, and R. C. Thompson. Doppler cooling of Ca^+ ions in a Penning trap. *Phys. Rev. Lett.*, 69:043402, 2004.
- [36] H. G. Dehmelt. Radio-frequency spectroscopy of stored ions I. storage. *Adv. At. Mol. Phys.*, 3:53, 1967.
- [37] P. K. Ghosh. *Ion Traps*. Oxford University Press, 1995.
- [38] D. A. Stevens. *The Quantum Manipulation of Ions*. PhD thesis, University of Oxford, 1999.
- [39] C. Donald. *Development of an Ion Trap Quantum Information Processor*. PhD thesis, University of Oxford, 2000.
- [40] D. Leibfried, R. Blatt, C. Monroe, and D. Wineland. Quantum dynamics of single trapped ions. *Reviews of Modern Physics*, 75(1):281, 2003.
- [41] S. C. Webster. *Ion Trapping with a Paul trap*. First Year Report, University of Oxford, 2002.
- [42] A. Yariv. *Optical Electronics*. Oxford University Press, 1991.
- [43] R. W. P. Drever, J. L. Hall, F. V. Kowalski, J. Hough, G. M. Ford, A. J. Munley, and H. Ward. Laser phase and frequency stabilization using an optical resonator. *Appl. Phys. B*, 31:97–105, 1983.
- [44] E. D. Black. An introduction to Pound-Drever-Hall laser frequency stabilization. *Am. J. Phys.*, 69:79–87, 2001.
- [45] B. Keitch. *Transfer Report*. First Year Report, University of Oxford, 2004.

- [46] R. D. Cowan. *The theory of atomic structure and spectra*. California Press, 1981.
- [47] H. W. van der Hart and C. McKenna. Private communication.
- [48] M. J. McDonnell, D. N. Stacey, and A. M. Steane. Laser linewidth effects in quantum state discrimination by EIT. *Phys. Rev. A*, 70:053802, 2004.
- [49] D. J. Wineland and W. M. Itano. Laser cooling of atoms. *Phys. Rev. A*, 20(4):1521 – 1540, 1979.
- [50] G. Morigi, J. Eschner, and C. Keitel. Ground state laser cooling using electromagnetically induced transparency. *Phys. Rev. Lett.*, 85:4458–4461, 2000.
- [51] D. Stevens, J. Brochard, and A. M. Steane. Simple experimental methods for trapped-ion quantum processors. *Phys. Rev. A*, 58(4):2750 – 2759, 1998.
- [52] C. Monroe, D. M. Meekhof, B. E. King, S. R. Jefferts, W. M. Itano, D. J. Wineland, and P. Gould. Resolved-sideband Raman cooling of a bound atom to the 3d zero-point energy. *Phys. Rev. Lett.*, 75(22):4011, 1995.
- [53] I. Marzoli, J. I. Cirac, R. Blatt, and P. Zoller. Laser cooling of trapped three-level ions: Designing two-level systems for sideband cooling. *Phys. Rev. A*, 49(4), 1994.
- [54] Ch. Roos, Th. Zeiger, H. Rohde, H. C. Nägerl, J. Eschner, D. Leibfried, F. Schmidt-Kaler, and R. Blatt. Quantum state engineering on an optical transition and decoherence in a paul trap. *Phys. Rev. Lett.*, 83(23):4713, 1999.
- [55] C. Roos, D. Leibfried, A. Mundt, F. Schmidt-Kaler, J. Eschner, and R. Blatt. Experimental demonstration of ground state laser cooling with electromagnetically induced transparency. *Phys. Rev. Lett.*, 85:5547–5550, 2000.
- [56] M. Lindberg and J. Javanainen. Temperature of a laser-cooled trapped three-level ion. *J. Opt. Soc. Am. B*, 3:1008–1017, 1986.
- [57] Q. A. Turchette, D. Kielpinski, B. E. King, D. Leibfried, D. M. Meekhof, C. J. Myatt, M. A. Rowe, C. A. Sackett, C. S. Wood, W. M. Itano, C. Monroe, and D. J. Wineland. Heating of trapped ions from the quantum ground state. *Phys. Rev. A*, 61(6):063418, 2000.
- [58] J. Home. *Temperature measurement of two ions*. Group Report, 2004.
- [59] B. E. King, C. S. Wood, C. J. Myatt, Q. A. Turchette, D. Leibfried, W. M. Itano, C. Monroe, and D. J. Wineland. Cooling the collective motion of trapped ions to initialize a quantum register. *Phys. Rev. Lett.*, 81(7):1525–1528, 1998.
- [60] D. Kielpinski, V. Meyer, M. A. Rowe, C. A. Sackett, W. M. Itano, C. Monroe, and D. J. Wineland. A decoherence-free quantum memory using trapped ions. *Science*, 291:1013–1015, 2001.
- [61] C. F. Roos, G. P. T. Lancaster, M. Riebe, H. Haffner, W. Hansel, S. Gulde, C. Becher, J. Eschner, F. Schmidt-Kaler, and R. Blatt. Bell states of atoms with ultralong lifetimes and their tomographic state analysis. *Phys. Rev. Lett.*, 92(22):220402, 2004.

- [62] D. J. Berkeland and M. G. Boshier. Destabilization of dark states and optical spectroscopy in Zeeman-degenerate atomic systems. *Phys. Rev. A*, 65(3):033413, 2002.
- [63] G. K. Woodgate. *Elementary Atomic Structure*. Oxford University Press, 2nd edition, 1980.
- [64] F. Arbes, M. Benzing, Th. Gudjons, F. Kurth, and G. Werth. Precise determination of the ground state hyperfine structure splitting of ^{43}Ca II. *Z. Phys. D*, 31:27–30, 1994.
- [65] W. Nörtershäuser, K. Blaum, K. Icker, P. Müller, A. Schmitt, K. Wendt, and B. Wiche. Isotope shifts and hyperfine structure in the $3d^2D_J \rightarrow 4p^2P_J$ transitions in calcium II. *Eur. Phys. J. D*, 2(1):33–39, 1998.
- [66] A. Ramos. *Isotope shifts and hyperfine structure in calcium*. Group Report, 2002.
- [67] H. J. Metcalf and P. van der Straten. *Laser cooling and trapping*. Springer, 1999.
- [68] A. M. Steane. *A Summary of Saturation Intensities*. Group Report, 2000.
- [69] R. Loudon. *The Quantum Theory of Light*. Oxford University Press, 2000.
- [70] C. Monroe, D. M. Meekhof, B. E. King, and D. J. Wineland. A “Schrödinger cat” superposition state of an atom. *Science*, 272(5265):1131–1136, 1996.